Submitted to Astrophysical Journal at 16 January 2019, accepted at 25 November 2019
Typeset using LaTeX **twocolumn** style in AASTeX62

Explosive Nucleosynthesis in Sub-Chandrasekhar Mass White Dwarf Models for Type Ia Supernovae: Dependence on Model Parameters

Shing-Chi Leung[1,2] and Ken'ichi Nomoto[1]

[1] *Kavli Institute for the Physics and Mathematics of the Universe (WPI),The University of Tokyo Institutes for Advanced Study, The University of Tokyo, Kashiwa, Chiba 277-8583, Japan*

[2] *TAPIR, Walter Burke Institute for Theoretical Physics, Mailcode 350-17, Caltech, Pasadena, CA 91125, USA*

(Dated: January 1, 2020)

ABSTRACT

Recent observations of Type Ia supernovae (SNe Ia) have shown diversified properties of the explosion strength, light curves and chemical composition. To investigate possible origins of such diversities in SNe Ia, we have presented multi-dimensional hydrodynamical study of explosions and associated nucleosynthesis in the near Chandrasekhar mass carbon-oxygen (CO) white dwarfs (WDs) for a wide range of parameters (Leung and Nomoto 2018 ApJ). In the present paper, we extend our wide parameter survey of models to the explosions of sub-Chandrasekhar mass CO WDs. We take the double detonation model for the explosion mechanism. The model parameters of the survey include the metallicity of $Z = 0 - 5\ Z_{\odot}$, the CO WD mass of $M = 0.90 - 1.20\ M_{\odot}$, and the He envelope mass of $M_{\rm He} = 0.05 - 0.20\ M_{\odot}$. We also study how the initial He detonation configuration, such as spherical, bubble, and ring shapes, triggers the C detonation. For these parameters, we derive the minimum He envelope mass necessary to trigger the C detonation. We then examine how the explosion dynamics and associated nucleosynthesis depend on these parameters, and compare our results with the previous representative models. We compare our nucleosynthesis yields with the unusual abundance patterns of Fe-peak elements and isotopes observed in SNe Ia 2011fe, 2012cg and 2014J, as well as SN Ia remnant 3C 397 to provide constraints on their progenitors and environments. We provide the nucleosynthesis yields table of the sub-Chandrasekhar mass explosions, to discuss their roles in the galactic chemical evolution and archaeology.

Keywords: (stars:) supernovae: general – hydrodynamics – nuclear reactions, nucleosynthesis, abundances

1. INTRODUCTION

Type Ia supernovae (SNe Ia) are known to have almost homogenized light curves and spectra, thus being used as a standard candle for studying the cosmic acceleration that led to the discovery of dark energy (e.g., Bergström & Goobar 2004; Branch & Wheeler 2017).

The basic properties of SNe Ia have been well-modeled as the explosions of CO white dwarfs (WDs) which have both near-Chandrasekhar mass and sub-Chandrasekhar mass (e.g., Hillebrandt & Niemeyer 2000). However, it is still controversial which mass (near-Chandrasekhar vs. sub-Chandrasekhar) of the WD is the actual progenitor. For the presupernova evolution in close binaries, both the single degenerate (SD) scenario and the double degenerate (DD) scenario have been discussed, but the actual evolutionary path remains unclear (e.g., Nomoto et al. 1997; Maoz et al. 2011).

Further, recent observations have shown the diversified properties of light curves and spectra of SNe Ia including very peculiar ones (e.g., Li et al. 2001; Taubenberger 2017; Jha 2017; Jiang et al. 2017). The diversity can be characterized by a wide range of ^{56}Ni and also differences in the ejecta composition and abundance. To understand this diversity, a wide range of theoretical models become necessary in order to extract the effects of each model parameter to explosion properties and nucleosynthesis yields.

To understand the origin of such diversities, we are computing SNe Ia models for wide ranges of model and environmental parameters. In Nomoto & Leung (2017); Leung & Nomoto (2018) we have studied how the model parameters, including the central density, metallicity, initial flame structure, and C/O ratio affect the explosion properties of near-Chandrasekhar mass WD mod-

els. For example, we have demonstrated how some well-observed SNe Ia and SNRs can be explained by tracing the variation of isotopes in the yields with respect to the change of model parameters.

In this paper, we present our parameter survey for the sub-Chandrasekhar mass WD model. The sub-Chandrasekhar mass explosions could occur in both SD and DD scenarios as follows.

1.1. *Sub-Chandrasekhar Mass Models in the Single Degenerate Scenario*

In the SD scenario, C+O WDs accrete matter from the non-degenerate companion stars, which include slightly evolved main-sequence stars, red-giant stars, He-main-sequence stars, evolved He stars. As a result of H-burning in the H-rich accreted material or a direct accretion of He, the mass of a He layer increases above the C+O core, leading to eventual He ignition (e.g., Nomoto & Leung 2017, 2018).

If the accretion rate of He, $\dot{M}_{\rm He}$, is higher than $\sim 10^{-8} M_\odot$ yr^{-1}, He burning shell burning makes weak flashes which recur many times to increase the WD mass toward the Chandrasekhar mass (e.g., Nomoto 1982a; Woosley & Kasen 2011). For lower rates of $10^{-10} M_\odot$ yr$^{-1} \lesssim \dot{M}_{\rm He} \lesssim 10^{-8} M_\odot$ yr^{-1}, the compressional heating rate is lower and thus the temperature of the He layer is lower, which causes a delay in the He ignition until the mass of He layer becomes large enough and the density at the bottom of He layer high enough for He burning to grow into detonation. It eventually leads to double detonation (Nomoto 1982b; Woosley et al. 1986). The double detonation model has been widely studied in 1D and multi-D simulations for various model parameters (e.g., Livne 1990; Livne & Glasner 1990, 1991; Livne & Arnett 1995; Arnett 1996; Fink et al. 2007, 2010; Sim et al. 2012; Moore et al. 2013; Moll & Woosley 2013; Shen et al. 2018; Polin et al. 2019).

The important property of the sub-Chandrasekhar mass progenitors in SD scenario is that the mass of the He layer exceeds $\sim 0.05 M_\odot$ to induce a He detonation (e.g., Nomoto 1982b; Woosley et al. 1986). This is in contrast to the sub-Chandrasekhar mass models in the DD scenario as discussed below.

1.2. *Sub-Chandrasekhar Mass Models in the Double Degenerate Scenario*

In the DD scenario, the detonation near the surface of the primary WD can be triggered during the violent merging of two WDs for suitable binary parameters (e.g., Rasio & Shapiro 1995; Segretain et al. 1997; Guerrero et al. 2004; Yoon et al. 2007; Fryer et al. 2010; Dan et al. 2011; Raskin et al. 2012, 2014; Moll et al. 2014; Sato et al. 2015). However, if there exists no He, the occurrence of the surface C detonation may still depend on the numerical resolution (e.g., Sato et al. 2015; Pakmor 2017). Then Pakmor et al. (2013); Dan et al. (2015) presented a He ignited double detonation model where the He detonation near the surface is triggered because a certain mass of He rich envelope is assumed to exist on both WDs. In contrast to the double detonation in the SD scenario, the He-ignited detonation could be triggered for a smaller mass He-rich envelope because of shock compression.

In the above DD model, the collision point can reach a sufficiently high temperature for triggering a He detonation. The He detonation can produce a shock wave which propagates through the He envelope and into the CO core. The shock-heating in the C-rich matter can induce a central or off-center C detonation. The WD is then disrupted by the C detonation. This model may produce the diversity of the different brightness, depending on the masses of the CO core and the He envelope (e.g., Arnett 1996; Sim et al. 2010; Woosley & Kasen 2011; Pakmor et al. 2013; Shen et al. 2018; Polin et al. 2019).

1.3. *Motivation*

In Leung & Nomoto (2017); Nomoto & Leung (2017) we have studied how the model parameters, including the central density, metallicity, initial flame structure and C/O mass fraction ratio, affect the chemical yield of SN Ia evolved from a near-Chandrasekhar mass WD. By tracing the variations of isotopes with respect to the change of model parameters, we have demonstrated how some well-observed SNe Ia can be explained by the near-Chandrasekhar mass model.

However, the occurrence rate of SNe Ia evolved from sub-Chandrasekhar WD is suggested to be higher than the near Chandrasekhar mass WD in population synthesis (See, e.g., Yungelson 2005; Maoz et al. 2014). It becomes necessary to ask whether the double detonation model can explain SNe Ia similarly to the Chandrasekhar mass model, or can even replace the Chandrasekhar mass model in certain parameter space.

Furthermore, through multi-dimensional hydrodynamics simulations, one can draw constraints on how to trigger the C detonation by the He detonation in the aspherical configuration systematically. This will set constraints on the criteria in triggering the C detonation through the aspherical He detonation with or without geometrical convergence.

To investigate possible origins of large diversities of SNe Ia, we perform two-dimensional hydrodynamical

studies of explosions and associated nucleosynthesis in the sub-Chandrasekhar mass CO WDs for wide ranges of parameters. All simulations use the code based on the two-dimensional hydrodynamics code developed for the explosion phase of supernovae (Leung et al. 2015a).

This work is a continuation of our previous work in Leung & Nomoto (2017); Nomoto & Leung (2017), where we have studied the dependence on model parameters of SNe Ia using the Chandrasekhar mass models (Leung et al. 2015b; Nomoto & Leung 2017, 2018; Leung & Nomoto 2018). In Leung & Nomoto (2018) we covered the density, metallicity, flame structure and detonation criteria. We have also shown that some of the chemical abundances features observed in recently observed SNe Ia can be reproduced by our models.

In the present paper, we want to extend our understanding to the sub-Chandrasekhar mass models for even a wider parameter region. We intend not only to explain the observed diversities of SNe Ia but also to provide the predictions of nucleosynthesis properties for coming observations (e.g., Timmes et al. 2019).

In Section 2 we summarize the numerical methods used in this work and the input physics specific to model the sub-Chandrasekhar mass model. In Section 3 we describe our two-dimensional simulations to study the exploding WDs starting from the He detonation at the envelope. In Section 5 we describe the benchmark model which is regarded as the representation of a typical sub-Chandrasekhar mass model. In Section 6 we describe nucleosynthesis yields and their dependence on the model parameters, including the WD mass, He envelope mass and initial He detonation pattern. We also present our cross-comparison with the classical double detonation model with spherical symmetry, and its possible impacts on galactic chemical evolution. In the Appendix we provide further numerical details and tests we have done for this work. We also discuss the implications of our models, including a comparison from models in the literature.

2. METHODS

2.1. *Input Physics*

Here we briefly review the structure of our hydrodynamics code and then we describe the change done to describe the He detonation and the onset of C deflagration or C detonation. We use the same two-dimensional hydrodynamics code as reported in Leung et al. (2015a) for our simulations. The code solves the Euler equations in cylindrical coordinates where the spatial discretization is done by the fifth-order weighted essentially non-oscillatory (WENO) scheme and the time-discretization is done by the five-step third-order non-strong-stability preserving Runge-Kutta scheme. We use the helmholtz subroutine (Timmes & Arnett 1999; Timmes & Swesty 1999) as the matter equation of state (EOS). This EOS includes the arbitrarily relativistic and degenerate electron gas, ions as a classical ideal gas, Planckian photon gas and electron-positron annihilation pairs. In the hydrodynamics section, we describe the chemical composition by a 7-isotope network, which includes ^{4}He, ^{12}C, ^{16}O, ^{20}Ne, ^{24}Mg, ^{28}Si and ^{56}Ni.

The one-equation model (Niemeyer et al. 1995) is used to model the velocity fluctuations in the sub-grid scale due to turbulence. To describe the geometry of the two detonation fronts, we use the individual level-set functions (Osher & Sethian 1988) as used in Reinecke et al. (1999). The geometry of the fronts are constructed by locating zero-value points in the level-set function, and then the fractional volume in each mesh being burnt by flame or detonation is extracted. The energy from nuclear burning is injected instantaneously to Eulerian grids which have an increase in the area (volume) fractions α in the 2- (3-) dimensional models enclosed by the contours and their boundaries. To prevent double-counting the energy released by burnt matter, α is set to be a monotonic increasing throughout the simulations. In each step, the code calculates the area fraction based on how the zero-contour intersects with the grid mesh. A fraction of α^* is obtained where $\alpha = 1$ for a completely burnt cell and 0 for pure fuel. The value of α^* is compared with that in the previous step $\alpha_{\rm old}$ and the larger one is taken, i.e. $\alpha = \max(\alpha^*, \alpha_{\rm old})$. For He detonation, we assume the detonation is in form of Chapman-Jouget detonation, where the detonation propagates in sound speed given by $\sqrt{\gamma_2(\partial p/\partial\rho)_s}$, where γ_2 is the adiabatic index, p and ρ are the pressure and density. For CO detonation, we used the same prescription as Sharpe (1999) by the numerical speed of pathological detonation.

All simulations are done by a resolution size of 400^2 using the cylindrical coordinate. We choose reflecting and outgoing boundaries for the inner and outer boundaries for both r and z axis. The resolution is fixed at either 15 or 23 km. The lower one is for higher mass white dwarf (mass $> 1M_\odot$) while the higher one is for lower mass white dwarfs. The grid size is chosen such that the simulation box is about 2 - 3 times of the initial WD radius. We do that because we want most exothermic reactions, which rely on the level-set method, can finish before the star reaches the outer boundary of the simulation box. We follow Roepke & Hillebrandt (2005) by implementing the moving-boundary technique so that, when the stellar outer radius reaches the simulation box boundary, the grid expands with a similar speed so that most matter can be contained in the simulation box. In

our calculation, we choose the averaged radial velocity of the low density matter (defined by 1 - 10 times of the atmospheric density) to be the expansion velocity. Following with the expansion, we also adjust the atmosphere density such that the total mass of matter in the "atmosphere" (also the minimum density allowed in the simulation) remains $\sim 10^{-4}$ of the star. We model only one quadrant of the WD by the use of reflecting boundary.

In our computation, it takes typically 2 - 3 days for a hydrodynamics simulation for a quadrant from the onset of He-detonation until homologous expansion develops by a single CPU run. The assumed symmetry allows only two He-detonation bubbles to be ignited simultaneously. A more general detonation form as a single He-detonation bubble requires hydrodynamics simulations of a hemisphere. The computational time can be lengthened by a factor of ~ 4 times with also a factor of 2 larger in memory. Thus only a small number of models are computed. In Appendix B we present some exploratory models using the relaxed symmetry and compare with our "quadrant" models. We also check the dependence of the general detonation model on the chosen resolution and report in Appendix C.

2.2. *Nuclear Reaction Scheme*

For the nuclear reactions of He-rich matter, the region swept by the level-set contour is regarded as burning from ^{4}He to ^{56}Ni. For CO-rich matter, similar to previous works (Leung & Nomoto 2018), we use the three-step burning scheme so as to include more flexible nuclear reactions, especially when there are contributions from shock wave collisions. In this work, we assume this process is instantaneous regardless of the local density. We follow the use of burning timescale as an approximation to burning where density is low (i.e. $\rho < 5 \times 10^7$ g cm^{-3}). That includes the nuclear quasi-statistical equilibrium (NQSE) timescale and the NSE timescale, given by, respectively (see Calder et al. (2007); Townsley et al. (2007)),

$$\tau_{\rm NQSE} = \exp(182/T_{f,9} - 46.1) \text{ s}, \quad (1)$$

$$\tau_{\rm NSE} = \exp(196/T_{f,9} - 41.6) \text{ s}, \quad (2)$$

where $T_{f,9} = T_f/10^9$ K is the final temperature of the ash. For a timestep shorter than these two timescales, we assume that a fraction of matter given by linear interpolation with τ is burnt. For a timestep longer than those, complete conversion of fuel to ash is assumed. Similar treatment is done for He detonation. We describe more details in Appendix A.

To determine whether a detonation wave can start, we follow the scheme in Fink et al. (2007). For an Eulerian grid of CO matter, when the temperature exceeds the threshold temperature as a function of density (see Table 1 and 2 in Fink et al. (2007)), a bubble or ring of hot ashes (i.e., NSE matter from CO and ^{56}Ni from He) is put artificially around that grid of 1.5 times the grid size. In practice, we set the level-set scalar field S in the way that $S(r,z) = -\sqrt{(r-r_0)^2+(z-z_0)^2} + 1.5\Delta x$. Here r_0 and z_0 are the center coordinates of the bubble and Δx is the resolution size. However, when multiple detonation seeds are triggered, those within 10 Δx from existing ones are discarded. At a density between 2×10^7 and 10^9 g cm^{-3}, detonation propagates in the form of pathological detonation, where behind shock front matter with a speed below the frozen sound speed appears (Sharpe 1999). The propagation velocity is obtained by solving the detonation structure explicitly. To prevent double-counting in the burnt material due to numerical diffusion, once a grid reached NSE, it is forbidden to carry out ^{16}O and ^{24}Mg burning in the second burning step. In the NSE state, the final composition is changed by solving iteratively by requiring that the change in the internal energy equals to the change in the binding energy up to the required precision. Matter in the NSE state is also allowed to carry out electron capture with a rate obtained by interpolating the pre-computed rate table using the prescription described in Seitenzahl et al. (2010).

To apply NSE calculation in the modeling, after each hydrodynamics step, we obtain a current density ρ, current electron fraction $Y_{{\rm e},i}$, trial temperature T_i, specific internal energy density ϵ_i and the nuclear binding energy per mass q_i. We look for the electron capture rate $\dot{Y}_{\rm e}$ and its corresponding neutrino energy loss rate per mass $\dot{q}_\nu$. To obtain the thermodynamics state in NSE, we solve the implicit equation

$$\epsilon_i - q_i = \epsilon_f(\rho, T_f, X_f) - q_f(\rho, T_f) + (m_n - m_p - m_e)N_A c^2 \dot{Y}_e(\rho, T_i, Y_{{\rm e},i}) + \dot{q}_\nu(\rho, T_i, Y_{{\rm e},i}). \quad (3)$$

Here, $\epsilon_f(\rho, T_f, X_f)$ and $q_f(\rho, T_f)$ are those for the final state. $(m_n - m_p - m_e)N_A c^2$ is the energy loss due to mass difference between neutron and electron-proton pair per mass. The above equation is solved by implicitly finding the T_f and its corresponding q_f such that the energy is balanced. The approximation $\dot{Y}_e(\rho, T_i, Y_{{\rm e},i})$ is true when the electron capture rate is much slower than dynamical timescale, which is true for SN Ia.

3. INITIAL MODELS

In this section we first describe the arrays of models we have performed for the SNe Ia using the sub-Chandrasekhar mass WD. Then we describe the explosion thermodynamics for each class of explosion.

In Tables 1 and 2 we tabulate the models studied for the double detonation model. The initial WD consists of a CO core and a He envelope. We regard the total WD mass M, the He envelope mass $M_{\rm He}$, the initial metallicity Z, and the position of the He detonation seeds as input parameters. The initial WD is assumed to be isothermal at a temperature of 10^8 K [1]. For $Z = 0.02$, we choose 49% ^{12}C and 49% ^{16}O and 2% ^{22}Ne in mass fractions, and for smaller Z, the mass fraction of ^{22}Ne is smaller and C and O have larger mass fractions in equal. For the He envelope, pure ^{4}He is assumed. Notice that the prescription of ^{22}Ne is not necessary the only element that represents metallicity. For example, in Shen et al. (2018), the ^{22}Ne mass fraction $X(^{22}\mathrm{Ne})$ scales as $Z = 1.1X(^{22}\mathrm{Ne})$. A more precise matching between the abundances from the stellar evolutionary models and the hydrodynamics simulations will require a more detailed isotope network.

It is shown that the actual C/O ratio can be sensitive to M and Z (Umeda et al. 1999). We remark that a direct extension for different C/O ratio is not straightforward since it requires first a quantitative study on how C-detonation is triggered as a function of density with a given composition.

To start the He detonation, we place a spherical detonation seed along the rotation symmetry axis. Due to resolution limit, the initial detonation seed is 1.5 times of the grid size in radius, i.e. 22 km. The position of the seed is regarded as an input parameter of the model, which ranges from 30 km to 300 km. The detonation seed consists of hot ashes of ^{56}Ni.

We notice that starting the explosion near the boundary may not be ideal in the two-dimensional models due to the possibility of enhancing nuclear burning along the symmetry boundary. But for our case, the detonation propagates much faster than typical fluid velocity. The hydrodynamical instabilities, especially Rayleigh-Taylor instability, do not have adequate time to grow before the fuel is swept by the detonation wave. So the boundary effect is less significant compared to the turbulent deflagration scenario. To construct the initial model, we choose models with a total mass $M = 0.9$ - $1.2\ M_\odot$ and $M_{\rm He} = 0.05$ - $0.35\ M_\odot$.

3.1. *Model Names*

[1] In general the WD can be away from isothermal profile due to the hydrostatic burning and convection. The exact profile depends on the competition between the compressional heating due to mass accretion and radiative cooling. In view of uncertainties during accretion, we neglect this factor and prepare identical initial models.

First we describe how these models are named and how they are chosen. Each model is named by their parameters, including M, $M_{\rm He}$, Z, and the initial position of the detonation bubble (sphere). For example, Model 105-050-2-50 stands for a WD with $M = 1.05\ M_\odot$, $M_{\rm He} = 0.05 M_\odot$, $Z = 0.02$ and the initial He detonation triggered at 50 km above the core-envelope interface.

The endings "-S50" and "-B50" stand for different initial He detonations. The term "S50" stands for a spherical detonation triggered at 50 km above the He/CO interface and "B50" stands for a belt (ring) around the "equator" of the WD. "R50" stands for a bubble triggered at 50 km above the He/CO interface. For "2R50" or "3R50" we put two or three "bubbles" (a combination of torus and bubble) in the He-envelope. Note that with the rotation and reflection symmetry, a bubble in the two-dimensional plane can be a "ring" if the bubble is away from the rotation-axis, in its three-dimensional projection. The distance 50 km is chosen such that the surface of the initial bubble is slightly separated by at least one grid from the interface. We find that this separation is necessary to avoid overlapping the initial He-detonation bubble with the CO-rich matter.

In Groups A - M in Table 1, the following effects are studied:
(1) Initial mass M: Groups A, B, C and M study the effects of progenitor mass on nucleosynthesis. For initial detonation with higher symmetry ("-S50" and "-B50" series), a lower He envelope mass $0.05\ M_\odot$ is used while for that with lower symmetry, the He envelope mass is fixed at $M_{\rm He} = 0.10$ or $0.15\ M_\odot$. Metallicity is fixed at the solar metallicity. The progenitor varies from 0.9 to $1.2\ M_\odot$.
(2) He envelope mass $M_{\rm He}$: In Groups D, E, F and G the effects of He envelope mass $M_{\rm He}$. Each group includes models of the same mass from 0.9 - $1.2\ M_\odot$ in a $0.1\ M_\odot$ interval, but with a different $M_{\rm He}$ from 0.05 to $0.2\ M_\odot$. In all models, solar metallicity is assumed. We remark that different $M_{\rm He}$ masses are used for different initial detonation geometries. It is because for a He detonation with a lower symmetry, the effects of shock convergence by geometry is smaller. To make sure the second detonation can be triggered for comparison, a higher $M_{\rm He}$ are studied.
(3) Metallicity Z: In Groups H, I and J we study the effects of metallicity to the explosive nucleosynthesis. Each group consists of models of the same M, $M_{\rm He}$ and detonation configuration. Models vary by their metallicity from 0 to 5 $Z_\odot$. We choose this large metallicity because in Leung & Nomoto (2018) we have already shown that such high metallicity model can be a clue to

Table 1. The model parameters and the global properties of the energetics and nucleosynthesis of the SNe Ia Model performed in this article. $E_{\rm nuc}$ and $E_{\rm tot}$ are the energy released by nuclear reaction and the total energy, in units of 10^{50} erg. M, $M_{\rm He}$ and $M_{\rm Ni}$ are the masses of the initial WD model, initial He envelope and the final synthesized ^{56}Ni in units of $M_\odot$. R, $R_{\rm seed}$ and $R_{\rm det}$ are the radii of the initial WD model, the distance of the initial detonation seed from the He/CO interface and the radius where the second detonation is started, in unit of km. $t_{\rm det}$ is the time when the second detonation is triggered. ρ_c and $\rho_{\rm det}$ are the initial central density and the density at which the second detonation is triggered, in units of 10^7 g cm^{-3}. The category "Type" classifies the final results into five types. "N" stands for no second detonation induced. "Y" stands for the second detonation which starts at location closer to the z-axis (the rotation symmetry axis). "X" stands for the second detonation which starts at a location closer to the r-axis (the symmetry plane axis). "D" stands for the second detonation which starts at somewhere between "Y" and "X" and "S" stands for the central detonation.

Group	Model	ρ_c	$M_{\rm He}$	$R_{\rm seed}$	M	R	$E_{\rm fin}$	$E_{\rm nuc}$	$t_{\rm det}$	$\rho_{\rm det}$	$R_{\rm det}$	$M_{\rm Ni}$	Type
A	090-050-2-B50	1.67	0.05	50	0.90	7160	3.82	5.08	2.71	1.00	4170	$< 10^{-2}$	"Y"
A	095-050-2-B50	2.26	0.05	50	0.95	6710	4.70	6.17	2.29	1.00	3860	0.11	"Y"
A	100-050-2-B50	3.21	0.05	50	1.00	6180	7.62	9.34	1.74	1.07	2870	0.31	"Y"
A	110-050-2-B50	6.17	0.05	50	1.10	4930	10.8	13.1	1.18	1.24	3770	0.68	"Y"
B	090-050-2-S50	1.67	0.05	50	0.90	7160	3.53	4.68	1.35	6.53	20	0.02	"S"
B	095-050-2-S50	2.26	0.05	50	0.90	6710	7.28	8.56	1.18	6.15	40	0.45	"S"
B	100-050-2-S50	3.21	0.05	50	1.00	6180	8.70	10.2	0.98	6.03	70	0.60	"S"
B	110-050-2-S50	6.71	0.05	50	1.10	4930	11.7	13.8	0.83	11.7	40	0.82	"S"
C	090-100-2-50	1.67	0.10	50	0.90	7160	-0.50	0.77	nil	nil	nil	$< 10^{-2}$	"N"
C	095-100-2-50	2.26	0.10	50	0.90	6710	-0.43	0.94	nil	nil	nil	$< 10^{-2}$	"N"
C	100-100-2-50	3.21	0.10	50	1.00	6180	-0.36	1.38	nil	nil	nil	$< 10^{-2}$	"N"
C	110-100-2-50	6.71	0.10	50	1.10	4930	11.1	13.0	0.94	1.04	3430	0.62	"X"
D	090-100-2-50	1.67	0.100	50	0.90	7160	-0.50	0.77	nil	nil	nil	$< 10^{-2}$	"N"
D	090-150-2-50	1.67	0.150	50	0.90	7160	5.65	7.04	2.35	1.51	2100	0.14	"Y"
D	090-200-2-50	1.67	0.200	50	0.90	7160	7.92	9.02	1.21	1.03	3940	0.28	"X"
D	090-300-2-50	1.67	0.300	50	0.90	7160	11.6	12.9	0.83	1.00	3370	0.54	"D"
E	100-050-2-50	3.21	0.050	50	1.00	6180	-1.45	0.27	nil	nil	nil	$< 10^{-2}$	"N"
E	100-075-2-50	3.21	0.075	50	1.00	6180	-1.08	0.63	nil	nil	nil	$< 10^{-2}$	"N"
E	100-100-2-50	3.21	0.100	50	1.00	6180	-0.36	1.39	nil	nil	nil	$< 10^{-2}$	"N"
E	100-150-2-50	3.21	0.150	50	1.00	6180	8.64	10.3	0.99	1.06	3370	0.47	"X"
E	100-200-2-50	3.21	0.200	50	1.00	6180	15.0	13.3	0.75	1.00	3360	0.61	"D"
F	110-050-2-50	6.17	0.050	50	1.10	4930	-1.89	0.39	nil	nil	nil	1.1×10^{-2}	"N"
F	110-075-2-50	6.17	0.075	50	1.10	4930	9.88	12.1	1.11	1.04	3560	0.56	"X"
F	110-100-2-50	6.17	0.100	50	1.10	4930	11.1	13.0	0.94	1.04	3430	0.62	"X"
F	110-125-2-50	6.17	0.125	50	1.10	4930	14.4	14.9	0.69	1.10	3270	0.78	"X"
F	110-150-2-50	6.17	0.150	50	1.10	4930	14.8	15.4	0.45	1.03	3190	0.69	"D"
F	110-200-2-50	6.17	0.200	50	1.10	4930	15.7	17.9	0.32	1.09	3000	0.79	"D"
G	120-050-2-50	14.8	0.050	50	1.20	4250	14.4	17.5	0.90	1.10	3010	0.83	"X"
G	120-100-2-50	14.8	0.100	50	1.20	4250	16.7	19.8	0.39	1.00	2790	0.92	"D"
G	120-150-2-50	14.8	0.200	50	1.20	4250	18.9	22.1	0.26	1.56	2570	0.96	"D"
G	120-200-2-50	14.8	0.150	50	1.20	4250	20.2	23.2	0.27	1.61	2440	1.00	"D"
H	090-150-0-50	1.67	0.150	50	0.90	7160	5.68	6.95	2.35	1.63	2080	0.15	"Y"
H	090-150-2-50	1.67	0.150	50	0.90	7160	5.77	7.04	2.35	1.51	2100	0.14	"Y"
H	090-150-6-50	1.67	0.150	50	0.90	7160	5.79	7.06	2.35	1.47	2100	0.14	"Y"
H	090-150-10-50	1.67	0.150	50	0.90	7160	5.80	7.07	2.35	1.73	2080	0.12	"Y"
I	110-100-0-50	6.17	0.050	50	1.10	4930	11.3	13.8	0.94	1.02	3430	0.67	"X"
I	110-100-2-50	6.17	0.100	50	1.10	4930	11.1	13.0	0.94	1.04	3430	0.62	"X"
I	110-100-6-50	6.17	0.050	50	1.10	4930	11.2	13.4	0.93	1.01	3410	0.51	"X"
I	110-100-10-50	6.17	0.050	50	1.10	4930	11.8	13.9	0.93	1.01	3410	0.52	"X"

Table 2. (*cont'd*) The initial models and their parameters.

Group	Model	ρ_c	$M_{\rm He}$	$R_{\rm seed}$	M	R	$E_{\rm fin}$	$E_{\rm nuc}$	$t_{\rm det}$	$\rho_{\rm det}$	$R_{\rm det}$	$M_{\rm Ni}$	Type
J	105-125-0-50	4.33	0.125	50	1.05	5300	9.85	12.2	0.96	1.06	3580	0.56	"X"
J	105-125-2-50	4.33	0.125	50	1.05	5300	10.3	15.2	0.94	1.04	3560	0.57	"X"
J	105-125-6-50	4.33	0.125	50	1.05	5300	10.3	12.4	0.96	1.03	3560	0.50	"X"
J	105-125-10-50	4.33	0.125	50	1.05	5300	10.0	11.9	0.96	1.04	3560	0.43	"X"
K	110-100-2-50	6.17	0.100	50	1.10	4930	11.1	13.0	0.94	1.04	3430	0.62	"X"
K	110-100-2-100	6.17	0.100	100	1.10	4930	11.1	13.1	0.93	1.04	3430	0.62	"X"
K	110-100-2-150	6.17	0.100	150	1.10	4930	11.8	13.6	0.93	1.06	3410	0.65	"X"
L	105-050-2-S50	4.33	0.050	50	1.05	5300	12.9	14.7	0.94	1.73	40	0.50	"S"
L	105-050-2-50	4.33	0.050	50	1.05	5300	-1.73	0.31	nil	nil	nil	8.6×10^{-3}	"N"
L	105-050-2-2R50	4.33	0.050	50	1.05	5300	9.61	11.6	1.48	4.63	3090	0.48	"Y"
L	105-050-2-3R50	4.33	0.050	50	1.05	5300	-1.67	0.33	nil	nil	nil	9.86×10^{-2}	"N"
M	090-150-2-50	1.67	0.150	50	0.90	7160	5.65	7.04	2.35	1.51	2100	0.14	"Y"
M	095-150-2-50	2.23	0.150	50	0.95	6710	8.64	10.1	1.33	1.00	4000	0.32	"X"
M	100-150-2-50	3.21	0.150	50	1.00	6180	8.64	10.3	0.99	1.06	3370	0.47	"X"
M	105-150-2-50	4.33	0.150	50	1.05	5300	13.6	14.7	0.73	1.04	3360	0.71	"X"
M	110-150-2-50	6.17	0.150	50	1.10	4930	14.8	15.4	0.45	1.03	3190	0.69	"D"
M	115-150-2-50	9.19	0.150	50	1.15	4550	16.5	17.7	0.33	1.09	2910	0.86	"D"
M	120-150-2-50	14.8	0.150	50	1.20	4250	18.9	22.1	0.26	1.56	2570	0.96	"D"

explain the observe SN remnants. For Groups H and I we pick these models because they are the benchmark models of our sub-Chandrasekhar mass SN Ia models. (4) Initial detonation geometry: In Groups K and L we study the effects of initial He detonation geometry. All models have the same M, $M_{\rm He}$ and at the solar metallicity. Group K consists of models with the detonation seed at different positions. Group L consists of models with different detonation geometry. It spans from different number of detonation "bubbles" to those with a higher symmetry, such as spherical detonation.

4. DETONATION TRIGGER

In the last column we classify the trigger mechanisms into four types. In all simulation groups (from Group C to M except Group L), all He detonations are started by placing an detonation spot at the radius 50 km along the rotation-axis. This mimics a single hot spot that induces thermonuclear runaway in the form of a bubble. In general, the detonation propagates along the He envelope without penetrating into the CO core. Depending on $M_{\rm He}$ and the interface density, different detonation types are observed.

4.0.1. *Type "N"*

Type "N" (no detonation) stands for no second detonation occurring. Type "N" can be found in models with a thin He envelope, the shock wave sent by the He detonation is not strong enough to compress the matter at both the center and the surface of the CO core. The CO core has a temperature always below the threshold temperature.

4.0.2. *Type "D"*

Type "D" (diagonal) stands for that the detonation first appears along elsewhere other than the symmetry axis. Type "D" occurs for models with high progenitor masses. In these cases, the typical density of interface can be as high as $\sim 10^7$ g cm^{-3}.

In Figure 1 we plot the temperature and explosion geometry for the Model 110-150-2-50 (D). When the detonation reaches the interface, the temperature of the CO matter can easily reach the critical temperature to start the CO detonation.

The temperature can reach 3×10^9 K where the shock penetrates. Notice that even the temperature in other detonated part can reach $\sim 2\times10^9$ K. The propagation is along the iso-density contour, where there is almost no heating in the radial direction. This makes no heating in the CO material. Therefore, while the He detonation is still burning the matter in envelope, the second detonation is already triggered.

4.0.3. *Type "X"*

Types "Y" and "X" stand for the detonation which is first started along the rotation axis (in x-y plane the y-axis) and symmetry axis (in x-y plane the x-axis).

Type "X" occurs when Type "D" cannot be started. This applies to models with lower M. Notice that in our simulations, a quarter of the star is simulated. When the detonation propagates, its burning rate increases due to the ring-shape structure, which has a local volume proportional to r. When the detonation approaches the symmetry-axis, the high velocity flow creates a strong compression of the remaining fuel. By symmetry, part of the fuel is compressed towards the core. This heats up the near-interface material and provides the required temperature for the first spot.

Figure 2 shows a typical "X"-type detonation for Model 110-100-2-50 (X). The second detonation is triggered at the r-axis, where the detonation wave compresses materials. The temperature due to the compression at the r-axis can be higher than the temperature rise in other regions due to detonation heating. As an example, the actual temperature can reach 3×10^9 K near the r-axis compared to other region which is $\sim 2\times10^9$ K. We remark that this shock heating is not related to the geometric convergence. Here, the detonation waves approach the symmetry boundary, i.e. two laminar detonation waves approaching each other (the collision site along the equator is locally flat).

4.0.4. *Type "Y"*

In Figure 3 we demonstrate the "Y"-Type detonation by using Model 110-050-2-B50 (Y) as an example. Type "Y" occurs when both Type "X" and Type "D" cannot be triggered beforehand. After the He shell is fully burnt, the first converging shock is not strong enough to detonate CO matter near interface. Instead, the mild shock continues to travel along the density-contour in the envelope. The flow creates another converging shock when the shock front returns to the rotation axis, which again creates the first hot spot for the C detonation.

4.0.5. *Type "S"*

Type "S" can be found in models with detonation seeds which have spherical symmetry, while the He envelope is not massive enough to ignite the near-interface C. The converging shock creates the hot spot at the center, where the geometric enhancement is the strongest.

In Figure 4 we plot Model 110-050-2-S50 (S). In contrast to the other 3 cases, the spherical detonation allows the envelope to be burnt much faster. In the plot, the He shell has expanded and cools down mostly, leaving almost a mild trace in the temperature distribution. On

the contrary, the center, where the C detonation starts, can reach as high as 6×10^9 K, sufficiently high for the burnt matter to reach NSE.

4.1. *Thermodynamics*

In Figure 5 we plot the maximum temperature against time for the four models presented. The letters in the figure correspond to the threshold temperature where the C detonation is triggered. The temperature needed to trigger the C detonation is the global maximum temperature in the simulations for Type "S", "X", "Y" detonations but not for Type "D" detonation. The global maximum temperature reaches its peak during the trigger of second detonation for Types "S", "X" and "Y". No such peak is observed for Type "D" detonation. Furthermore for Type "S" detonation, the maximum temperature when the C-detonation is triggered is the highest temperature reached in the simulation. This means that for a non-spherical trigger, even the hot ash can be higher than the threshold temperature, unless certain shock convergence occurs, the CO matter near interface can remain a temperature below the critical temperature.

Another feature is that in most cases, when the C detonation approaches the center, nuclear burning, despite at its low density, can be enhanced when the convergence effect is strong. This effect is robust under different resolution, and is even stronger when a finer resolution is used. It is because the shock strength can increase in the way $\sim 1/r$ for a cylindrical detonation and $\sim 1/r^2$ for a spherical. Locally, the density growth in the core will be higher for a finer resolution run, which allows more rapid reactions. However, globally the energy production will not diverge because the finer the resolution is, the smaller contribution such temperature peak gives. On the other hand, by using different geometry (e.g. Cartesian Coordinate) or higher dimensions (i.e. three-dimensional model), the level of shock convergence will be changed because it depends on how the geometry describes the structure with a high symmetry such as a ring or a sphere.

The peak temperature, albeit contributing to an extremely small amount of mass ($\sim 10^{-8-11} M_\odot$), can reach above 10^{10} K. One feature in "Y"-Type detonation does not appear in other types of detonation, namely the multi-peaks prior to detonation. This reflects the shock interaction from multiple detonations. For example, they correspond to the first collision of He detonations, the arrival of the reflected shock on the r-axis and the z-axis respectively.

This shows that the exact peak temperature can vary a lot depending on the geometric convergence. But how the convergence of shock and its subsequent divergence in temperature take place are related to the spatial resolution. In Appendix D we preform a numerical study to see how the spatial resolution affects the thermodynamics properties in local and global properties in some of the explosion models.

Below, we discuss the hydrodynamics behaviour of these models.

4.1.1. *Effects of He Envelope Mass*

In Groups D, E, F and M we cover the effects of $M_{\rm He}$ for different progenitor masses from 0.9 - 1.2 $M_\odot$. Some common trends can be seen in these series. At low $M_{\rm He}$, no second detonation can be triggered. By increasing $M_{\rm He}$, the second detonation can be triggered by "Y"-Type, "X"-Type and then "D"-Type in ascending $M_{\rm He}$. The created ^{56}Ni increases with $M_{\rm He}$. The explosion energy follows the same trend. Due to the change of detonation channel, the detonation trigger time becomes earlier for a higher $M_{\rm He}$. We remark that "S"-Type is independent from other three detonation types because it requires always a spherical He-detonation independent of $M_{\rm He}$. Models with a high $M_{\rm He}$ favours the "D"-Type detonation. For $M \geqslant 1.0\ M_\odot$, transition from "X"-Type to "D"-Type detonation occurs when $M_{\rm He} > 0.1 - 0.15\ M_\odot$. For $M \leqslant 1.0\ M_\odot$, transition from "Y"-Type to "X"-Type and then "D'-Type takes place for the transition $M_{\rm He}$ at 0.15 and 0.2 $M_\odot$ respectively. The critical $M_{\rm He}$ where no second detonation takes place depends on M, which decreases when M increases, and the detonation geometry. He-detonation with rotation or spherical geometry can trigger the second detonation with $M_{\rm He}$ as low as 0.05 $M_\odot$. For other types of He-detonation, the minimum value of $M_{\rm He}$ is $\sim 0.15 M_\odot$ for $M = 0.9 - 1.0\ M_\odot$, 0.1 $M_\odot$ for $M = 1.1\ M_\odot$ and 0.05 $M_\odot$ for $M = 1.2\ M_\odot$.

4.1.2. *Effects of Metallicity*

In Groups H, I and J we cover the effects of Z for three different models. The latter two are the benchmark models decided by its $M_{\rm Ni}$ at solar metallicity. We can see that metallicity has a very mild influence on the explosion energy and final energy. The detonation position, its channel and its trigger time are insensitive to Z. The major difference can be seen from the the ^{56}Ni mass, which drops when Z increases.

4.1.3. *Effects of detonation pattern*

In Groupd K and L we explore the effects of the detonation pattern, determined by its initial He detonation spot and its geometry. Again, all models share the same M, $M_{\rm He}$ and Z. The initial He detonation spot has

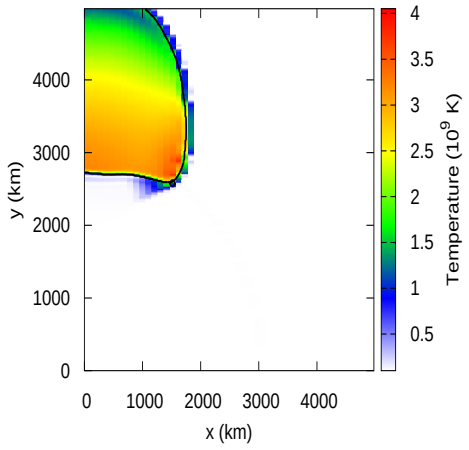

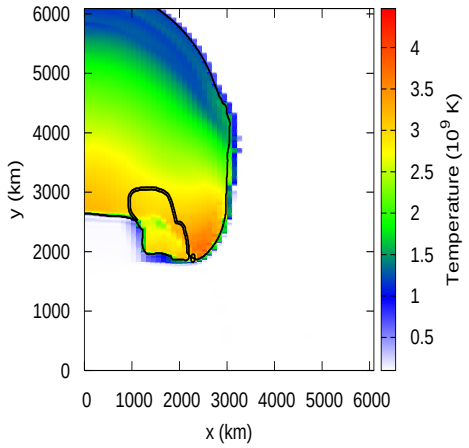

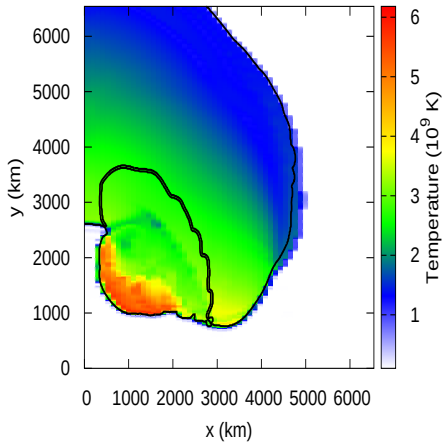

Figure 1. The flame and detonation geometry and the temperature for Model 110-200-2-R50 (D). The detonation is captured at -0.34, 0.03, 0.15 and 0.40 s from the detonation transition.

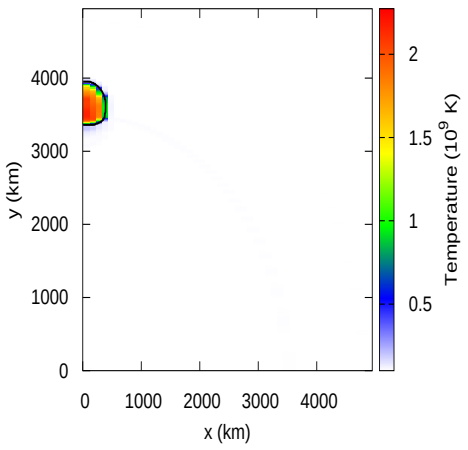

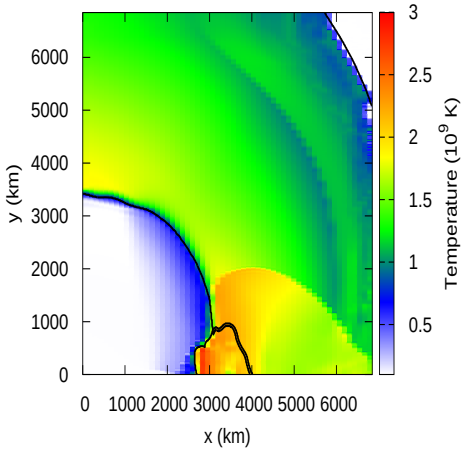

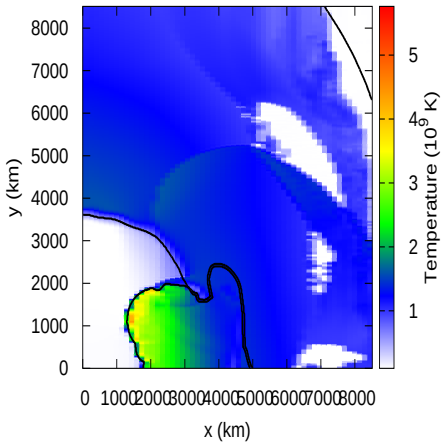

Figure 2. Similar to Figure 1, but for Model 110-100-2-R50 (Type "X"). The detonation is captured at -0.82, 0.15 and 0.40 s from the detonation transition.

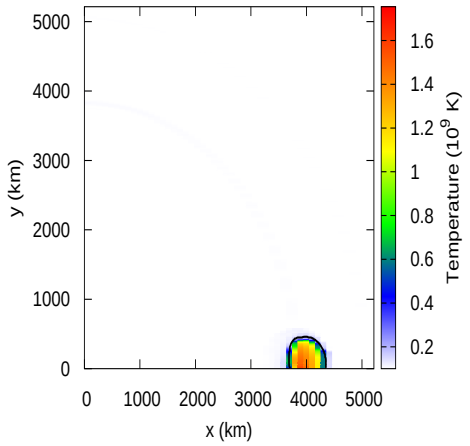

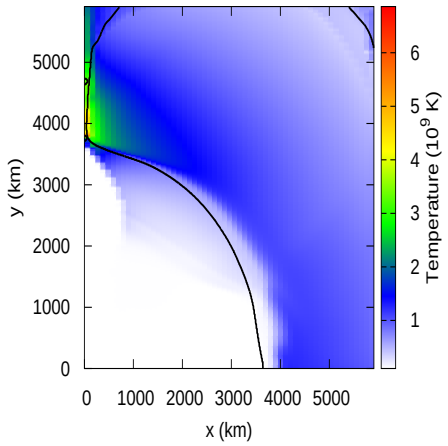

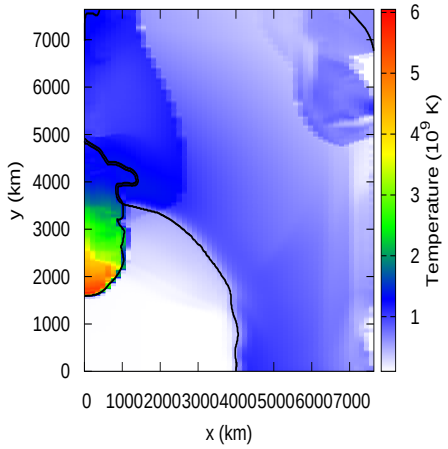

Figure 3. Similar to Figure 2, but for Model 110-050-2-B50 (Y). The detonation is captured at -0.98, 0.05 and 0.22 s from the detonation transition.

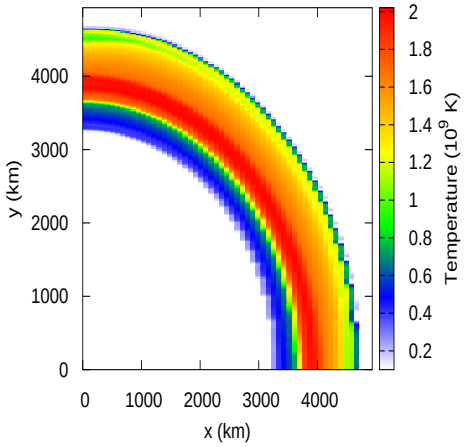

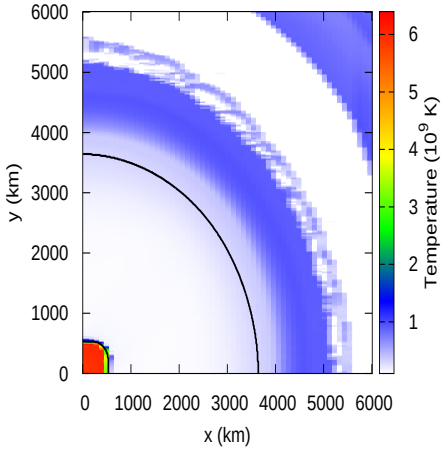

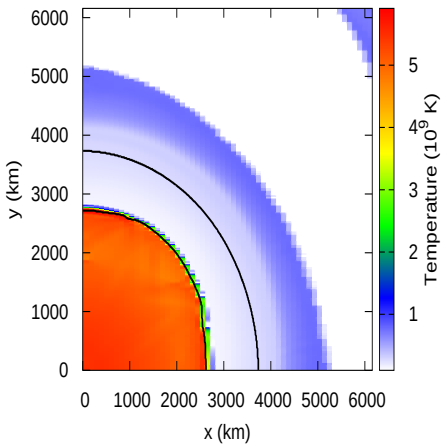

Figure 4. Similar to Figure 2, but for Model 110-050-2-S50 (S). The detonation is captured at -0.72, 0.08 and 0.32 s from the detonation transition.

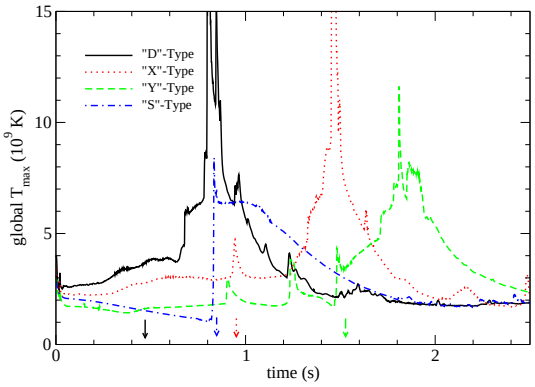

Figure 5. Maximum temperature in the simulations against time for Models 110-150-2-50 (D), 110-100-2-50 (X), 110-100-2-2R50 (Y)and 110-050-2-S50 (S) respectively. The arrows stand for the time where DDT is triggered for each model.

almost no impact on the explosion energetics and explosion properties. The Ni-production is also insensitive to the change of detonation position. On the other hand, the choices of detonation geometry is very influencing to the explosion properties. Some models (Models 105-050-2-50 (N) and 105-050-2-3R50 (N)) cannot trigger C detonation spontaneously while some (Models 105-050-2-S50 (S) and 105-050-2-2R50 (Y)) can. This reflects that the symmetry of the initial shock and how the detonation waves collide with each other determine the final fate of the WD. The resultant $M_{\rm Ni}$ can vary from $\sim 10^{-2}$ $M_\odot$ in a failed detonation to ~ 0.5 $M_\odot$ in a successful detonation. We note that Models 105-050-2-3R50 (N) and Model 105-050-2-2R50 (Y) behave differently. To show that the result is robust in our study, in Appendix E we do a resolution study to demonstrate how the trigger of C-detonation depends on the spatial resolution.

4.1.4. *Effects of Initial Mass*

In Group J we explore the effects of M on the explosion energetics. Compared to the near-Chandrasekhar mass WD studied in Leung & Nomoto (2018), the mass range for sub-Chandrasekhar mass is much wider (from 0.9 to 1.2 $M_\odot$). We do not explore mass below 0.9 $M_\odot$ since the central density of these models is below 10^7 g cm^{-3}, where the incomplete burning dominates. We also do not extend the upper bound to 1.3 $M_\odot$ since it is unclear, if there is nuclear runaway, whether the explosion is carried out as deflagration or detonation (Nomoto et al. 1976; Nomoto 1982b; Nomoto et al. 1984). We can see that when M increases, some effects are similar as increasing $M_{\rm He}$. The explosion energy increases. Also, the explosion time becomes earlier with its position being closer to the core. The detonation channel also changes from Type "Y" to Type "X" and then Type "D".

5. BENCHMARK MODELS

In this section, we study in details some models which behave most similar to a standard Type Ia supernova, determined by their ^{56}Ni production, which should be ~ 0.6 $M_\odot$ as observed in the majority of normal SNe Ia. Since there is a degeneracy in the models to produce this feature, we pick the one with the lowest amount of $M_{\rm He}$. We selected Models 110-100-2-50 (X), 100-050-2-S50 (S) and 110-050-2-B50 (Y). All of them have a healthy explosion of ^{56}Ni mass ~ 0.6 $M_\odot$.

In contrast, for sub-Chandrasekhar mass WD, we do not impose the constraints of Mn and Ni as what we have done in Leung & Nomoto (2018) because all models we built always underproduce Mn and Ni. Chosen by the ^{56}Ni production, there exists a degeneracy of models which satisfy this constraint. As a result, from each detonation trigger, we choose one model with $M_{\rm Ni} = 0.6$ $M_\odot$. They include Models 110-100-2-50 (X), 105-050-2-B50 (Y) and 100-050-2-S50 (S). No model with Type "D" produces an explosion with $M(^{56}{\rm Ni}) \sim 0.6 M_\odot$.

5.1. *Energy Evolution*

In Figure 6 we plot the time evolution of the total energy, kinetic energy, internal energy and gravitational energy for the benchmark models. Here we give an analysis on the energy evolution of only Model 110-100-2-50 (X). The other two benchmark models have similar evolution as this one, except at different detonation triggers and different He detonation convergence effects.

Before 0.9 s, there is only He detonation. The energy release $\sim 1 \times 10^{50}$ erg is insufficient to unbound the star due to the small amount of He and its low density. There is almost no change in the gravitational energy and kinetic energy. Almost all the energy change is reflected in the change of internal energy, showing that the He detonation does not influence the global dynamics. From 0.9 to 1.6 s C detonation takes place. The total energy sharply increases by 10^{51} erg at ~ 1.3 s, showing that the C detonation is rapidly turning the CO fuel into ash. At the same time, the internal energy, gravitational energy and kinetic energy increase. The C detonation is strong enough to heat up the WD, and causes the subsequent expansion. Beyond 1.6 s, the total energy remains a constant, signifying the end of both He and C detonations. Simultaneously, the internal energy drops while internal energy and gravitational energy increase and reach their equilibrium values at ~ 2 s. This corresponds to the phase that the thermalized ash is quickly expanding to accelerate the matter outwards until homologous expansion is developed.

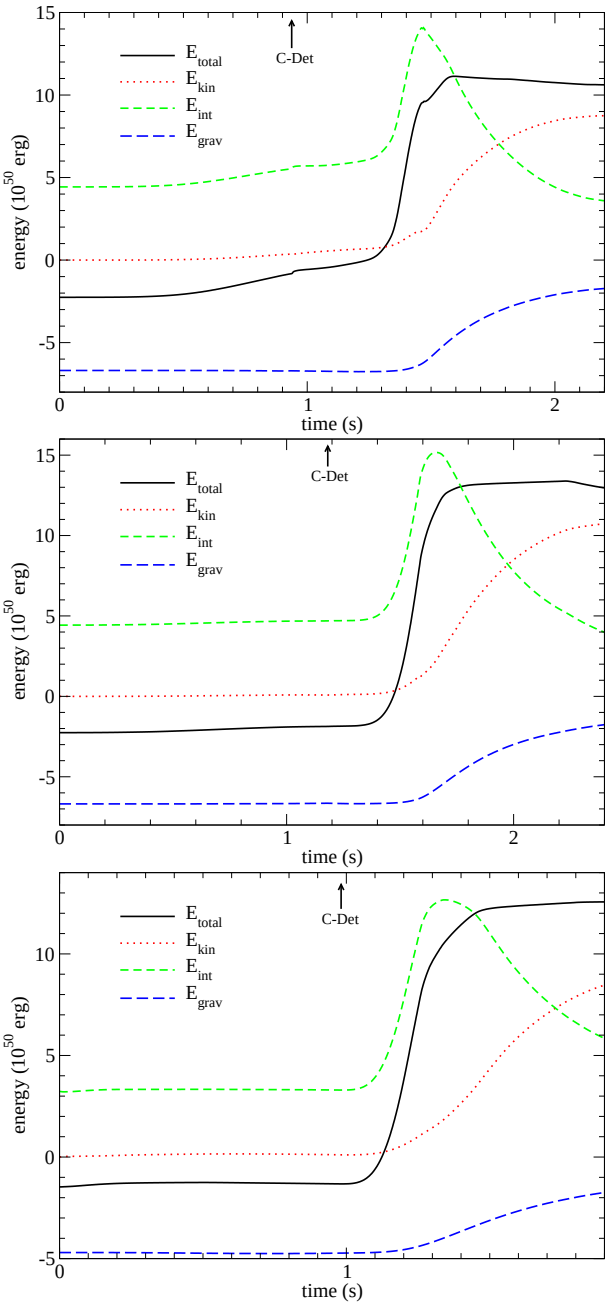

Figure 6. The total energy, kinetic energy, internal energy and gravitational energy against time for the Models 110-100-2-50 (X) (top panel), 110-050-2-B50 (Y) (middle panel) and 100-050-2-S50 (S) (bottom panel).

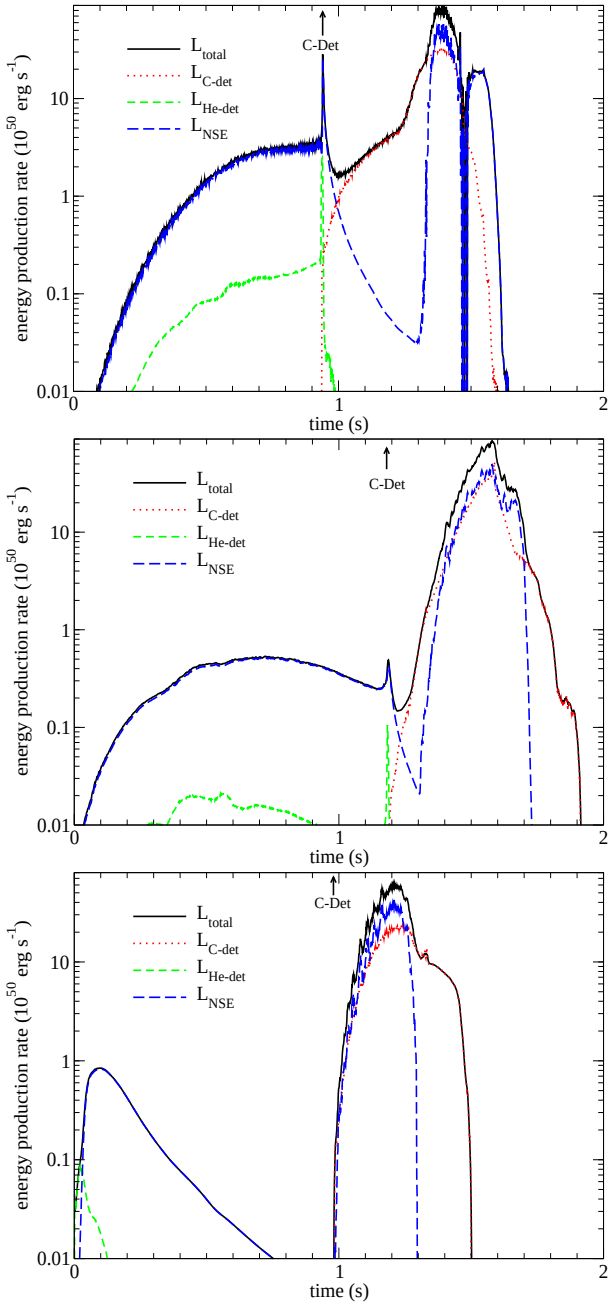

Figure 7. The total luminosity, C detonation luminosity, He detonation luminosity and NSE burning luminosity against time for Models 110-100-2-50 (X) (top panel), 110-050-2-B50 (Y) (middle panel) and 100-050-2-S50 (S) (bottom panel).

5.2. *Luminosity evolution*

In Figure 7 we plot the luminosity of the three benchmark models 110-100-2-50 (X), 110-050-2-B50 (Y), 100-050-2-S50 (S) in the top, middle and bottom panels respectively. First, we analyze the evolution of Model 110-100-2-50 (X).

Before 0.9 s, the total luminosity and the He detonation overlap with each other. This means most energy is produced directly from detonation where NQSE and NSE do not actively contribute to the energy evolution. There is a peak at 0.9 s, which is the moment where the He detonation reaches the symmetry axis. The compression causes a sudden jump in the density and temperature, which allows He burning to proceed much more efficiently. After that the He detonation ceases as there is not any pure He left but only partially burnt He in

the ash. At $t = 0.9$ s, the C burning takes place to the major nuclear reactions. But there is no advanced burning, showing that the detonation is still incinerating material in the low density region. At $t = 1.5$ s, the advanced burning exceeds the C detonation to become the major energy production channel. This shows that the detonation has finally reaches the center, which is dense and hot enough to carry out silicon burning up to NSE. Around 1.5 s, the C detonation begins to cease. Also, beyond 1.6 s, all matter becomes too cold or of too low density for further exothermic nuclear reactions to occur.

Model 110-050-2-B50 (Y) has a similar evolution to Model 110-100-2-50 (X) but has the "Y"-Type detonation. The shape of the energy production rates are similar but with two major differences. However the delay between the C-detonation and NSE luminosity rise is shorter than the Type-"X" detonation model. This feature is similar to the "S"-Type detonation (See below), despite its off center ignition. One reason is that during the geometric convergence, not only it heats up the CO-rich matter below the interface, but also generating a strong inward flow, which helps to guide the detonation reaching high density region. Such channeling is weaker in the "X"-Type model due to the absence of geometric convergence.

Model 110-050-2-S50 (S) is the "S"-Type detonation. It has a different structure from the other two by the absence of He-burning peak at the onset of second detonation and the similarity between the total luminosity and that by the NSE burning. Due to the detonation symmetry, there is no geometric convergence for the He-detonation. The He-detonation creates an inward moving shock while propagating outwards to burn the remaining He. Hence no luminosity peak during the transition is observed. Then, after the C-detonation is triggered, the total energy release, NSE burning and C-burning closely follow each other. It is because the detonation starts from the center. The higher density compared to the envelope allows the burning reaching NSE much shorter than dynamical timescale. This feature is not observed in Type "X"- or "Y"-Type detonation. At 1.3 s the energy production by C-burning drops rapidly, showing that the detonation wave has finished sweeping all C-fuel in the star. Accompanying with the expansion of the star, the recombination of ^{4}He into ^{56}Ni becomes the only energy production, which also ceases at 1.5 s.

5.3. *Chemical abundance*

We use the tracer particle scheme to reconstruct the detailed nucleosynthesis. The massless tracers are advected by the fluid motion, but have no effect on the fluid. They record the local density and temperature accordingly. Here we examine the typical chemical abundances of the three benchmark models presented in previous parts.

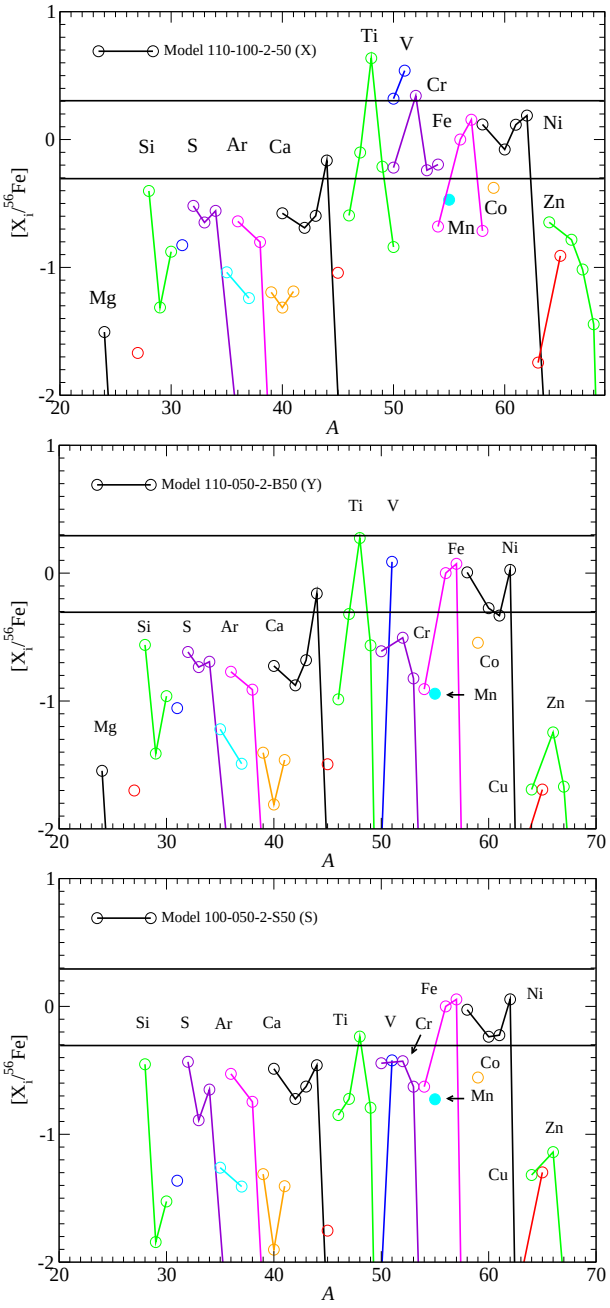

Figure 8. $[X_i/^{56}\mathrm{Fe}]$ after all short-lived isotopes have decayed for Models 110-100-2-50 (X) (top panel) and 110-050-2-B50 (Y) (middle panel) and 100-050-2-S50 (S) (bottom panel). $[X_i/^{56}\mathrm{Fe}]$ is defined as $\log_{10}(X_i/X(^{56}\mathrm{Fe})) - \log_{10}(X_i/X(^{56}\mathrm{Fe}))_\odot$. The upper and lower horizontal lines stand for two times and half of the solar value.

In Figure 8 we plot the final chemical abundance of the three benchmark models mentioned above. $[X_i/^{56}\mathrm{Fe}]$ is defined as $\log_{10}(X_i/X(^{56}\mathrm{Fe})) - \log_{10}(X_i/X(^{56}\mathrm{Fe}))_\odot$.

For Model 110-100-2-50 (X), the intermediate mass elements (IMEs)up to ^{40}Ca are underproduced. Starting from Ti, the production becomes similar to the solar abundance, where some of which are even overproduced, including ^{48}Ti, ^{51}V and ^{52}Cr. They are from 3 to 6 times higher than the observed solar values. Most Fe and Ni isotopes are very close to the solar values. Isotopes beyond Ni are underproduced. The pattern for Ni where ^{60}Ni and ^{62}Ni are more abundant can be observed. Also, as expected, ^{55}Mn, which comes mostly from the low electron fraction matter, is underproduced. In order to produce Mn, two channels are possible. First, Mn can be directly formed from NSE when the electron fraction of the matter is $Y_\mathrm{e} = 0.45$. Second, it is formed during alpha-chain burning of ^{52}Fe, where $^{52}\mathrm{Fe}(\alpha, p)^{55}\mathrm{Co}$. The ^{55}Co will later decay by $^{55}\mathrm{Co}(e^-, \nu_e)^{55}\mathrm{Fe}(e^-, \nu_e)^{55}\mathrm{Mn}$. The formation of ^{55}Co is favourable at $Y_\mathrm{e} = 0.49$. For pure C+O matter, the $Y_\mathrm{e} = 0.5$, therefore directly NSE burning without electron capture or alpha-chain burning cannot form seeds of ^{55}Mn, which is the case of sub-Chandrasekhar mass model.

For Model 110-050-2-B50 (Y), the nucleosynthesis pattern is very similar to the previous model. There are minor variations such as the much lower ^{50}V, and no trace of ^{54}Cr. This is because there is no shock convergence by the C detonation in the core due to the propagation direction. The effects of hot spot become less significant in this benchmark model.

For Model 100-050-2-S50 (S), the nucleosynthesis pattern is very different from the previous two models. Due to the imposed He detonation symmetry, much lower amount of He envelope mass is needed to trigger the C detonation. As a result, the resultant chemical pattern, related to He burning, is highly suppressed. A major drop of the abundances in $^{47-48}$Ti, ^{51}V, and ^{52}Cr becomes solar or even sub-solar. Other abundances, which are basically the C detonation products, remain the same as the two other models.

5.4. *Ejecta Composition*

In Figures 9 we plot the velocity distribution of some representative isotopes for the benchmark Models 110-100-2-50 (X), 110-050-2-B50 (Y) and 100-050-2-S50 (S) in the left, middle and right panels respectively. We extract the chemical abundances and velocities of the tracer particles.

In Model 110-100-2-50 (X), this benchmark model possesses both the typical sub-Chandrasekhar mass SN Ia ejecta profile with asymmetric effects. Here, we refer to e.g. Shigeyama et al. (1992) for a typical sub-Chandrasekhar mass SN Ia. For the typical one, we can see in the core, up to 10000 km s^{-1}, the ejecta is made of mainly $^{56-58}$Ni. Beyond that, IMEs, including ^{28}Si, ^{32}S, ^{36}Ar and ^{40}Ca become more abundant. However, in this model ^{56}Ni remains the most abundant almost throughout the star within $v < 13000$ km s^{-1}. Traces

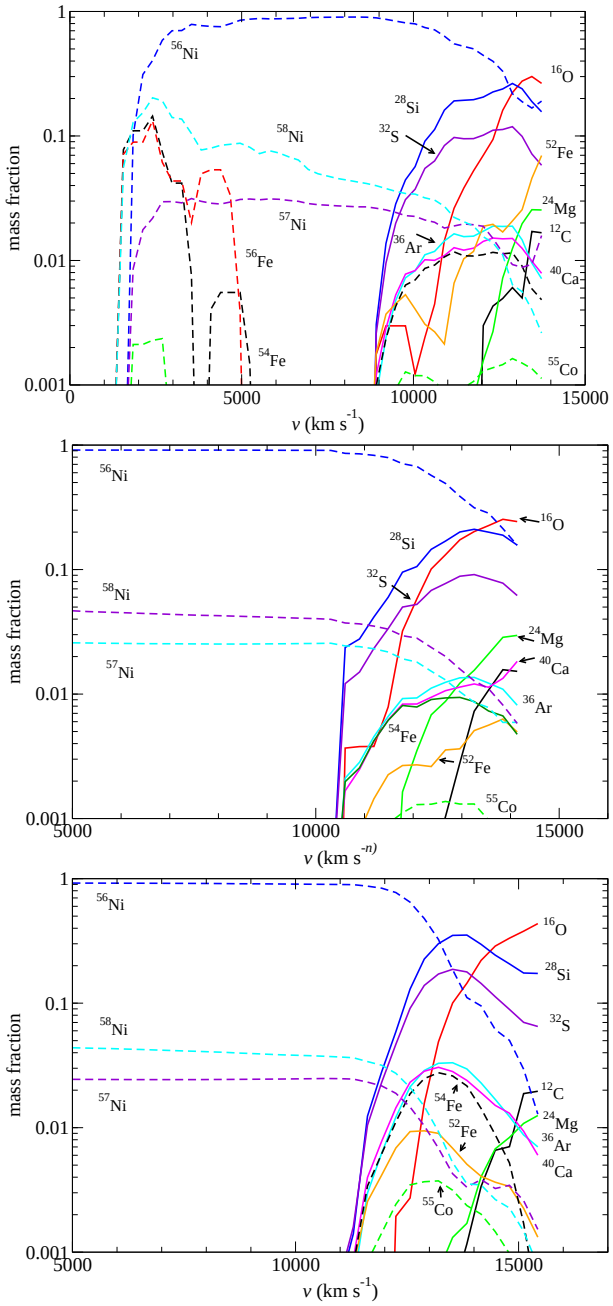

Figure 9. The mass fraction against velocity of the final abundance before the decay of short-live isotopes for the benchmark models 110-100-2-50 (X) (upper panel), 105-100-2-B50 (Y) (middle panel) and 100-050-2-S50 (S) (lower panel).

of ^{12}C and ^{16}O can be found when $v > 12000$ km s^{-1}. They correspond to the products from the incomplete C burning. These features are common to all three benchmark models presented here.

In Model 110-100-2-50 (X) and 110-050-2-B50 (Y), we can see a mild rise of ^{52}Fe near the surface. Also, ^{54}Fe remains to maintain a few percent mass fraction even to the outermost ejecta. They come from He burning, especially when there is shock convergence or detonation wave collision. The further compressional heating with this hydrodynamical origin can enhance the formation of these isotopes. On the other hand, we see a clear cut of ^{54}Fe inside the outermost ejecta of Model 100-050-2-S50 and ^{52}Fe has a clear falling trend when $v > 13000$ km s^{-1}.

Major differences appear in the innermost part of the ejecta because of the C detonation convergence. As discussed in previous sections, the further C detonation induced geometric convergence can create hot spot which allows the matter to be heated up to a temperature above it can normally reach through simple detonation. In that sense, this allows a small part of matter to undergo complete burning and even electron capture. This property can be found in Model 110-100-2-50 (X). We can see that at the innermost part of the ejecta, neutron-rich isotope including ^{54}Fe and ^{56}Fe are produced. Some ^{55}Co can be even produced. Notice that these features are usually found in the Chandrasekhar mass model (See e.g. Nomoto (1984); Iwamoto et al. (1999) for the detailed ejecta profile of some classical models). This demonstrates that the asphericity of the He detonation and hence the C detonation can be reflected by the low-velocity ejecta.

5.5. *Thermodynamics*

In Figure 10 we plot the $\rho_{\rm max}$ against $T_{\rm max}$ for the benchmark model obtained from the tracer particles. The sampling is done by grouping the tracer particles into bins according to their $\rho_{\rm max}$, which is defined by their individual thermodynamics history. Then the average, upper and lower limits of $T_{\rm max}$ in each density bin is taken. $T_{\rm max}$ is also the maximum value in the thermodynamics history. In most cases, the particle achieves its $\rho_{\rm max}$ and $T_{\rm max}$ is at the same time, when the detonation wave swept across the particle. However, in the case where multiple detonation shocks appear, the two moments can be non-simultaneous. Notice that the initial central density of this model is $\sim 6 \times 10^7$ g cm^{-3}. Due to the shock wave compression, which is further enhanced by the geometric convergence as well as shock wave collision, the matter can reach a maximum density as high as 3×10^8 g cm^{-3}. Together with the rise of the density, the temperature can rise as high as 7×10^9 K. Certain particles which are directly under shock interaction, can reach a maximum density 5×10^8 g cm^{-3} with a maximum temperature of 9×10^9 K. This can compared with Figure 12 in Leung & Nomoto (2018). In that figure, the tracer particles show a uniform $\rho_{\rm max}$ against $T_{\rm max}$ for the particles inside deflagration zones and a spread of $T_{\rm max}$ in the detonation zone. Our model here shows a similar behaviour for the detonation, except that the effects are more pronounced because of the inward motion during the shock propagation.

At last in Figure 11 we plot also the final Y_e of the tracer particles against $T_{\rm max}$. We can see three groups of particles. The first group is the particle from the He envelope. It has a uniform final $Y_{\rm e} = 0.5$ which has a density from 10^{6-8} g cm^{-3}. This shows that the He envelope has in general low density where electron capture processes are inefficient. The second group is the $10^6 - 5 \times 10^8$ g cm^{-3}. This corresponds to the tracer particles experiencing single pass of detonation wave. The final Y_e shows a mildly decreasing function as $\rho_{\rm max}$, which suggests that electron capture becomes important at near 10^8 g cm^{-3}. The third group of particles are those with Y_e from 0.47 - 0.495 with a $\rho_{\rm max}$ from $5 - 10 \times 10^8$ g cm^{-3}. This corresponds to tracer particles which are excited by shock compression. There are much fewer particles of this types since it occurs to the particles very close to the symmetry boundary or lying inside the collision site of C detonation shock. Again, this figure can be compared with Figure 12 in Leung & Nomoto (2018). In that figure, the distribution of particles is more uniform and there exists a one-one correspondence for a given $\rho_{\rm max}$ to final $Y_{\rm e}$. In this work, this correspondence is broken down because of the He envelope. Also, the pronounced shock interactions provide a wider diversity to the thermodynamics history in the tracer particles.

6. NUCLEOSYNTHESIS

To calibrate the nucleosynthesis yield, we use the post-process scheme as described in Travaglio et al. (2004); Seitenzahl et al. (2010). In the hydrodynamics simulations we place massless particles which record the thermodynamics history of the local density and temperature of the Eulerian grid. The density and temperature evolution, together with the initial chemical composition depending on its initial position, are sent to the nuclear reaction network to calculate the chemical abundance of the corresponding model. Similar to previous works, we use the nuclear reaction network as developed in Timmes (1999). It includes a network of 495 isotopes ranging from ^{1}H to ^{91}Tc. The nuclear reaction rates are up-

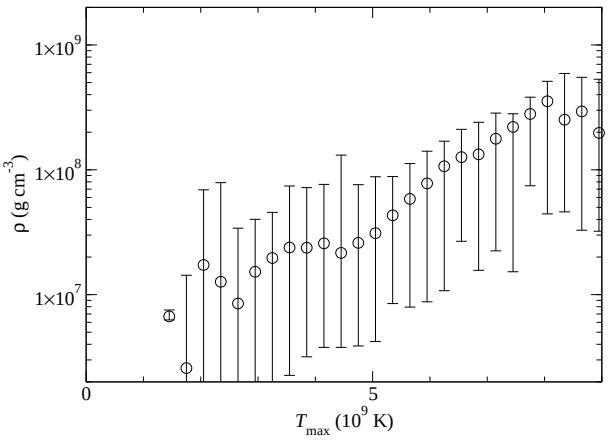

Figure 10. The $\rho_{\rm max}$ against $T_{\rm max}$ for the benchmark model obtained from the tracer particle thermodynamics histories for the Model 110-100-2-50 (X). The error bars stand for the temperature ranges of the tracer particles at a specific density bin with the circle being the average.

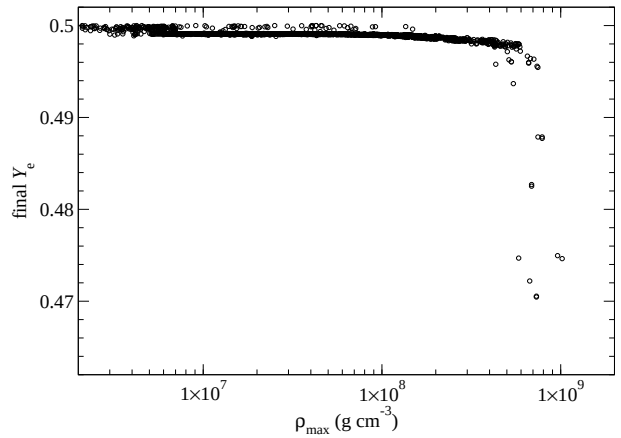

Figure 11. Same as Figure 10 but for the final $Y_{\rm e}$ against $\rho_{\rm max}$ for the benchmark model 110-100-2-50 (X) obtained from the tracer particle thermodynamics histories.

dated by the values provided in Rauscher & Thielemann (2000). We include the electron screening by Kitamura (2000) and Benvenuto et al. (2015). The formula aims for strong electron screening, and it reduces to the weak electron screening given in Abe (1959). We include the corresponding free energy for the calculation of NSE as described in Seitenzahl et al. (2010). The chemical potential assumes classical ideal gas form, which is suitable for the density ($\sim 10^9$ g cm^{-3}) and temperature (10^9 K) used here. We have also updated electron capture rate table by including the rate table from Nabi & Klapdor-Kleingrothaus (1999, 2004). We use this rate table when there is no rate given in the original version of the nuclear reaction network, although we remark that the electron capture and its related weak interaction processes are of less importance due to the typically lower density than the near-Chandrasekhar mass explosion model.

6.1. *Dependence on WD Mass*

6.1.1. *One-Bubble Configuration*

In Figure 12 we plot $[X_i/^{56}{\rm Fe}]$ for the isotopes from Models 105-100-2-50 (X), 110-100-2-50 (X), 115-100-2-50 (D) and 120-100-2-50 (D). The isotopes are obtained from the nucleosynthesis by the post-processing as described above, but after all short-live isotopes decayed. In practice after the nucleosythesis yield is computed by post-processing, we allow further radioactive decays by computing the network while suppressing thermonuclear reactions. We fixed the period to be 10^6 years. The period is chosen to be long enough to allow certain long lived isotopes, such as ^{59}Ni, to completely decay to compute the asymptotic chemical yield. But we also note that there are still some isotopes with even longer half-lives, such as ^{27}Al and ^{60}Fe.

These models in this figure have the same configurations by setting the same $M_{\rm He}$, initial He detonation pattern and metallicity. As a result, the mass of the CO fuel increases when the total mass increases. By increasing the mass, there is a systematic decrease in $[X_i/^{56}{\rm Fe}]$. This is because when the mass increases, the produced ^{56}Ni increases as shown in Table 1. The final ^{56}Fe yield thus increases. For IME, there is a drop from Mg to Ca by a factor of $\sim O(1)$. Similar effects are observed in Fe-peak isotopes. This shows that when the mass increases, the extra ash contributes to the production of ^{56}Fe. Therefore, the qualitative features of the mass fraction remain.

Nevertheless, even for the massive progenitor like Model 115-100-2-50 (D), the over-production of ^{48}Ti cannot be resolved as they are mostly produced in the He envelope. Some of the isotopes, such as ^{51}V, ^{52}Cr and ^{70}Zn, become comparable to the solar abundance when $M = 1.15\ M_\odot$. However, compared to the Chandrasekhar mass SN Ia, none of the isotopes shows a drastic boost when M increases. This can be compared to the Chandrasekhar mass WD scenario, by increasing the mass from 1.30 to 1.37 $M_\odot$, some of the isotopes, such as ^{54}Cr and ^{60}Fe, can be drastically enhanced. One reason is that the density related to the sub-Chandrasekhar mass model is low that the electron capture does not play an important role in most parts of the star. The major changes come from the increment of ^{56}Ni, which systematically lowers all mass fractions of all isotopes.

6.1.2. *One-Ring Configuration*

In Figure 13 we plot similar to Figure 12 but for Models 090-050-2-B50 (Y), 095-050-2-B50 (Y), 100-050-2-B50 (Y) and 110-050-2-B50 (Y)respectively. These

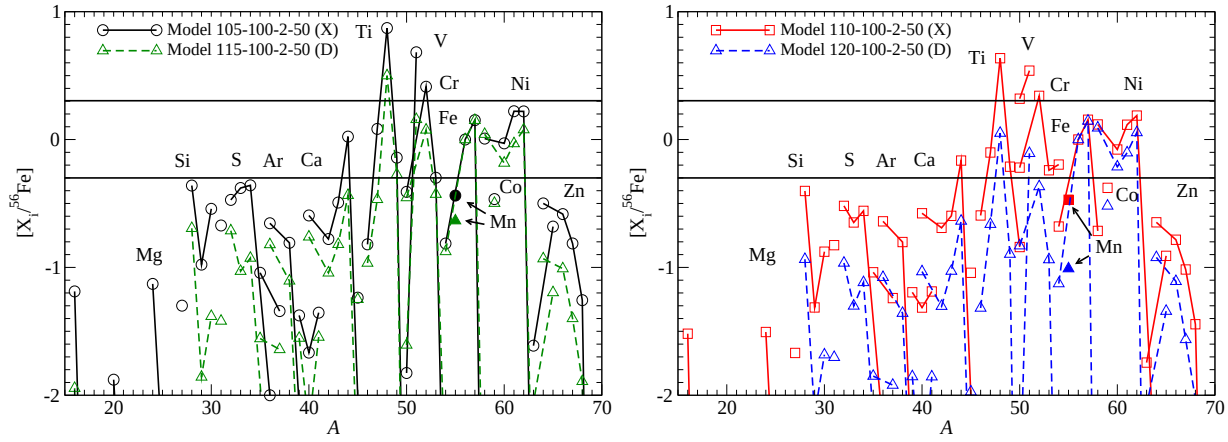

Figure 12. $[X_i/^{56}\mathrm{Fe}]$ for Models 105-100-2-50 (X) ($M = 1.05\ M_\odot$) and 115-100-2-50 (D) ($M = 1.15\ M_\odot$) in the left panel and Models 110-100-2-50 (X) ($M = 1.10\ M_\odot$) and 120-100-2-50 (D) ($M = 1.20\ M_\odot$) in the right panel. All models assume $M_{\rm He} = 0.1\ M_\odot$, $Z = 0.02$ and a bubble-shape initial He-detonation at 50 km above the CO-envelope interface.

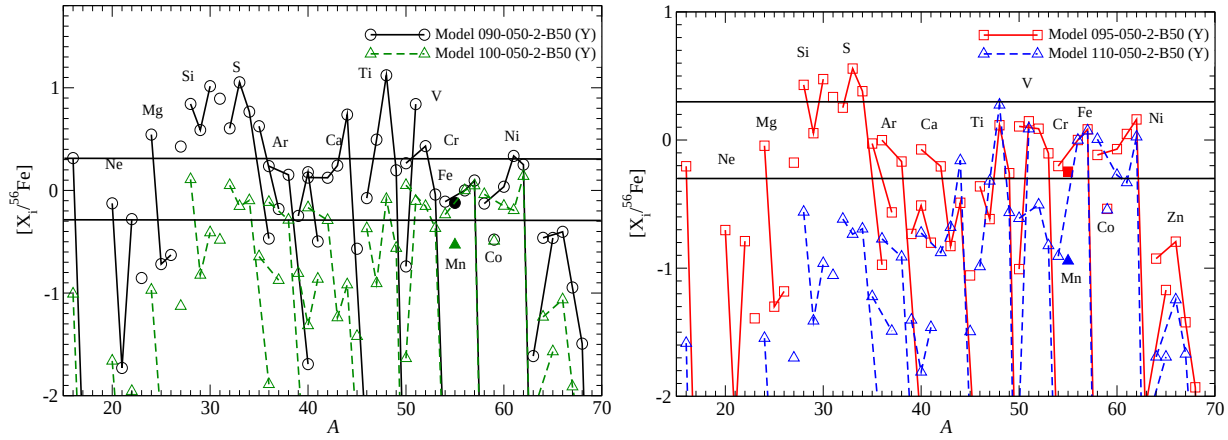

Figure 13. $[X_i/^{56}\mathrm{Fe}]$ fractions for Models 090-050-2-B50 (Y) ($M = 0.90\ M_\odot$) and 100-050-2-B50 (Y) ($M = 1.00\ M_\odot$) in the left panel and Models 095-050-2-B50 (Y) ($M = 0.95\ M_\odot$) and 110-050-2-B50 (Y) ($M = 1.10\ M_\odot$) in the right panel. All models assume $M_{\rm He} = 0.05\ M_\odot$, $Z = 0.02$ and a belt-shape initial He-detonation at 50 km above the CO-envelope interface.

models correspond to the series of models of the same $M_{\rm He}$ but at different masses, each with the same initial He detonation by a He ring. Due to the detonation symmetry which may trigger the second detonation with a lower He mass, the effects of the He incomplete burning products, such as Ti, V and Cr become better fit to the solar abundance. The qualitative trends for an increasing mass can be observed.

At lower mass, the lower production of ^{56}Ni causes a strong overproduction of elements like Si, S. Ti and V are overproduced but this feature is suppressed at Model 090-050-2-B50 (Y). As mass increases, the relative productions of IMEs drop. This includes Si, S, Ar and Ca. Relative productions of Ti, V and Cr also decrease when the mass increases, but they remain saturated around the solar values. Fe and Ni are overall insensitive to the mass change.

6.1.3. *Spherical Configuration*

In Figure 14 we plot similar to Figure 12 but for Models 090-050-2-S50 (S), 095-050-2-S50 (S), 100-050-2-S50 (S) and 110-050-2-S50 (S) respectively, using the spherical He detonation as the initial trigger. Again, the higher He detonation symmetry allows triggering the second detonation at a lower He envelope. The overproduction of intermediate α-chain burning production is less severe for the models with a normal amount of ^{56}Ni ($\sim 0.6\ M_\odot$). Due to the spherical symmetry, the second detonation all starts at the core for all models, so that the variations of elements become more regular.

The IMEs Si, S, Ar and Ca show a flat distribution and decrease with an increasing mass. The over-productions of ^{50}Ti, ^{51}V and ^{52}Cr as the major products in He detonation before reaching ^{56}Ni, are largely suppressed once the mass reaches above $0.95\ M_\odot$. The isotopes of Fe remain non-sensitive to the variation of mass except for

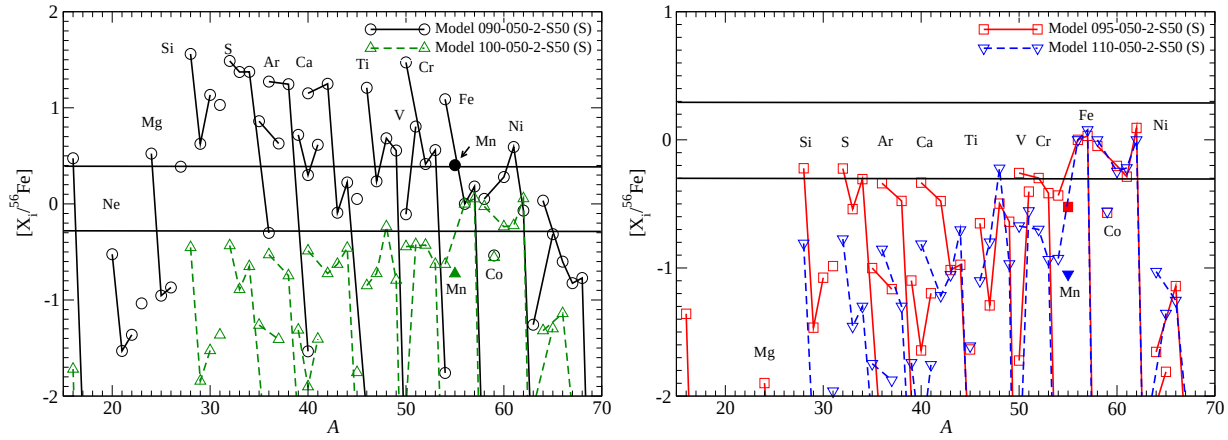

Figure 14. $[X_i/^{56}\mathrm{Fe}]$ for Models 090-050-2-S50 (S) ($M = 0.90\ M_\odot$) and 100-050-2-S50 (S) ($M = 1.00\ M_\odot$) in the left panel and Models 095-050-2-S50 (S) ($M = 0.95\ M_\odot$) and 110-050-2-S50 (S) ($M = 1.10\ M_\odot$) in the right panel. All models assume $M_{\rm He} = 0.05\ M_\odot$, $Z = 0.02$ and a spherical initial He-detonation at 50 km above the CO-envelope interface.

^{54}Fe. A systematic drop of ^{55}Mn can also be seen, showing that the amount of ^{55}Mn is not increased significantly when the mass increases.

6.2. *Dependence on He Envelope Mass*

6.2.1. *One-Bubble Configuration*

In Figure 15 we plot similar to Figure 12 but for Models 110-075-2-50 (X), 110-100-2-50 (X), 110-125-2-50 (X) and 110-150-2-50 (D). This series of model have also the same configurations except for the He envelope mass. Notice that among these models, Model 110-150-2-50 (D) has a different detonation mechanism as it has "D"-Type detonation instead "X"-Type detonation. By increasing $M_{\rm He}$, the mass fractions of IMEs reduce. However, by comparing Models 110-125-2-50 (X)and 110-150-2-50 (D), the IME mass fractions increase. This is because the "Y"-Type detonation allows an earlier detonation, which ensures that the low density matter is well detonated before it expands and the density becomes too low for nuclear reaction. For Fe-peak elements, clear trends can be seen in elements like Ti, Cr and V. Again a decreasing trend is observed when $M_{\rm He}$ increases but there is not much difference in Fe and Ni.

6.2.2. *One-Ring Configuration*

In Figure 16 we plot similar to Figure 15 but for Models 100-050-2-B50 (Y), 100-100-2-B50 (Y), 110-050-2-B50 (Y) and 110-100-2-B50 (Y), where all models share the same initial masses $M = 1.00$ and $1.10\ M_\odot$ and He detonation configuration. Different He envelope masses are used. We remind that Model 110-050-2-B50 (Y) is the benchmark model and we choose a progenitor mass for comparison to extract the effects of $M_{\rm He}$ at different mass.

For $M = 1.10\ M_\odot$, the chemical abundances do not change strongly with $M_{\rm He}$. It is because the overall production is dominated by ^{56}Ni. A small suppression of IMEs for ^{28}Si, ^{32}S and ^{36}Ar can be observed. Almost no change can be found for Fe-peak elements from Ti to Ni. On the other hand for $M = 1.00\ M_\odot$, the chemical abundances scale strongly with $M_{\rm He}$. Besides the more obvious drop in the IMEs, there is a huge jump in ^{48}Ti. ^{51}V and ^{52}Cr when $M_{\rm He}$ increases. Again, Fe-peak elements like Fe, Mn and Ni are less changed by $M_{\rm He}$.

6.2.3. *Spherical Configuration*

In Figure 17 we plot similar to Figure 15 but for the Models 090-050-2-S50 (S), 090-100-2-S50 (S), 100-050-2-S50 (S) and 100-100-2-S50 (S). The models consist of initial masses of 1.00 and 1.10 $M_\odot$. All models assume a spherical He detonation as the initial trigger. Again we remind that Model 100-050-2-S50 is the benchmark model of this work.

For the spherical model, due to its stronger explosion, a lower mass model is used for the benchmark model. So compared to the one-ring structure, the effects of He envelope are larger. Besides a more prominent decrease in IMEs, the α-chain products including ^{48}Ti, ^{52}Cr and ^{51}V are vastly increased for a more massive He envelope. No significant change is observed for Fe, Mn and Ni. The effects are more significant for the lower mass cases due to a smaller ^{56}Ni mass. A flat distribution in ^{28}Si, ^{32}S, ^{36}Ar, ^{40}Ca, ^{42}Ca, ^{44}Ti and ^{48}Cr can be seen. The ^{55}Mn is even over-produced because of the suppressed ^{56}Ni and hence ^{56}Fe. A higher $M_{\rm He}$ results in a global suppression of this relative production rate.

6.3. *Dependence on Metallicity*

6.3.1. *One-Bubble Configuration*

In Figure 18 we plot $[X_i/^{56}\mathrm{Fe}]$ of stable isotopes after all short-lived radioactive isotopes have decayed for

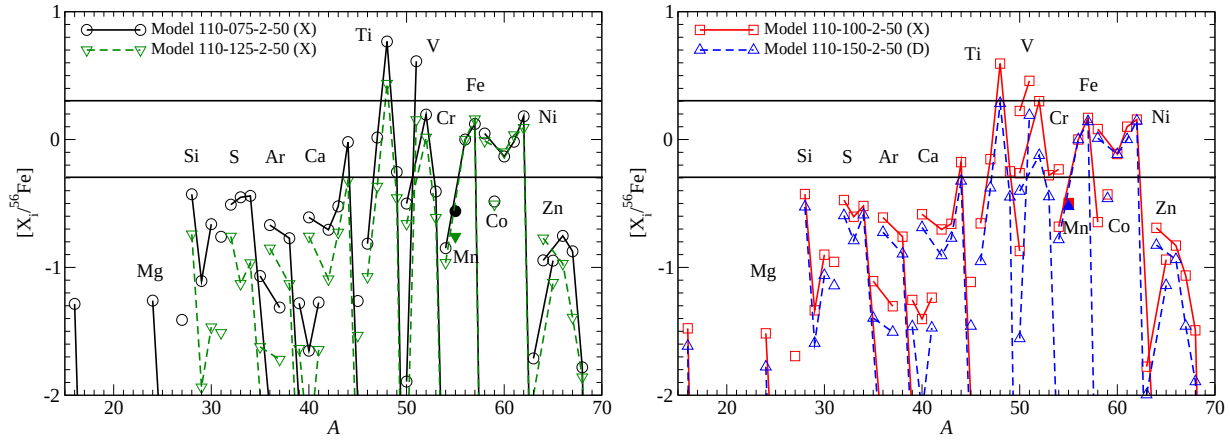

Figure 15. $[X_i/^{56}\mathrm{Fe}]$ for models comparing the effects of He envelope mass including Models 110-075-2-50 (X) ($M_{\rm He}$ = 0.075 $M_\odot$), and 110-125-2-50 (X) ($M_{\rm He}$ = 0.125 $M_\odot$) in the left panel and Models 110-100-2-50 (X) ($M_{\rm He}$ = 0.100 $M_\odot$) and 110-150-2-50 (D) ($M_{\rm He}$ = 0.150 $M_\odot$) in the right panel. All models assume M = 1.10 $M_\odot$, Z = 0.02 and a bubble-shape initial He-detonation at 50 km above the CO-envelope interface.

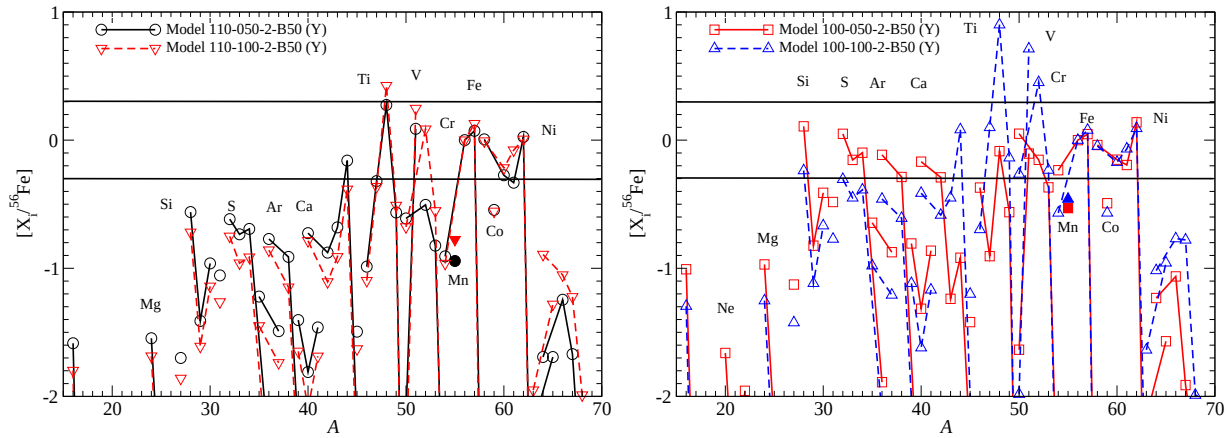

Figure 16. Similar to Fig. 15, but for Models 100-050-2-B50 (Y) (M = 1.00 $M_\odot$) and 110-050-2-B50 (Y) (M = 1.10 $M_\odot$) in the left panel and Models 100-100-2-B50 (Y) (M = 1.00 $M_\odot$) and 110-100-2-B50 (Y) (M = 1.10 $M_\odot$) in the right panel. All models assume $M_{\rm He}$ = 0.05 (0.10) $M_\odot$ in the left (right) panel, Z = 0.02 and a belt-shape initial He-detonation at 50 km above the CO-envelope interface.

Models 110-100-0-50 (X), 110-100-2-50 (X), 110-100-6-50 (X) and 110-100-10-50 (X). Similar to Chandrasekhar mass SNe Ia (Leung & Nomoto 2018), metallicity is important to the production of isotopes with a neutron-proton ratio close to the unity. Also, the presence of ^{22}Ne slightly lowers the energy release of C detonation. We can observe a boost of IMEs including ^{30}Si, ^{34}S, ^{38}Ar, ^{42}Ca. The boost factors can be as large as beyond two orders of magnitude when the metallicity increases from 0 to 5 $Z_\odot$. For Fe-peak elements, we also observe a boost in the production ^{46}Ti, ^{50}Cr ^{54}Fe, ^{55}Mn, ^{58}Ni. The boost can range from ten to hundred when contrasting the Models 110-100-0-50 (X) and 110-100-10-50 (X). In Tables 7, 8, 10, 11, 13 and 14 we tabulate the masses of the stable isotopes in different metallicity for the benchmark models based on Models 110-100-2-50 (X), 100-050-2-B50 (Y) and 110-050-2-S50 (S). By comparing models with the same configuration but different metallicity, it can be seen that when metallicity increases, IMEs with a high neutron ratio are boosted sharply. For example, we observe a clear increasing trend for $^{29-30}$Si, ^{34,36}S, ^{37}Cl, ^{38}Ar and ^{40}K and so on. The jump can be as high as four orders of magnitude from zero metallicity to 5 $Z_\odot$. For Fe-peak elements, we have ^{46}Ti, ^{50}V, ^{50}Cr, ^{54}Fe and ^{58}Ni to be the representative isotopes. The results here are very similar to those in Chandrasekhar mass WD.

6.3.2. *One-Ring Configuration*

In Figure 19 we plot similar to Figure 18 but for the Models 110-050-0-B50 (Y), 110-050-2-B50 (Y), 110-050-6-B50 (Y) and 110-050-10-B50 (Y). This series of models focus on the effects of metallicity for the same progenitor

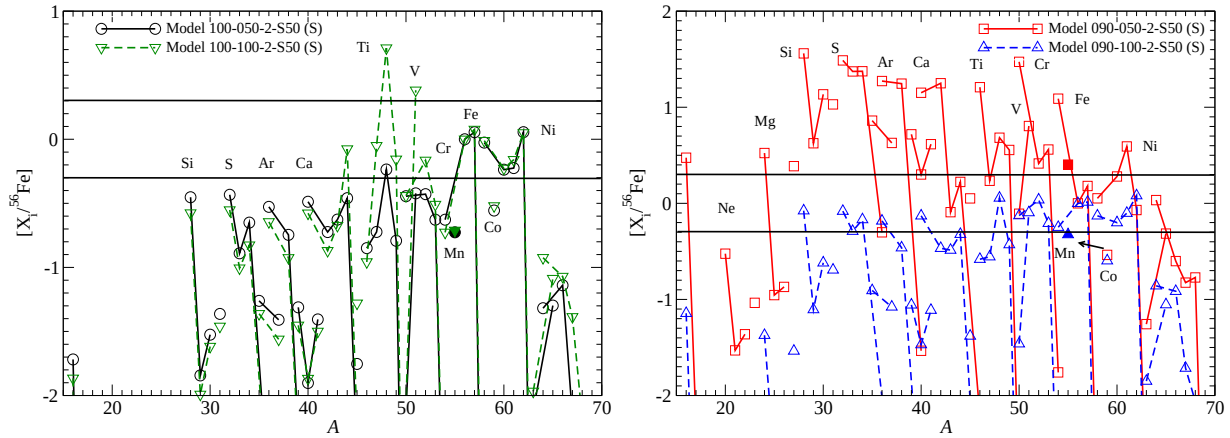

Figure 17. Similar to Fig. 15, but for Models 100-050-2-S50 (S) ($M = 1.00\ M_\odot$) and 110-050-2-S50 (S) ($M = 1.10\ M_\odot$) in the left panel and Models 100-100-2-S50 (S) ($M = 1.00\ M_\odot$) and 110-100-2-S50 (S) ($M = 1.10\ M_\odot$) in the right panel. All models assume $M_{\rm He} = 0.05$ (0.10) $M_\odot$ in the left (right) panel, $Z = 0.02$ and a spherical initial He-detonation at 50 km above the CO-envelope interface.

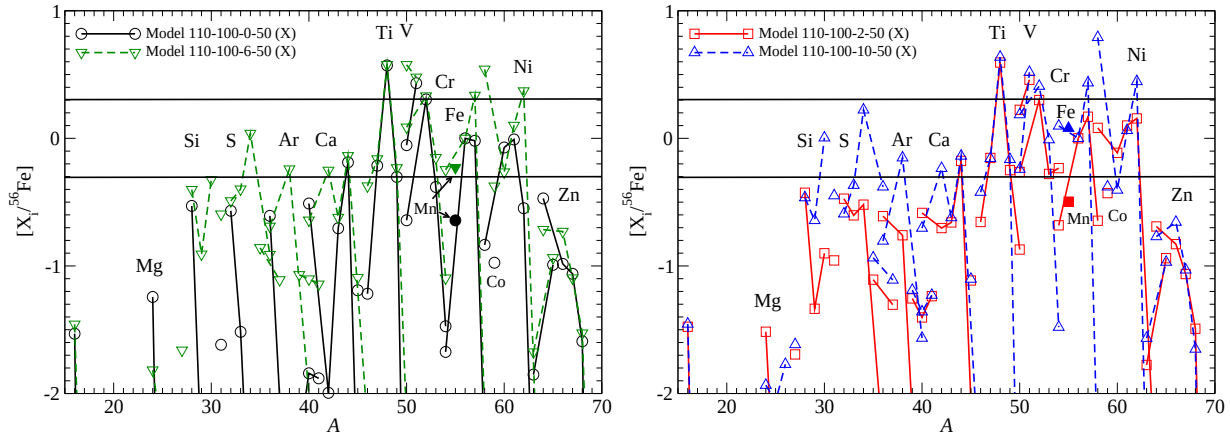

Figure 18. Similar to Fig. 12, but for Models 110-100-0-50 (X) ($Z = 0$) and 110-100-6-50 (X) ($Z = 0.06$) in the left panel and Models 110-100-2-50 (X) ($Z = 0.02$) and 110-100-10-50 (X) ($Z = 0.10$) in the right panel. All models assume $M = 1.10\ M_\odot$, $M_{\rm He} = 0.10\ M_\odot$, and a bubble shape initial He-detonation at 50 km above the CO-envelope interface.

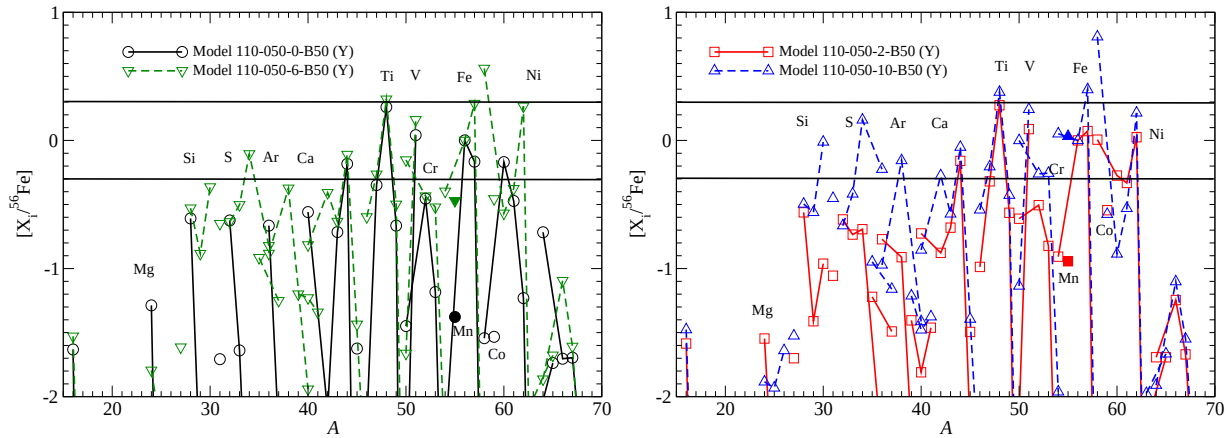

Figure 19. Similar to Fig. 18, but for Models 110-050-0-B50 (Y) ($Z = 0$) and 110-050-6-B50 (Y) ($Z = 0.06$) in the left panel and Models 110-050-2-B50 (Y) ($Z = 0.02$) and 110-050-10-B50 (Y) ($Z = 0.10$) in the right panel. All models assume $M = 1.10\ M_\odot$, $M_{\rm He} = 0.05\ M_\odot$, and a belt shape initial He-detonation at 50 km above the CO-envelope interface.

mass $M = 1.1\ M_\odot$, He mass at 0.05 $M_\odot$ and with the same He detonation trigger.

The general trends of isotopes on metallicity are similar to the one-bubble case. There is no significant change for the α-chain isotopes such as ^{28}Si, ^{32}S, ^{36}Ar and ^{44}Ca. But the slightly low-Y_e isotopes, such as ^{30}Si and ^{34}S, are strongly enhanced at high metallicity. There are smaller changes for the Fe-peak elements except for ^{52}Cr, ^{54}Fe, ^{55}Mn and ^{58}Ni. Minor increases can be observed for isotopes like ^{48}Ti and ^{51}V.

6.3.3. *Spherical Configuration*

In Figure 20 we plot similar to Figure 18 but for Models 110-050-0-S50 (S), 110-050-2-S50 (S), 110-050-6-S50 (S) and 110-050-10-S50 (S). Again, the models here share the same initial progenitor mass at 1.10 $M_\odot$, He mass at 0.05 $M_\odot$ and an initial spherical He detonation. The overall pattern remains compatible with the single one-bubble case.

The metallicity plays an important role to the slightly low-Y_e isotopes (defined by the neutron number N comparable but not larger than atomic number Z) including ^{30}Si, ^{34}S, ^{38}S, ^{42}Ca for the IMEs, and ^{51}V, ^{52}Cr, ^{55}Mn, ^{54}Fe and ^{58}Ni for Fe-peak isotopes. The variations of isotopes against metallicity are similar to the previous two cases. This shows that the metallicity dependence is not sensitive to the explosion energetics.

6.4. *Dependence on He Detonation Pattern*

Here, we analyze the final chemical abundance for different types of detonations. In Figure 21 we plot $[X_i/^{56}\mathrm{Fe}]$ for Models 110-100-2-50 (X) and 110-100-2-B50 (Y), 110-100-2-2R50 (D) and 110-100-2-S50 (S). They represent the typical detonation of Type "D", "X", "Y" and "S" respectively. All of the four models have ^{56}Ni closest to 0.6 $M_\odot$ among all models we have. We observe that in general "S"-Type is the strongest that it has more isotopes with abundances closer to solar values. "X"- and "Y"-Type are the intermediate ones and "D"-Type is the weakest among the four models. The difference for IME can be as large as a factor of $\sim O(1)$. For Fe-peak elements, differences can be found to Ti to Cr. The "Y"-Type model tends to produce less $^{47-50}$Ti, $^{50-51}$V, and $^{64-70}$Zn. The major difference between "Y"-Type and other detonation types is that there is no shock-convergence induced heating along the r-axis. This shows that ^{48}Ti is a sensitive indicator on how the He detonation propagates along the surface of the WD. Similar to previous cases, Fe and Ni are less sensitive to the detonation mechanism owing to the difference in production site.

6.5. *Differences from spherical detonation*

One theoretical uncertainty in the He detonation is that it is unclear whether the pre-explosion fluid motion is strong enough to alter the first detonation site. In the case with a strong fluid motion background, heat generated can be distributed by the eddy motion or be further enhanced by the local turbulent motion. This breaks the initial symmetry and creates some detonation bubbles. On the other hand, in the quiescent star, the whole He layer can simultaneously burn and reach the explosive temperature together. Thus, the initial detonation can preserve the symmetry. To derive constraints on the initial detonation profile, we examine the scaled mass fraction again in Figure 22 for both spherical and aspherical detonation model. Both models produce a very similar distribution for Fe and Ni since they are chosen to produce $\sim 0.6\ M_\odot$. For lighter Fe-peak elements, differences appear. The aspherical model produces more Ti, V and Cr than the spherical one for at least one order of magnitude. In particular, the ^{48}Ti, $^{50-51}$V and ^{52}Cr are $\sim$ 2 - 5 times higher than solar values. This suggests that observations of non-aspherical detonation model can be characterized by the excess of these light Fe-peak elements.

In Figure 23 we plot the $\rho_{\max}$ against $T_{\max}$ for the tracer particles of the two models. It can be seen that even for the same ^{4}He mass and total mass, the spherical model, whose evolution contains no oblique shock and the detonation wave propagates radially outward only, provides a uniform element distribution. This can be contrasted with the aspherical model, where the scattering in density and temperature is much pronounced.

6.6. *Constraints on progenitor model*

The double detonation model is one of the well accepted physical models due to the robustness of initiating the detonation and its variability in producing the dispersion in the observed SNe Ia brightness. However, one major concern, in contrast to the near-Chandrasekhar mass white dwarf, is that the detonation nature can produce a considerable amount of ^{56}Ni if the detonation is triggered too early, which produces overluminous SNe Ia. This is incompatible to the majority of SNe Ia, where $\sim$ 0.5 - 0.7 $M_\odot$ of ^{56}Ni is observed as induced by their light curves. In view of that it becomes important to understand, at which condition we could obtain realizations which can resemble with the typical SNe. This may provide constraints on the progenitor model, including the typical mass, the He envelope mass, and the initial detonation seed. In particular the position of the initial detonation seed is not yet well constrained.

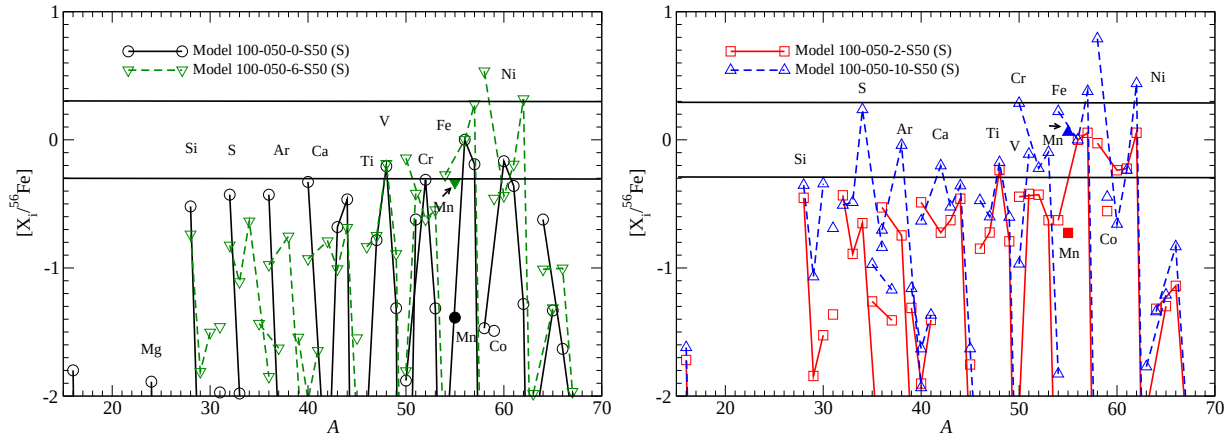

Figure 20. Similar to Fig. 18, but for Models 110-050-0-S50 (S) ($Z = 0$) and 110-050-6-S50 (S) ($Z = 0.06$) in the left panel and Models 110-050-2-S50 (S) ($Z = 0.02$) and 110-050-10-S50 (S) ($Z = 0.10$) in the right panel. All models assume $M = 1.10\ M_\odot$, $M_{\rm He} = 0.05\ M_\odot$, and a spherical initial He-detonation at 50 km above the CO-envelope interface.

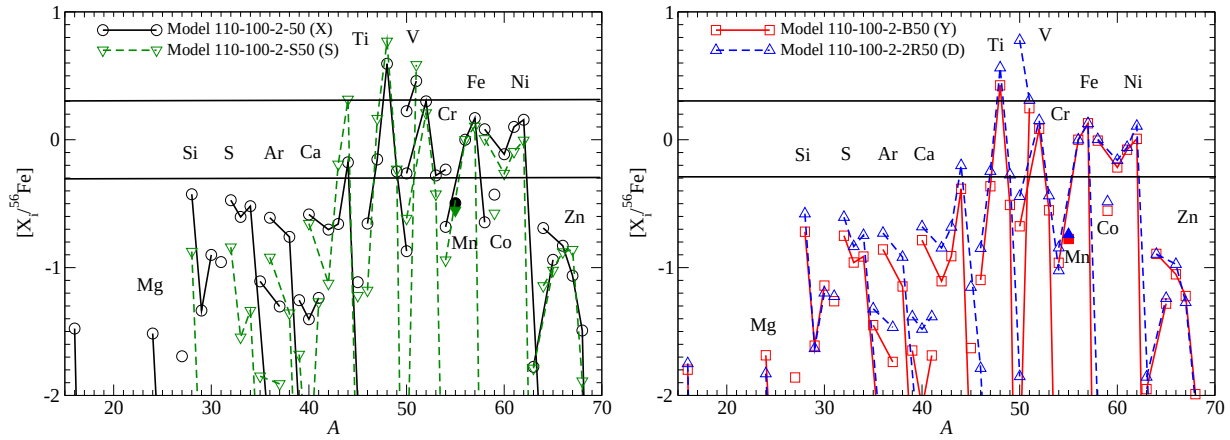

Figure 21. $[X_i/^{56}{\rm Fe}]$ for the series of models studying the effects of initial He detonation structure. Similar to Fig. 12, but for Models 110-100-2-50 (X) (bubble shape) and 110-100-2-B50 (Y) (belt shape) in the left panel and Models 110-100-2-2R50 (D) (bubble+belt shapes) and 110-100-2-S50 (S) (spherical) in the right panel. All models assume $M = 1.10\ M_\odot$, $M_{\rm He} = 0.10\ M_\odot$, and $Z = 0.02$.

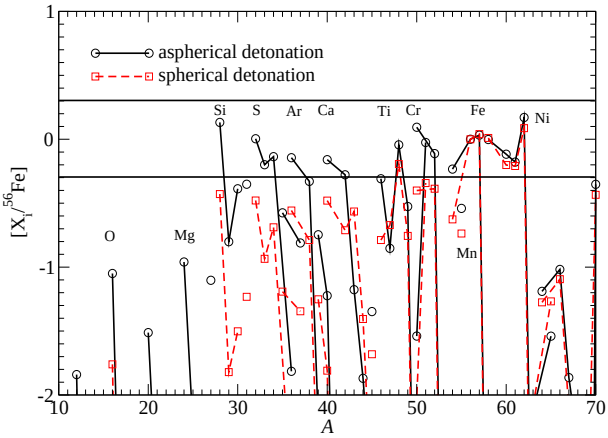

Figure 22. $[X_i/^{56}{\rm Fe}]$ for the two models 105-050-2-S50 (S) and 110-100-2-50 (X).

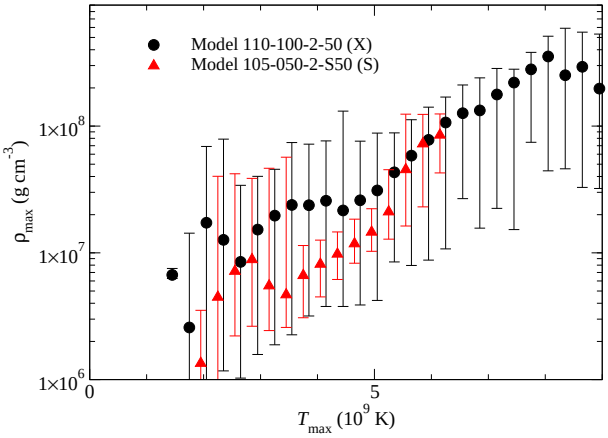

Figure 23. Similar to Figure 22, but for $\rho_{\rm max}$ against $T_{\rm max}$.

To do so, we plot the ^{56}Ni mass against progenitor WD mass for different progenitor masses and different explo-

sion mechanisms. In Figure 24 we plot that for the double detonation models for both the spherical detonation and the aspherical one, which we choose the one bubble pattern along the z-axis. For the near-Chandrasekhar mass WD, we use the standard DDT model with turbulent deflagration as reported in Leung & Nomoto (2017).

The sub-Chandrasekhar mass WD model corresponds to both single and double degenerate scenarios. We remind that for the violent merger model, due to the compactness of CO core, the secondary WD is disintegrated when the He detonation starts. Thus effectively it has a structure similar to the double detonation model in the single degenerate scenario. The Chandrasekhar mass model corresponds to the near-Chandrasekhar mass models presented in Leung & Nomoto (2017); Nomoto & Leung (2017). In particular, we choose the configuration identical to the benchmark model but for different central density from 5×10^8 to 5×10^9 g cm^{-3}.

In the sub-Chandrasekhar mass models (0.9 – 1.2 $M_\odot$), $M_{\rm Ni}$ increases with M for both spherical (Model 100-050-2-S50) and aspherical (Model 110-050-2-B50) models. This is because in principle the whole star is burnt. How complete the nuclear burning depends only on the density. For a lower mass WD, there is less matter with sufficient density to reach complete burning (typically 5×10^7 g cm^{-3}). Therefore, the ^{56}Ni scales almost linearly with M. On the other hand, in the Chandrasekhar mass branch, $M_{\rm Ni}$ decreases with M. This is related to the more efficient electron capture in the matter burnt by deflagration, which lowers the matter electron fraction. As ^{56}Ni is produced in NSE while ^{56}Ni has an electron fraction 0.5, any electron capture in the matter will only suppress the production of ^{56}Ni.

We note that we compute both Chandrasekhar and sub-Chandrasekhar mass models from both scenarios for a mass 1.2 – 1.3 $M_\odot$. This is because in this intermediate regime, it is unclear whether the thermonuclear runaway occurs in the form of deflagration or detonation, because the pressure jump becomes close to the initial pressure (Nomoto et al. 1976; Nomoto 1982b; Nomoto et al. 1984). Therefore, both scenarios cannot be ruled out. By examining the overlapping mass range for all three curves, it can be seen that the sub-Chandrasekhar mass branch has a $M_{\rm Ni}$ lower than the Chandrasekhar mass branch. Future statistics of observed SNe Ia for this pair of quantities will resolve the uncertainty here.

At last we explain the difference of $M_{^{56}\rm Ni}$ between the spherical and aspherical models. The spherical model in general produces more ^{56}Ni than the aspherical model for the same M. This is because the C-detonation starts in the center for the spherical model and off-center for the aspherical one. However, most the ^{56}Ni is produced near the center, where the density is the highest. This means, for aspherical detonation to produce ^{56}Ni, it needs to overcome the density gradient and the outward motion of the white dwarf during expansion. This requires more time for the detonation to reach the center to burn the matter for synthesizing ^{56}Ni, while the white dwarf has started its expansion. As a result, the matter density burnt by aspherical detonation in general is lower, which suppresses the production of ^{56}Ni. Future observations of SN Ia mass and ^{56}Ni mass can provide further constraints on this degeneracy, and hence the asphericity of the initial He-detonation.

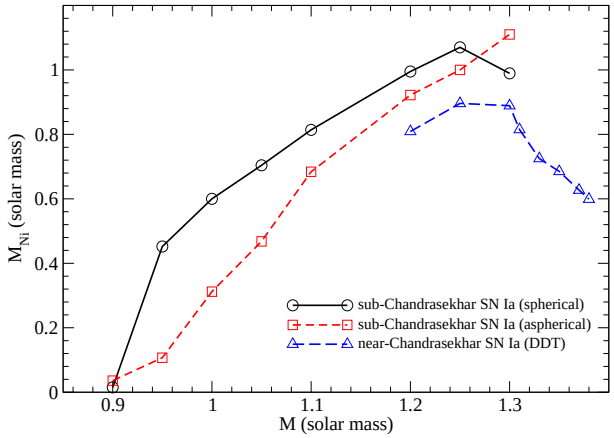

Figure 24. The synthesized ^{56}Ni mass at the end of the simulations against the initial WD mass. Both Chandrasekhar and sub-Chandrasekhar mass models are included. For sub-Chandrasekhar mass models, we use Models C-050-2-50 for aspherical model and Models C-050-2-B50 for spherical model, where C is the initial mass shown in the figure. The results for sub-Chandrasekhar mass and Chandrasekhar mass WD are selected from this work and in Leung & Nomoto (2017).

6.7. *Contribution to Galactic Chemical Evolution*

The single-degenerate (Chandrasekhar mass model) versus double degenerate (sub-Chandrassekhar mass model) scenario has been a long lasting theoretical tension remaining unsolved. The Chandrasekhar mass model has been favored because of its correspondence to an invariant model which can explain the similarity among observed SNe Ia. However, the shock-companion star interaction is shown to provide strong X-ray signal before the bolometric maximum of the light curves (Kasen 2010). The absence or non-discovery of such feature leads to the consideration of using the sub-Chandrasekhar mass model as an alternative to explain the origin of SNe Ia.

To compare how the sub-Chandrasekhar mass model influences the metal enrichment process we first compare the chemical yield directly. In Figure 25 we compare

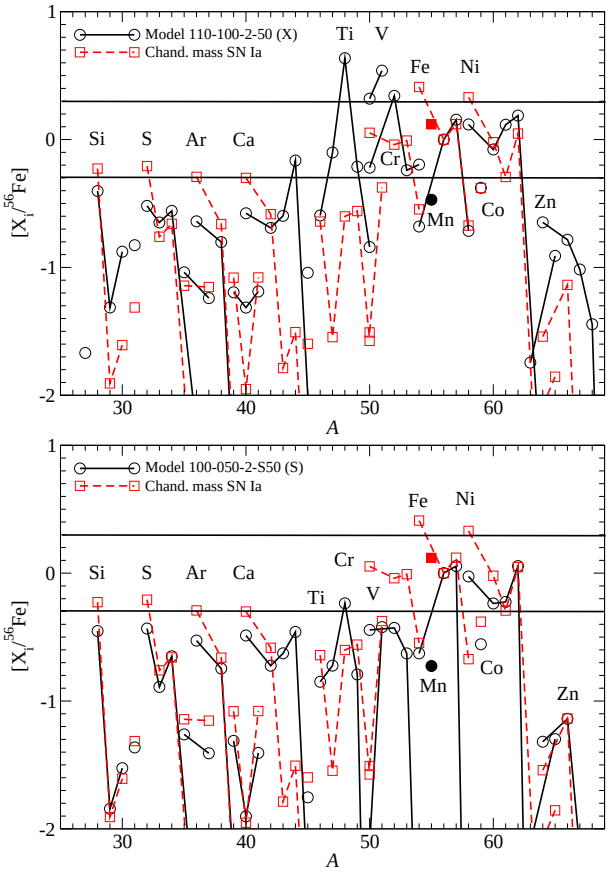

Figure 25. $[X_i/^{56}\mathrm{Fe}]$ for the benchmark Model 110-100-2-50 (X) (upper panel) and 100-050-2-S50 (S) (lower panel).

the chemical yield between the benchmark Models of this work, namely Model 110-100-2-50 (upper panel) and Model 100-050-2-S50 (lower panel) with the benchmark Chandrasekhar mass model. We can see that the Chandrasekhar mass model has its IME more closer to the solar value. The Ti and V productions are suppressed compared to the sub-Chandrasekhar mass model. The Fe and Ni patterns are similar for the two classes of model, except the ^{54}Fe and ^{58}Ni are more enhanced in the Chandrasekhar mass model. As remarked, the amount of Mn in the sub-Chandrasekhar mass model is very small to explain the solar value owing to the differences in electron capture rates. In Model 100-050-2-S50, a similar difference can be observed, except that the over-productions in Ti, V and Cr become regulated due to its less massive He envelope.

In Figure 26 we plot the evolution of $X(^{55}\mathrm{Mn})/X(^{56}\mathrm{Fe})$, scaled with the solar value, as a function of metallicity Z. To contrast with the results of the sub-Chandrasekhar mass model, we also include the benchmark Chandrasekhar mass model from Leung & Nomoto (2017); Nomoto & Leung (2017). The stellar abundance from galactic disk F and G dwarfs (Reddy et al. 2003), cluster

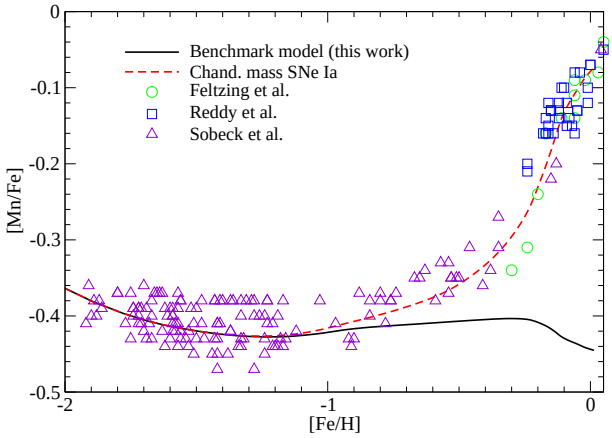

Figure 26. The $[^{55}\mathrm{Mn}/X(^{56}\mathrm{Fe})]$ against [Fe/H] for the benchmark model 110-100-2-50 (X) and the typical Chandarsekhar mass SNe Ia (Leung & Nomoto 2018).

and field stars (Sobeck et al. 2006) and stars from thin discs (Feltzing et al. 2007). are included. As expected, at $Z < -1$ both models do not alter the results since the time-delay of SNe Ia mutes the contribution of SNe Ia. After that, the two models deviate. The Chandrasekhar mass model, which shows a healthy electron capture, provides sufficient ^{55}Mn to raise the ratio close to the solar value. On the other hand, the sub-Chandrasekhar mass model, which produces only 30 % of the solar ratio. The prolonged underproduction of ^{55}Mn makes the ratio even decreases in [Fe/H]$= -0.2 - 0$ to $\approx 30\%$ of the solar value.

This suggests that even when sub-Chandrasekhar model can provide a variety of model, with ranges of ^{56}Ni to match observational results of different peak luminosity and with ranges of progenitor mass for different light curve widths. The Chandrasekhar mass model contribution to the stellar evolution remains important. The nucleosynthesis suggests that ^{55}Mn can be partially produced owing to the strong compression heating of the matter inside the star. The related mass is far from enough to explain the grow of ^{55}Mn especially from $\log_{10} Z = -0.2 - 0$.

For further application of our sub-Chandrasekhar SNe Ia yield in the context of GCE, we also present in Tables 16, 17 and 18, Tables 19, 20 and 21, and Tables 22, 23 and 24, the mass abundance of our representative SNe Ia models with the minimum M_{He} necessary for triggering the second detonation based on the Models 110-100-2-50 (X), 110-050-2-50 (Y) and 100-050-2-S50 (S) respectively. Metallicity is obviously an important factor which contributes to ^{56}Ni production and also the production of high neutron-ratio isotopes. M_{He} determines the minimum mass above which the C detonation can be triggered in our aspherical detonation models.

$M_{\rm Ni}$ is the primary indicator of the explosion strength as derived from the light curves.

It can be seen that, from the observational point of view, the sub-Chandrasekhar mass SNe Ia produce radioactive isotopes qualitatively different from the conventional Chandrasekhar mass SNe Ia. Due to the He envelope burning, α-chain elements are more pronounced. Among that, ^{44}Ti is produced, which has a half life of ≈ 60 years by electron capture to form ^{44}Sc. A typical amount of $\sim 10^{-3} M_\odot$ is found. Their abundance decreases when the ^{56}Ni production increases. The detection of the decay of ^{44}Ti as a long term energy of SNe Ia remnant may give very stringent constraints on the progenitor type of SNe Ia.

7. COMPARISONS WITH OBSERVED SUPERNOVAE AND SUPERNOVA REMNANTS

We have shown in Leung & Nomoto (2017); Nomoto & Leung (2017); Leung & Nomoto (2018) that the Chandrasekhar mass turbulent deflagration model with delayed detonation transition can be constrained through the observational data including the late-time light curves and the spectra. The late-time light curves can give indications to the amount of minor isotopes which has a longer lifetime compared to ^{56}Ni with a half life 7.8 days. They include for example ^{56}Co and ^{57}Co, which have a decay lifetimes of 77.2 and 272 days respectively. The energy deposition during the decay supports the light curve being observed. Another way to study SN chemical abundance is by the spectra of SN remnant. Through a comparison of the X-ray line strengths of the radioactive elements, such as Cr, Mn, Fe and Ni, one can obtain the ratio among these elements and thus cast constraints on the explosion mechanism (See. e.g. Yamaguchi et al. (2014)).

7.1. *Supernova Remnant 3C 397*

The first example we study is the SN remnant 3C 397 (Yamaguchi et al. 2015). This SN remnant has a remarkable X-ray spectrum in terms of its rich neutronized material compared to other SN remnants such as Tycho and Kepler. This remnant is also shown that the Chandrasekhar mass model is one of the feasible realizations of SN Ia explosions constrained by direct observational data. In the measurement, this remnant is found to have $0.027\pm^{+0.007}_{-0.006} M_\odot$ Cr, $0.025\pm^{+0.008}_{-0.007} M_\odot$ Mn and $0.17\pm^{+0.07}_{-0.05}$ Ni. This corresponds to the Mn/Fe and Ni/Fe ratios being 0.018 - 0.033 and 0.11 - 0.24 respectively. In Yamaguchi et al. (2015) it is shown that by using one-dimensional models, Chandrasekhar mass model ($M \approx 1.37\ M_\odot$) with a metallicity five times to the solar metallicity is shown to produce the closet abundance ratio. In Nomoto & Leung (2017); Leung & Nomoto (2018) we reported similar discovery based on a series of two-dimensional models of turbulent deflagration model with delayed detonation transition. Here we shall examine our models to see in the sub-Chandrasekhar mass domain what kind of model is needed to explain this SN remnant.

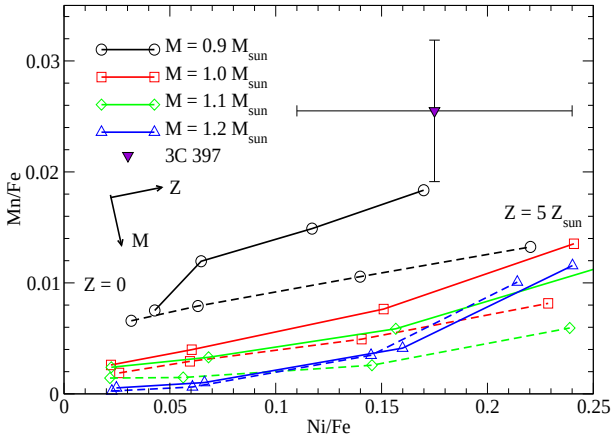

Figure 27. The mass ratio Mn/Fe against Ni/Fe for the sub-Chandrasekhar mass models from $M = 0.9$, 1.0, 1.1 and 1.2 $M_\odot$. The He envelope is fixed to be 0.1 (solid line) and 0.2 (dashed line) $M_\odot$. The metallicity ranges from 0, 1, 3 and 5 $Z_\odot$ for models on the same line from the left to right. The observational data point of the SN remnant 3C 397 is included. The typical mass and metallicity dependences of the models are shown by the arrows.

In Figure 27 we plot Mn/Fe against Ni/Fe for our sub-Chandrasekhar mass models with the observational data from the SN remnant. The SN Ia models of $M = 0.9$ - 1.2 $M_\odot$ are included with a He envelope of $M_{\rm He} = 0.1 - 0.2\ M_\odot$. We pick $Z = 0$ to 5 $Z_\odot$ as done in Leung & Nomoto (2018). It can be seen that in general when metallicity increases, Mn/Fe increases with Ni/Fe. However, when the total mass M increases, the whole shifted downward, showing that the Mn/Fe ratio drops but no significant change in Ni/Fe observed. This is because when the mass increases, the central density of the initial model increases, therefore, the C detonation becomes more energetic which can unbind the star more quickly. As a result, more ^{56}Ni is produced which suppresses the ratio.

The model with a more massive He envelope has a lower [Mn/Fe] in general because of the higher ^{56}Ni as part of it can be produced in the envelope. This relation is uniform for almost all models except for $Z = 5$ $Z_\odot$ at $M = 1.2\ M_\odot$. The two models show a rapid jump in the [Mn/Fe] ratio. This is because at high density, electron density becomes important. The C detonation, which can release adequate energy to burn the

core matter into NSE, is followed by electron capture before the matter cooling down by adiabatic expansion. Certainly, the typical electron capture rate in the sub-Chandrasekhar mass model is considerably lower than those in typical Chandrasekhar mass models. The lowered electron fraction in the core matter, when in NSE, will be more favourable to produce ^{55}Mn, which has a proton ratio of 0.454. The data point of 3C 397 is included. It can be seen that the data point lies very far from the other lines. This is consistent with the conclusion in Yamaguchi et al. (2015) that the single degenerate Chandrasekhar mass SN Ia channel is more likely to explain this peculiar SN Ia.

Our models show that the ^{55}Mn production is in general too low that even with a rather small ^{56}Ni production at the end of simulation, the resultant [Mn/Fe] ratio remains insufficient to explain. The closest model is the $M = 0.9\ M_\odot$ at $Z = 5\ Z_\odot$. Our result is comparable with theirs.

One may note that this object has raised interest in the literature owing to its predicted high metallicity and different proposals are raised in order to recover the high [Mn/Fe] ratio without invoking the high metallicity. For example, in Shen et al. (2018) the sub-Chandrasekhar mass SNe Ia in the spherical approximation is revisited. The high [Mn/Fe] is shown to be viable if one consider a subset of ejecta, namely by taking the effects of reverse shock heating into account. Another attempt is done in Dave et al. (2017). The gravitational confined detonation model is explored with extension to pure turbulent deflagration with or without delayed detonation transition for the Chandrasekhar mass model. It is shown that a combination of high central density, low [C/O] ratio and a high offset of initial deflagration can provide an alternative to this observation. These trends are consistent with our previous finding as reported in Leung & Nomoto (2018).

7.2. *SN 2012cg*

The next application is on SN 2012cg. This SN exploded at 2012 May 17 (UT) in the nearby spiral galaxy NGC 4424, which is measured in the Lick Observatory Supernova Search Kandrashoff et al. (2012). The SN Ia nature is revealed in the spectral study found in Cenko et al. (2012); Marion et al. (2012). This SN Ia is close enough that the late-time light curve after $\sim$ 1000 days can still be measured. The low-density ejecta becomes transparent to most γ-ray so that the γ-ray emitted during decay can escape freely from the ejecta without significant heating. On the other hand, the emitted e^- is completely absorbed by the surrounding matter. This means that one can trace its amount

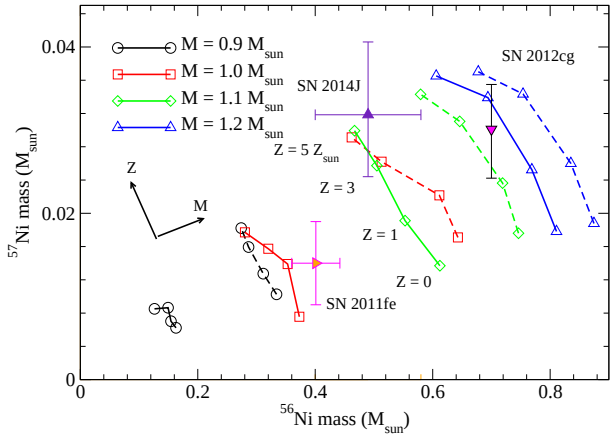

Figure 28. ^{57}Ni against ^{56}Ni for our sub-Chandrasekhar mass models from $M = 0.9$, 1.0, 1.1 and 1.2 $M_\odot$. The He envelope is fixed to be 0.1 (solid line) and 0.2 (dashed line) $M_\odot$. The metallicity ranges from 0, 1, 3 and 5 $Z_\odot$ for model from bottom to top. The observational data point of the SN 2011fe, SN 2012cg and SN 2014J are included. The typical mass and metallicity dependences of the models are shown by the arrows.

through its decay as a heat source in the light curve. In particular, the channels ^{56}Co $\rightarrow^{56}$Ni (half life $\approx$ 113 days) and ^{57}Ni $\rightarrow^{57}$ Co (half life $\approx$ 272 days) can be readily measured. In Graur et al. (2016), the B-band light curve of SN 2012cg is revisited at 900 days after the B-band maximum. It is shown that this SN Ia has a high ^{57}Ni/^{56}Ni ratio at $0.043\pm^{+0.012}_{-0.011}$, which is twice to the corresponding solar ratio.

In Figure 28 we plot similar to Figure 27 but for ^{57}Ni against ^{56}Ni for the same series of models and with this SN Ia. For models with an increasing metallcity, ^{57}Ni production increases while ^{56}Ni mildly decreases. This is because the initial electron fraction, as metallicity increases, deviates from the value 0.5, which most favours the production of ^{56}Ni in NSE. On the other hand, the lowered electron fraction enhances production of ^{57}Ni. Models with a thicker He envelope has higher ^{56}Ni and ^{57}Ni compared to models with the same mass but lower $M_{\rm He}$. Similarly, for models with an increasing M, the ^{56}Ni and ^{57}Ni productions are enhanced as a result of higher central density, which allow more matter to be burnt until NSE for producing Fe-peak elements.

Then, we compare our results with this SN Ia. The data point of SN 2012cg is included. It can be seen that this SN has a rather high $^{56-57}$Ni as a healthy explosion. In our models, the high mass models $M = 1.2\ M_\odot$ with high metallicity from $3-5\ Z_\odot$ are more likely to explain this data point. This is consistent with our previous work (Leung & Nomoto 2017; Nomoto & Leung 2017; Leung & Nomoto 2018) that a high metallcity model

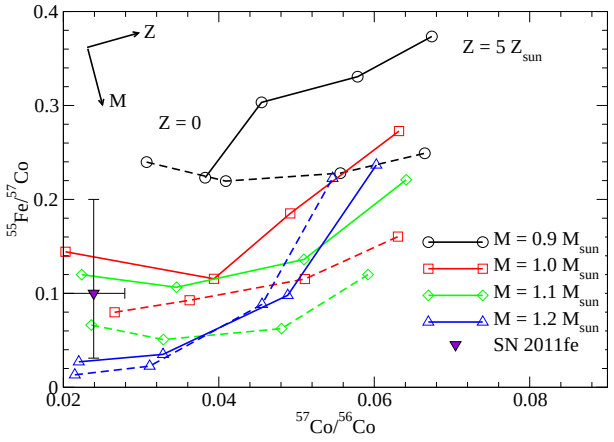

Figure 29. ^{55}Ni/^{57}Co against ^{57}Ni/^{56}Co for our sub-Chandrasekhar mass models from M = 0.9, 1.0, 1.1 and 1.2 $M_\odot$. The He envelope is fixed to be 0.1 (solid line) or 0.2 (dashed line) $M_\odot$. The metallicity includes 0, 1, 3 and 5 $Z_\odot$. The observational data point of the SN 2011fe is included. The typical mass and metallicity dependences of the models are shown by the arrows.

from $1-5$ $Z_\odot$ with a central density from 5×10^8 - 1×10^9 g cm^{-3} may fit this observational data the best. However, compared to our Chandrasekhar mass model, the sub-Chandrasekhar mass models can fit the upper range of this data point by models with M = 1.2 $M_\odot, M_{\rm He} = 0.1 M_\odot$ and fit the lower range of that by models with M = 1.1 $M_\odot, M_{\rm He} = 0.2 M_\odot$). The trend derived here agress with the estimation from the analytic formula as done in Graur et al. (2016) that the Chandrasekhar mass model is more preferred for this high ^{57}Ni abundance. However, we also emphasized that the sub-Chandrasekhar mass model is not excluded by this SN Ia as a physical picture. To further clarify its origin, future spectral study in the remnant, similar to the SNR 3C 397 will be necessary.

7.3. *SN 2011fe*

The third example comes from the well observed SN 2011fe. This recent SN exploded at 2011 August 24 in a rather proximate Pinwheel galaxy (Nugent et al. 2011), which situated at 6.4 Mpc away (Shappee & Stanek 2011). The close distance of this SN Ia has attracted intensive study in different bandwidths (See Shappee et al. (2017) for the references therein) and spectral studies. This also allows detection of light curves beyond $\sim$ 1000 days. This provides more abundance constraints compared to the previous SN 2012cg. This SN Ia is first probed with the decay of ^{55}Fe (^{55}Fe $\rightarrow^{55}$Mn with a half life of 999.67 days) directly. Through taking ratios with other decaying channels, they observe $\log_{10}(^{57}{\rm Co}/^{56}{\rm Co}) = -1.62\pm^{+0.08}_{-0.09}$. In their best fit model they also showed $\log_{10}(^{55}{\rm Fe}/^{57}{\rm Co}) = -1.0\pm^{+0.3}_{-0.5}$.

In Figure 29 we plot similar to Figure 28 but for the ratio ^{55}Fe/^{57}Co against ^{57}Co/^{56}Ni for our sub-Chandrasekhar mass models and the observational data SN 2011fe. Our models show a less uniform variation with increasing metallicity in the sub-Chandrasekhar mass range. The variation is non-uniform at low metallicity (0 - 1 Z). On the other hand, ^{55}Fe/^{57}Co increases with metallicity, showing that the abundance of ^{55}Fe is more sensitive to metallicity. This is expected, as shown in Figure 27 that the metallicity still plays an important role in the formation of stable Mn, which comes from the decay of ^{55}Fe. The models tend to have a lower ratio when the He envelope becomes thicker. Also, when the total mass increases, the ratio is also suppressed. This is because the growth of ^{57}Ni, which is very sensitive to the size of zone being burnt into NSE, is faster than ^{55}Fe. The much faster growth of ^{55}Fe/^{57}Co for the model M = 1.2 $M_\odot$ and Z = 5 $Z_\odot$ is again related to the enhancement of electron capture in the NSE region. The observational data point fits our model much better than the previous two models. It can be seen that a wide range of parameters can be used to explain this SN Ia. SN Ia models from $M = 1.0-1.2$ $M_\odot$ and a low metallicity $Z = 0-1$ $Z_\odot$ are adequate to fit in this observational data. This is also consistent with our previous work (Leung & Nomoto 2017; Nomoto & Leung 2017; Leung & Nomoto 2018) that a low central density from $5\times10^8-7.5\times10^8$ g cm^{-3} with a metallicity $0-1$ $Z_\odot$ can explain this data point using the turbulent deflagration model with DDT.

Recent late time study of the light curve in the optical band has also revealed the ^{57}Ni/^{56}Ni ratio of this SN Ia. By measuring the shift of late time light curve after most ^{56}Ni has decayed, the decay of ^{57}Ni $\rightarrow^{57}$Co can be another important radioactive source. In Dimitriadis et al. (2017), the pseudo-bolometric light curve is produced by combining data of the optical and near-IR bandwidth in the literature from 200 to 1600 days after explosion. It is shown that this supernova, albeit with significant systematic uncertainties, ^{57}Co/^{56}Co = 0.031 ± 0.011.

In Figure 28 we also plot this data point with our model sequences. The prediction of WD progenitor using the explosion product has been discussed for SN 2012cg in the previous section. Here we further apply this technique for SN 2011fe. The WD sequence with a mass $\approx$ 1.0 $M_\odot$ with a He envelope $\approx$ 0.1 $M_\odot$ can explain the observed ^{57}Ni/^{56}Ni ratio. The data point can be the best explained by the model with $\sim Z_\odot$.

We remark that, from the first sight the SN 2011fe is very well explained by the sub-Chandrasekhar mass model, in fact, in Leung & Nomoto (2017); Nomoto & Leung (2017) we demonstrate that this SN

Ia can also be explained by the Chandrasekhar mass model in the high central density (high mass) limit with a metallicity close to $Z_\odot$ in the centrally ignited model. This suggests that to further constrain the progenitor, future follow-up observations will be essential to measure the abundances of other isotopes or elements, similar to the analysis done for the SNR 3C 397.

7.4. *SN 2014J*

The fourth application of our models to the SN Ia observation is the candidate SN 2014J. This is an extremely well observed SN Ia owing to its vicinity. This SN Ia is observed from very early time since its rising light curve (Goobar et al. 2014). The multi-frequency light curve and spectra are observed ranging from the infrared spectra (Telesco et al. 2015), optical photometry and spectrography (Ashall et al. 2014), ultraviolet (Foley et al. 2014; Brown et al. 2015), to gamma-ray light curve and spectra (Diehl et al. 2015a; Churazov et al. 2015; Diehl et al. 2015b; Isern et al. 2016). This supernova is interesting for its peculiar gamma ray signals. It has an early gamma ray signal coming from the decay of ^{56}Ni at about 20 days after explosion, which is 10 days in advance of typical SNe Ia (Diehl et al. 2015a). The follow-up observation in its time-domain variations shows that it has a non-monotonic variation in the ^{56}Co-decay gamma ray line. The Doppler shift analysis further shows the highly fluctuating Co-decay line frequency (Diehl et al. 2015b). Such features are argued to be originated from the He detonation and asymmetry in the detonation. The current work on the asymmetry double detonation model appears to well match with this SN.

Here we try to constrain its progenitor from some of its observable by its ^{57}Ni/^{56}Ni mass fraction ratio. This ratio has been applied to other SNe Ia including the previous SN 2011fe and SN 2012cg. The late time flattening of the late curve in the optical band is analysed, from 277 days to 1181 days after explosion. From the analysis of the late time light curve (Yang et al. 2018), the mass ratio of ^{57}Co/^{56}Co $= 0.066 \pm^{0.009}_{0.008}$. The ratio is even higher than SN 2012cg. By using the ^{56}Ni derived from gamma ray (Isern et al. 2016), where $^{56}\mathrm{Ni} = 0.49 \pm 0.09$, we plot in Figure 28 the data point of SN 2014J.

From the figure we observe that the sub-Chandrasekhar mass model is capable of reaching the high Ni-isotope ratio at the high metallicity end. Two of the model sequences can approach this observed data point, namely when $M = 1.1\ M_\odot$ with $M_{\rm He} = 0.10\ M_\odot$ and $M = 1.0\ M_\odot$ with $M_{\rm He} = 0.20\ M_\odot$. Both sequences require $Z \approx 5\ Z_\odot$ to reach the high mass fraction ratio. Again, the more massive He envelope is capable of producing the required ^{56}Ni, however such early surface ^{56}Ni can be very different from that produced through standard Chandrasekhar mass WD. In the latter case, the ^{56}Ni is mostly produced by C detonation after deflagration-detonation transition. But it is always covered by another layer of IME when the detonation reaches the surface. As a result, the ^{56}Ni-decay is not directly visible, but can be seen as a heat source in the light curve. On the other hand, with the He envelope, there is almost no shielding for the synthesized ^{56}Ni, therefore it is expected that the early gamma-ray signal can be very different. We also note that such a massive He envelope with decaying 56Ni should show rather strong He lines.

We also compare the 57Ni/56Ni ratio of SN 2014J with the Chnadrasekhar mass models in Figure 20 of Leung & Nomoto (2018). We note that the Chandrasekhar mass models with $Z \approx 3-5\ Z_\odot$ produces the observed high 57Ni/56Ni ratio.

8. SUMMARY

In this paper, we study the hydrodynamics and associated nucleosynthesis of sub-Chandrasekhar mass models for SNe Ia, where the C detonation is triggered by the surface He detonation of a symmetric or an asymmetric structure. Such a double detonation can in both the single degenerate and the double degenerate scenarios. Our findings are summarized as follows.

(1) We find that whether C detonation triggered is strongly sensitive to the He detonation pattern. We consider four possible structures: namely, one-bubble, one-ring, bubble-and-ring, and spherical, in view of the unresolved, inner fluid motion of the He shell before nuclear runaway. The He detonation with higher symmetry (one-ring and spherical structures) can result in geometric convergence, which can very robustly heat up the C fuel to the ignition temperature for the subsequent temperature. He detonation with lower symmetry (one-bubble) requires a more massive He envelope ($> 0.1\ M_\odot$) to trigger the second explosions. The case with multi-bubbles depends on how the shock wave propagates inside the WD.

(2) We carry out a parameter survey on the nucleosynthesis for the sub-Chandrasekhar mass WD models with different model parameters. We perform two-dimensional hydrodynamical simulations using our own supernova simulation code from the onset of the He detonation until all detonations quench by the expansion. The following parameters are studied: the metallicity, He envelope mass, total mass, the initial He detonation, and the initial C/O mass fraction ratio. We pay attention to some representative elements, including intermediate mass elements (e.g. Si, S, Ar and Ca), light

iron-peak elements (Ti, V and Cr) and other iron-peak elements (Mn, Fe, Co, Ni). These elements are strongly sensitive to the total mass, metallicity and He-envelope mass, but less sensitive to the initial He detonation and C/O mass fraction ratio. Metallicity affects mostly on the low-Y_e isotopes e.g., ^{55}Mn and ^{58}Ni. He envelope mass affects light iron-peak elements, especially ^{48}Ti, ^{50,51}V and ^{52}Cr. Total mass affects ^{56}Ni and hence the mass fraction $[X_i/^{56}\mathrm{Fe}]$ with respect to the Sun.

(3) We also compare our two-dimensional models with the classical spherical double detonation model and show that the chemical signature due to asphericity is very significant. The aspherical detonation can create hot spots which produce distinctive abundance pattern in intermediate mass elements and light iron-peak elements (Ti, V and Cr). Explosion of progenitor with a mass $\sim 1.1-1.2\ M_\odot$ may help distinguish in the future the degeneracy of single and double degenerate scenario. However, an exact matching with the observed ^{56}Ni distribution will also require the stellar initial mass function. We further show that the sub-Chandrasekhar mass WD models cannot substitute the Chandrasekhar mass one because of the persistent insufficiencies of Mn production. The final [Mn/Fe] can be 0.4 dex lower than the model using Chandrasekhar mass WD model. We provide corresponding yield tables for the applications to the galactic chemical evolution.

(4) We apply our models to provide constraints on some well-observed SNe Ia, including SN 2012cg, SN 2011fe, SN 2014J, and SN Ia remnant 3C 397. The probable progenitor configurations are implied based on the derived chemical abundance of some Fe-peak isotopes. We used the late time light curve to indicate the ^{57}Ni/^{56}Ni ratio. We find that SN 2014J can resemble with the sub-Chandrasekhar mass model at $1.0-1.1\ M_\odot$ with metallicity $Z = 3-5\ Z_\odot$. (Note that the Chandrasekhar mass models also resemble to SN 2014J if $Z = 3-5\ Z_\odot$.) SN 2011fe can be explained by models with $M \sim 1.0 M_\odot$ with near Z_{odot}. SN 2012cg can be approached by models with $M = 1.1-1.2 M_\odot$ at $Z = 1-3\ Z_\odot$. For supernova remnant 3C 397, the high Mn/Ni ratio cannot be resembled with any of our current sub-Chandrasekhar mass models. The Mn/Fe ratios in our models are much lower than the observed value. Only models at the lower mass end ($0.9 M_\odot$) with $Z = 5 Z_\odot$ can approach the observe data point.

(5) The hydrodynamical structures and nucleosynthesis profiles provide useful predictions for future observations of elemental abundances and line γ-rays.

9. ACKNOWLEDGMENT

This work has been supported by World Premier International Research Center Initiative (WPI), and JSPS KAKENHI Grant Number JP17K05382. S.C.L. acknowledges support from Grant HST-AR-15021.001-A.

We thank the anonymous referee for the very detailed and helpful suggestions to improve the manuscript.

We thank Frank Timmes for his open-source microphysics subroutines including the Helmholtz equation of state and the *torch* subroutine for the post-process nucleosynthesis. We also thank Ken Shen for the ideas in the numerical modeling of the detonation physics. We thank Amanda Karakas and Chiaki Kobayashi for the information about the galactic stellar abundances. At last we thank Roland Diehl and Jordi Isern for the inspiring discussion about SN 2014J.

APPENDIX

A. DETERMINATION OF THE HE DETONATION TIMESCALE

In Section 2 we mentioned that simplified schemes for C and He detonation are used. In this section, we describe in more details how they are implemented. Unlike C detonation, He detonation in the sub-Chandrasekhar mass WD scenario, occurs at a much lower density ($\sim 10^4 - 10^7$ g cm^{-3} in the He envelope). The low density, as well as the non-degenerate property of the electron gas, lead to a lower final temperature, after all He is burnt. As a result, it becomes important to estimate more precisely how much He is burnt in the reaction zone and in the post-reaction zone. In particular, we are interested to know how He is burnt as a function of time, which is used to calibrate the amount of energy released by the detonation.

We calculate the detonation structure following the numerical scheme described in Sharpe (1999). Here we give a brief summary about this method. In general, detonation consists of three sections, the pre-shock region, the reaction zone and the post-reaction region. We assume at every point inside the detonation wave, thermodynamics equilibrium is maintained, such that the specific internal energy ϵ, pressure p are related by the thermodynamics input including the density ρ, temperature T and the number fraction of each isotope Y_i ($i = 1, N$) in a network with N isotopes. Therefore,

$$\Delta\epsilon = \frac{\partial\epsilon}{\partial\rho}|_{T,X_i} + \frac{\partial\epsilon}{\partial T}|_{\rho,Y_i} + \sum_i \frac{\partial\epsilon}{\partial Y_i}|_{\rho,T}. \tag{A1}$$

The steady state Euler equation can be written as

$$\frac{d\rho}{dx} = -\frac{\rho a_f^2}{v}\frac{\sigma \cdot \mathbf{R}}{\iota}, \tag{A2}$$

$$\frac{dT}{dx} = \left(\frac{\partial p}{\partial T}\right)^{-1}_{\rho,X} \{\left[u^2 - \left(\frac{\partial p}{\partial \rho}\right)_{T,X}\right]\frac{d\rho}{dx} - \sum_{i=1}^{N}\left(\frac{\partial p}{\partial X_i}\right)_{\rho,T,X_{j\neq i}}\frac{dX_i}{dx}\}, \tag{A3}$$

$$\frac{dX_i}{dx} = \frac{R_i}{A_i v}, \tag{A4}$$

where

$$\eta = a_f^2 - v^2 \tag{A5}$$

is the sonic parameter, A_i is the atomic mass for the i-th isotope,

$$a_f^2 = \left(\frac{\partial p}{\partial \rho}\right)_{T,X} + \left[\frac{p}{\rho^2} - \left(\frac{\partial \epsilon}{\partial \rho}\right)_{T,X}\right]\left(\frac{\partial p}{\partial T}\right)_{\rho,T}\left(\frac{\partial \epsilon}{\partial T}\right)^{-1}_{\rho,X} \tag{A6}$$

is the sound speed of constant composition (also known as frozen sound speed in the literature of detonation),

$$\sigma_i = \frac{1}{\rho a_f^2}\{\left(\frac{\partial p}{\partial X_i}\right)_{\rho,T,X_{j\neq i}} - \left(\frac{\partial p}{\partial T}\right)_{\rho,X}\left(\frac{\partial \epsilon}{\partial T}\right)^{-1}_{\rho,X}\left[\left(\frac{\partial \epsilon}{\partial X_i}\right)_{\rho,T,X_{j\neq,i}} - \left(\frac{\partial q}{\partial X_i}\right)_{X_{j\neq i}}\right]\} \tag{A7}$$

is the thermicity constant, such that $\sigma \cdot \mathbf{R}$ is the thermicity. In integrating this set of differential equations, we use the boundary conditions at $x = 0$, $\rho = \rho_i$, $T = T_i$; at $x \to \infty$, $\rho = \rho_f$, $T = T_f$ and $X = X_f$ with thermicity = 0. Notice that ρ_i, T_i and Y_i are the quantities after shock. They are related to the pre-shock quantities (ρ_0, T_0, X_0) by

$$\rho_0 D = \rho_i c_s, \tag{A8}$$

$$\rho_0 D^2 = \rho_i c_s^2, \tag{A9}$$

$$\rho_0 D^2 + \rho_0 \epsilon_0 + P_0 = \rho_i c_s^2 + \rho_i \epsilon_i + P_i. \tag{A10}$$

D, c_s and P_0 are the pre-shock matter density, speed of sound and pressure of the pre-shock matter.

In Figure 30, we plot the density, temperature and chemical isotope profiles for a detonation wave at a density 10^6 g cm^{-3}. To trigger the first incineration, the matter is assumed to be shock heated to a temperature $\sim 2 \times 10^9$ K. Before 10^{-4} s. the temperature does not rise considerately. Also, there is only very subtle drop in the density. There is also a slow change in the chemical composition from ^{4}He to ^{12}C. At $\sim 10^{-4}$ s, the temperature rises drastically from 2×10^9 K to 3×10^9 K. The density also drops by ~ 30 %. We can see a isotopes from ^{12}C, ^{40}Ca, ^{48}Ti and ^{52}Fe burst out one by one around 10^{-4} s. This means that even at low temperature, the α-chain reaction can proceed efficiently, once the triple α reactions have provided the first fuel for the subsequent reactions. Beyond 4×10^{-4} s, the productions of other isotopes are suppressed again, except ^{56}Ni. At that time, ^{4}He is stably burnt into ^{56}Ni, causing the temperature (density) to grow (drop) to its equilibrium value. At ~ 1 s, the temperature and density reaches its equilibrium at 3.6×10^9 K and 4.6×10^6 g cm^{-3}.

In Figure 31, we plot the temperature, density and isotope abundance profiles for pure He fuel at an initial density of 10^7 g cm^{-3}. With a high density, nuclear reactions can take place spontaneously. In the first 10^{-4} s, temperature increases quickly from 3×10^9 K to 6×10^9 K. while the density drops from 4×10^7 g cm^{-3} to $\sim 2 \times 10^7$ g cm^{-3}. The initial peaks for various isotopes except ^{56}Ni can be found at the first 10^{-6} s, while the conversion of ^{4}He to ^{56}Ni can be found at the first 10^{-4} s. After that, the temperature and density start to converge to their asymptotic values at $\sim 5.5 \times 10^9$ K and 1.4×10^7 g cm^{-3}. At the same time, the temperature is sufficiently high that NSE emerges. ^{52}Fe, ^{40}Ca, ^{48}Cr, ^{36}Ar, ^{32}S form one by one and reach their equilibrium value at ~ 0.1 s.

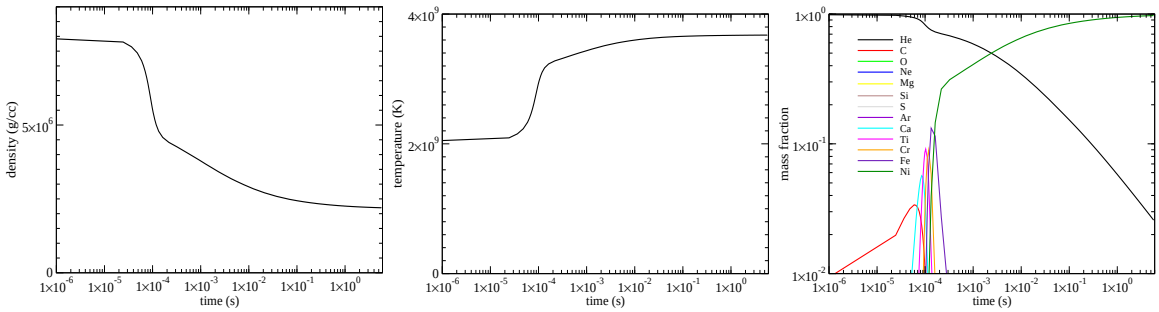

Figure 30. (left) The density evolution of He during detonation for pure He fuel at a density 10^6 g cm^{-3}. The matter is assumed to be shock-heated to above 2×10^9 K. (middle) The temperature evolution of the detonation wave at an initial density 10^6 g cm^{-3}. (right) The isotope evolution of the detonation wave at an initial density 10^6 g cm^{-3}

By comparing the two sets of results, we can see that in the density range related to the sub-Chandrasekhar mass double detonation models, the time necessary for He to completely release its energy into the system increases by two orders of magnitude when the density drops from 10^7 to 10^6 g cm^{-3}. (In the simulations we find the typical time steps has a size $\sim 10^{-4} - 10^{-3}$ s, depending on the global velocity distribution). Therefore, especially for the He near the surface, once they are burnt they expand drastically, making their local density much lower than those underneath. As a result, their energy release process is incomplete. To mimic this effect, we use a density dependent time scale $\tau_{\rm He}(\rho)$ which is calibrated by the detonation waves as demonstrated above. The time scale corresponds to the time when 90 % of energy is released with respect to its equilibrium value. To establish the relation $\tau_{\rm He}$, we repeat the above process for He-detonation wave at different initial densities. Then we collect the necessary time scale by the above detonation. A simple power-law fitting provides us the formula:

$$\tau_{\rm He} = 1.72 \times 10^{-6} \left(\frac{\rho}{10^8 \text{ g cm}^{-3}} \right)^{-2} \text{s}. \tag{A11}$$

In the simulations, when the current time step $\Delta t > \tau_{\rm He}$, complete burning is assumed. Otherwise, only the fraction of matter $\Delta t/\tau_{\rm He}$ is assumed to release its energy. We have only considered the effect of density because the reaction rate is very sensitive to the input temperature. Below the ignition temperature ($\sim 10^9$ K), the reactions are so slow that the burning time scale is much longer than the dynamical timescale, which means no detonation can be formed. On the other hand, above the ignition temperature, the fuel burns instantaneously. Also the energy generated by the nuclear reaction is much larger than the different choices of input temperature. Thus, the product of the detonation wave is less insensitive to the input temperature compared to the density.

Certainly a self consistent way, which is to calculate the network directly, can provide us the most accurate results regarding to the process of partial burning. However, such inclusion is beyond the current capability of our computing resource. Furthermore, in the hydrodynamics, acoustic waves are found everywhere inside the star. These waves cause fluctuations in the local temperature. These fluctuations increase the computation time significantly when a complete network is used, since the nuclear composition always adjusts itself to the local temperature, where at high temperature the typical time step is small.

B. EFFECTS OF SYMMETRY BOUNDARY

In this work we have carried out simulations of sub-Chandrasekhar SNe Ia in a quadrant of sphere. This uses a reflective boundary along the symmetry plane $z = 0$. As a result, the initial He detonation configuration, namely a one-bubble structure, corresponds to two synchronous ignitions of He detonation, one at the "north"-pole and one at the "south"-pole. It is unclear, prior to the runaway of He, how the velocity field, especially the turbulent velocity motion, may perturb the initial ignition of He. Certainly it is more likely for two He detonation bubbles to have asynchronous ignition time, or even there is only one ignition before C detonation is triggered. Therefore, it is unclear whether the C detonation can still be robustly triggered when there is a time-lapse between the two He detonation bubbles.

To do the comparison, we develop a temporary extension of our hydrodynamics code to model the hemisphere of the WD by relaxing the reflection symmetry. We place one He bubble at the "north"-pole, while another one at the "south"-pole with some time delay. In Table 3 we tabulate the configuration and initial detonation properties of our

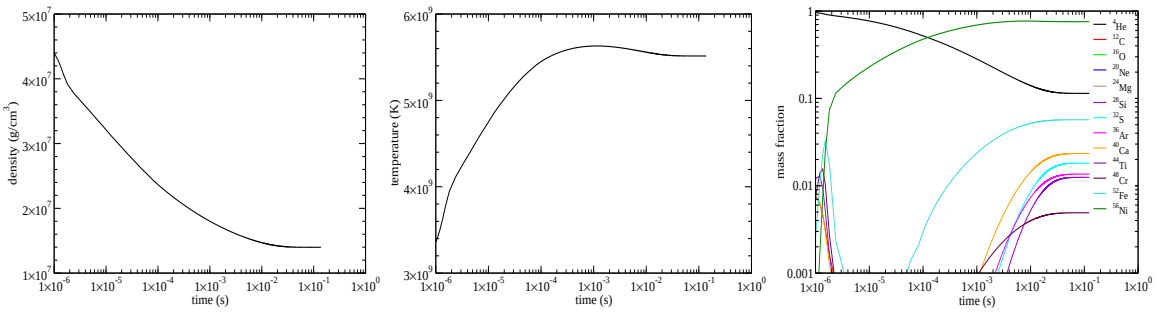

Figure 31. (left) The density evolution of He during detonation for pure He fuel at a density 10^7 g cm^{-3}. The matter is assumed to be shock-heated to above 2×10^9 K. (middle) The temperature evolution of the detonation wave at an initial density 10^7 g cm^{-3}. (right) The isotope evolution of the detonation wave at an initial density 10^7 g cm^{-3}

Table 3. The models for the study of reflection symmetry effects in the sub-Chandrasekhar SNe Ia. Delay time is the difference between the two He detonation bubble in the unit of s. "C-det?" corresponds to whether C detonation can be triggered or not. If yes, $\rho_{\rm C-det}$ and $T_{\rm C-det}$ are the density and temperature of the triggered grid in units of 10^7 g cm^{-3} and 10^9 K respectively. $t_{\rm C-det}$ is the ignition time in units of s. Position is the coordinate in units of km.

Model	Delay time	C-det?	Position	$t_{\rm C-det}$	$\rho_{\rm C-det}$	$T_{\rm C-det}$
Test-QS	0	Yes	(3420,0)	0.94	1.04	2.55
Test-HS-0	0	Yes	(3380,0)	0.94	1.06	2.84
Test-HS-1	0.2	Yes	(3290,-720)	1.03	1.09	2.83
Test-HS-2	0.4	Yes	(3120,-1400)	1.15	1.04	2.89
Test-HS-3	1.0	Yes	(1330,-2910)	1.43	1.00	2.00

test models. It can be seen that the all the cases give a positive response to the He detonation, regardless of being one or two He bubbles and their delay time. This suggests that as long as the He envelope has exceeded the marginal thickness then the shock compression, either by shock-shock collision or by shock-wall collision can create similar heating to the surface matter of the CO core.

We carry out 5 hydrodynamics simulations to extract the effects of reflection symmetry. Test-QS corresponds to the model with reflection symmetry, where we choose the same configuration as the Benchmark Model 110-100-2-50. This means the Model Test-QS is exactly the benchmark model. Models Test-HS-0 - Test-HS-3 do not assume reflection symmetry and has a He ignition delay time from 0 - 1 s. Model Test-HS-0 acts as a control test to see if the hemisphere extension is consistent with a quadrant sphere modeling; while in Model Test-HS-3 we delay the second ignition so long such that the C detonation is triggered. From Table 3, when the delay time becomes larger, the position of the C detonation moves away from the "equator", since the upper He bubble has more time to propagate before the shock collision. However, no significant change in the trigger density and temperature is observed, showing that the trigger of C detonation does not depend strongly on the minor details of the He detonation.

In Figure 32 we plot the temperature colour plots with the He and C detonation structure at 0.5 s, at the trigger of C detonation and 0.2 s after the trigger of C detonation respectively for the Model Test-HS0. The detonation structure of both He and C demonstrates a high degree of symmetry throughout the simulation. The detonation occurs at equator around the surface of CO core. The reflected shock leads to a clear distinction between the pre-heated region and post-heated region. From Table 3, it can be seen that when the two He detonations are placed explicitly, the C detonation is triggered along the "equator" of the WD at the same time as Model Test-QS. However, slight differences in density and temperature appear between the grid positions in the quadrant of sphere and hemisphere. They are different that in the Test-QS no grid is placed on the reflection plane while explicit grid is put on the reflection place in the Model Test-HS-0. As a result, it allows an explicit compression of matter on the equator when the two shocks merge.

In Figure 33 we plot similar to Figure 32 but for Model Test-HS-1. Due to the delayed He detonation, the area swept by the upper He detonation wave has a larger volume than the lower one. As a result, the collision point is

Figure 32. (Figures removed for reducing the pdf file size, see published version for full figures.) The He and C detonation structure and the temperature colour plot of Model Test-HS-0 at 0.5 s, at the trigger of C detonation and at 0.2 s after the C detonation trigger.

Figure 33. (Figures removed for reducing the pdf file size, see published version for full figures.) Similar to Figure 32, but for Model Test-HS1 at 0.5 s, at the trigger of C detonation and at 0.2 s after the C detonation trigger.

Figure 34. (Figures removed for reducing the pdf file size, see published version for full figures.) Similar to Figure 32, but for Model Test-HS2 at 0.5 s, at the trigger of C detonation and at 0.1 s after the C detonation trigger.

Figure 35. (Figures removed for reducing the pdf file size, see published version for full figures.) Similar to Figure 32, but for Model Test-HS3 at 0.5 s, at the trigger of C detonation and at 0.075 s after the C detonation trigger.

lower. Despite that, the collision point remains to be the hottest point which can trigger C detonation. Due to the assymetric expansion of the star, the detonation in the CO core has more features compared to the previous case.

In Figure 34 we plot similar to Figure 32 but for Model Test-HS-2. The further delayed second He detonation bubble allows the collision to occur at an even lower position. The newly formed C detonation can propagate as in previous cases. The shock reflection in the He envelope can be clearly seen.

In Figure 35 we plot similar to Figure 32 but for Model Test-HS-3. We delayed putting in the second detonation so long that the C detonation has been triggered beforehand. In this case, it is identical to the one-bubble scenario where the shock convergence at the "south"-pole of the He envelope creates the desired shock compression and penetration into the CO core, which heats up sufficiently the fuel for spontaneous runaway. The geometrical convergence around the "south"-pole allows the shock to be strengthened with an increasing post-shock temperature when it approaches the rotation-axis. The temperature is already adequately high to trigger the C detonation before the He shock collides with the axis. The triggered C detonation can then propagate inside the CO core.

From all these four cases it suffices to demonstrate that the C detonation can be ignited by He detonation, the reflection symmetry of the $z = 0$ plane can provide the necessary shock collision for shock compressing the fuel in order to raise its temperature for spontaneous nuclear runaway. Even without the symmetry plane, we demonstrated that the collision of He detonation, regardless of their ignition time, will provide also the necessary shock heating on the CO core surface. We also presented that in the one-bubble limit, i.e. the delay time much greater than the C detonation time, the geometric convergence in the models can also provide the required shock compression. This suggests that as long as the He envelope mass is large enough for triggering C detonation naturally, the configuration of He detonation plays a less important role for the detonation structure. Since in these tests we only aim at showing the robustness of triggering the C detonation with or without reflection symmetry, the complete nucleosynthesis and the effects of shock collision on the nuclear burning will be left as future work. However, it remains unclear whether the WD can be represented comprehensively by a sphere in hydrostatic equilibrium prior to its runaway. The effects of a non-static atmosphere, as a result of He burning before its runaway, will be an interesting future work to further test the robustness of the C detonation mechanism by bubbles.

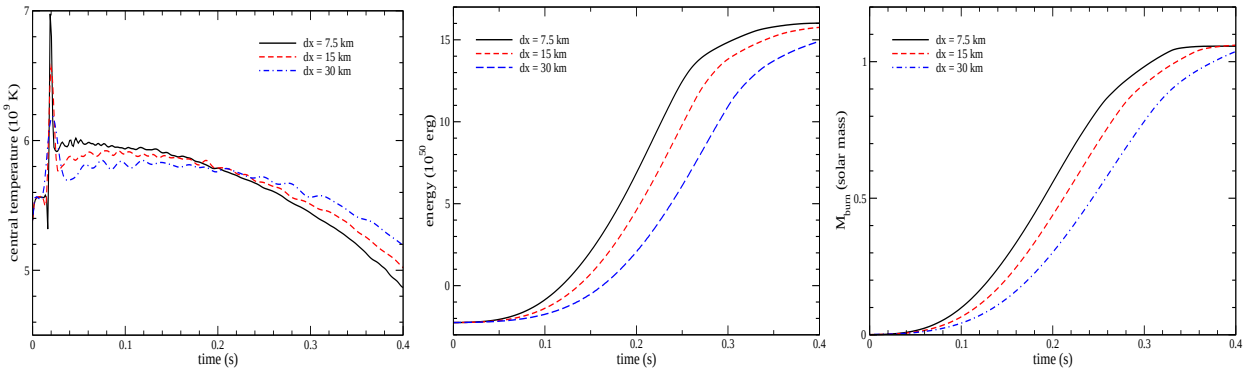

Figure 36. (left panel) The time evolution of the central temperature for the Models Test1-fine ($\Delta x = 7.5$ km), Test1 ($\Delta x = 15$ km) and Test1-coarse ($\Delta x = 7.5$ km). (middle panel) Similar to the left panel, but for the total energy. (right panel) Similar to the left panel, but for the total burnt mass.

Table 4. The model parameters for the one-dimensional resolution study. M, $M_{\rm He}$ are in unit of $M_\odot$. Δx is grid size in unit of km. $t_{\rm burn}$ is the time needed for the C-detonation wave to burn everything in unit of s. $E_{\rm fin}$ is the final asymptotic energy given by the simulation, in unit of 10^{50} erg. $T_{\rm max}$ is the maximum central temperature experienced in the simulations. The numbers in the brackets stand for the percentage difference between that model with the higher resolution model.

Model	Δx	M	$M_{\rm He}$	$t_{\rm burn}$	$E_{\rm fin}$	$T_{\rm max}$
Test1-fine	7.5	1.1	0.1	0.31	15.9	7.0
Test1	15.0	1.1	0.1	0.34 (9.6)	15.8 (0.63)	6.6 (5.7)
Test1-coarse	30.0	1.1	0.1	0.38 (11.8)	15.3 (3.2)	6.2 (6.1)

C. TEST 1: RESOLUTION STUDY IN THE PROPAGATION OF DETONATION

In the main text we have studied extensively how each of the model parameter contributes to the diversity of chemical composition. However, besides the chemical composition which should be compatible with solar composition, the simulation results should be convergent with respect to different resolution. Here we examine in more details how our models depend on the choice of resolution.

The first test is done to a static CO core with He envelope as in our benchmark model. We choose the configuration the same as Model 110-100-2-50 except for the initial He-detonation. We put a spherical C-detonation with a radius 100 km at the beginning and allow it to propagate. The spherical detonation will preserve mostly its symmetry and propagate. Thus, it is literally a one-dimensional problem. But we remark that it is still a two-dimensional problem because in cylindrical coordinate the spherical structure is broken down to $r-$ and $z-$ component along the constant radius contour.

We put the model parameters and the explosion energetics including thermodynamics information in Table 4. We choose the standard resolution at 15 km, which is the same as in the main text. A coarser model with a resolution of 30 km and a finer model with that of 7.5 km are prepared in a similar manner. We can see that when the resolution increases, the global quantities including the explosion energy and burning time converge, though it does not follow the exact scaling used in the spatial discretization scheme. The local quantity, i.e. the global maximum temperature, shows a much slower convergence rate. Despite that, the three models show a decreasing relative change, showing that the results are on the convergence side.

In Figure 36 we plot the time evolution of the central temperature, total energy and total burnt mass for the three test models. All three models show an initial peak at $t = 0.1$ s because of the shock imposed by the initial detonation. The peak temperature increases when resolution decreases. A typical change of 5 % increases is observed when Δx drops by half. After that, the star gradually expands and the star cools down. The models with a lower resolution has a lower peak temperature. Our code shows linear convergence in the temperature. It is because the smaller the grid size it has, the closer to the $1/r$ divergence when the shock converges. The cooling rate of the central grid also depends on the resolution. The model with a smaller resolution cools faster and the change of temperature shows a linear dependence. A 5 % difference can be seen at the central at $t = 0.4$ when resolution reduces by half.

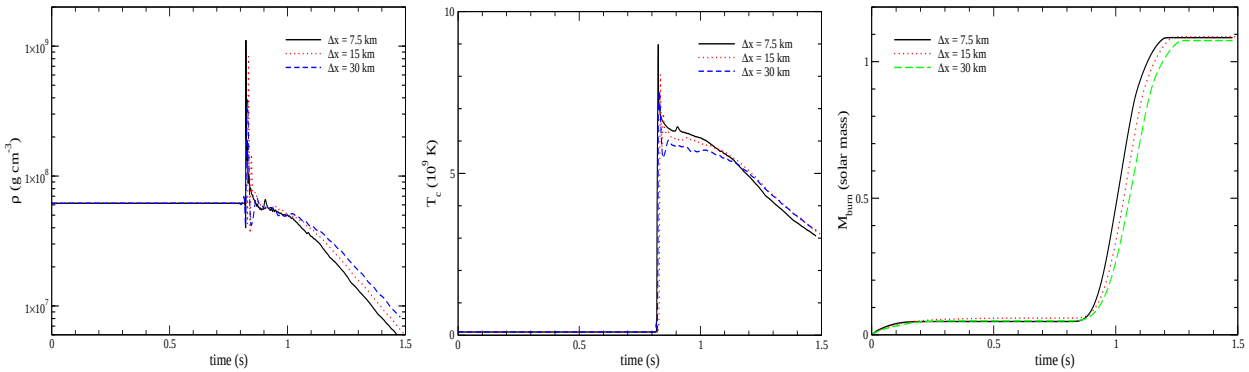

Figure 37. (left panel) The time evolution of the central temperature for the Models Test2-fine ($\Delta x = 7.5$ km), Test2 ($\Delta x = 15$ km) and Test2-coarse ($\Delta x = 30$ km). (middle panel) Similar to the left panel, but for the central density. (right panel) Similar to the left panel, but for the total burnt mass.

Table 5. The model parameters for the one-dimensional resolution study. M, $M_{\rm He}$ are in unit of $M_\odot$. Δx is grid size in unit of km. $t_{\rm burn}$ is the time needed for the C-detonation wave to burn 1 $M_\odot$ in unit of s. $\rho_{\rm max}$ is the maximum central density in the simulation, in unit of 10^8 g cm^{-3}. $T_{\rm max}$ is the maximum central temperature experienced in the simulations in units of 10^9 K. The numbers in the brackets stand for the percentage difference between that model with the higher resolution model.

Model	Δx	M	$M_{\rm He}$	$t_{\rm burn}$	$\rho_{\rm max}$	$T_{\rm max}$
Test2-fine	7.5	1.1	0.05	1.13	11.1	9.0
Test2	15.0	1.1	0.05	1.16 (2.6)	8.0 (2.8)	8.0 (11.1)
Test2-coarse	30.0	1.1	0.05	1.19 (2.6)	3.8 (5.2)	7.5 (6.3)

The total energy and its energy generation are also dependent on the spatial resolution. The total energy includes the kinetic, internal and gravitational energy. The energy growth and its final energy are also weakly dependent on the spatial resolution. Models with a higher resolution has a faster energy growth and higher final energy. The relative difference is ~ 1 % when resolution reduces by half. This suggests that when Δx decreases, the level set can capture the front surface with more details, which increases its surface area. As a result, the detonation can effectively propagate faster, and release more energy while the star has less time to expand before it is swept by the detonation wave.

The total burnt mass shows how much mass is swept up by the detonation wave. It has a similar trend as the total energy but the result is independent of the energy production algorithm. The models shows a larger and weaker scaling relation for different Δx. A smaller Δx gives a lower time for the detonation wave to complete burning the whole star. A difference of $\sim 10\%$ is observed.

D. TEST 2: RESOLUTION STUDY OF SHOCK CONVERGENCE

In this test we study how the choice of spatial resolution affects the convergence of detonation shock. Geometric convergence exists in both C- and He-detonation in different manners. For C-detonation, we have showed that "X"-Type detonation (such as Model 110-100-2-50 (X)) can result in the first C-detonation along the symmetry axis. This detonation later propagates to the center. But in the three-dimensional projection, it corresponds to a C-detonation ring shrinking into a point. Similarly, the "S"-Type detonation (such as Model 100-050-2-S50 (S)) can result in a spherical shock propagating towards center. For He-detonation, similar phenomenon occurs in the "Y"-Type detonation such as Model 110-050-2-B50 (Y). The geometric convergence occurs when the He-detonation propagate from the convergence. However, the discontinuity is described numerically in the discretized manner by the Eulerian meshes. As a result, the local thermodynamics behaviour at the point of convergence can depend strongly on the spatial resolution.

To study how the geometric convergence of shock depends on the simulation, we repeat the simulations for Model 110-050-2-S50 (S) at a spatial resolution Δx of 7.5, 15 and 30 km. We remind $\Delta x = 15$ km is the default resolution. We set up a WD with a $M = 1.1$ $M_\odot$ and $M_{\rm He} = 0.05$ $M_\odot$ at $Z = Z_\odot$. The initial He-detonation is spherical at 30 km away from the CO-core. We use the spherical He-detonation near the CO-core interface. Then we allow the He-detonation to propagate and trigger the inward propagating shock. The shock converges at the stellar core

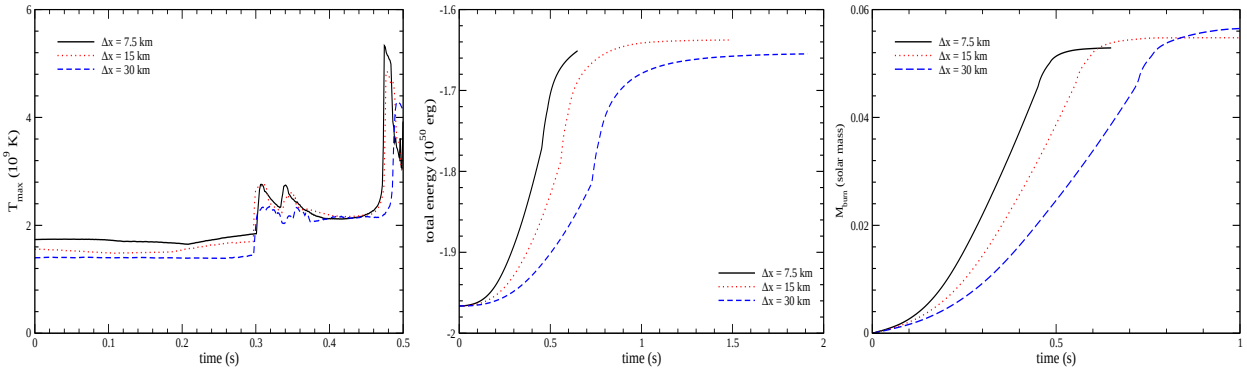

Figure 38. (left panel) The time evolution of the central temperature for the Models Test3-fine ($\Delta x = 7.5$ km), Test3 ($\Delta x = 15$ km) and Test3-coarse ($\Delta x = 30$ km). (middle panel) Similar to the left panel, but for the total energy. (right panel) Similar to the left panel, but for the total burnt mass.

Table 6. The model parameters for the one-dimensional resolution study. M, $M_{\rm He}$ are in unit of $M_\odot$. Δx is grid size in unit of km. $t_{\rm burn}$ is the time needed for the C-detonation wave to burn everything in unit of s. $E_{\rm fin}$ is the final asymptotic energy given by the simulation, in unit of 10^{50} erg. $T_{\rm max}$ is the maximum central temperature experienced in the simulations in units of 10^9 K. $2^{\rm nd}$ detonation means if the carbon detonation is triggered throughout the simulation. The numbers in the brackets stand for the percentage difference between that model with the higher resolution model.

Model	Δx	M	$M_{\rm He}$	$t_{\rm burn}$	$T_{\rm max}$	$E_{\rm fin}$	$2^{\rm nd}$ detonation
Test3-fine	7.5	1.1	0.05	0.49	4.3	∼-1.63	No
Test3	15.0	1.1	0.05	0.58 (18.4)	4.8 (11.6)	-1.64 (0.6)	No
Test3-coarse	30.0	1.1	0.05	0.75 (29.3)	5.3 (10.4)	-1.66 (1.2)	No

and triggers the C-detonation, which propagates outwards. In Table 5 we tabulate the parameters necessary for this resolution study.

In the left panel of Figure 37 we plot the evolution of central density for the three tests. The density is an important quantity not only because it is the essential part in the Euler equation, but also the energy production frequently refers density as the input parameter. In the figure, the central density has its peak at $t \sim 0.8$ s. This corresponds to the moment when the spherical shock arrives at the center of the star. The peak value can increase from 4×10^8 up to 10^9 g cm^{-3} when resolution increases. Again, this suggests that the code obtain a weakly converging result when describing the local properties in the center.

In the middle panel of Figure 37 we plot similar to the left panel but for the central temperature. The central temperature can be important especially when it is related to the burnt matter because it controls the NSE process and the electron capture process. The central temperature can increase from 7×10^9 to 9×10^9 K for the three models here. Again, smaller Δx allows a faster drop in the central temperature. The sequence does not show a convergent trend. Despite that we remind that the smaller the resolution we have, the smaller contribution the divergent result to the whole system is.

In the right panel of Figure 37 we plot the burnt mass against time. There is no significant burning at the beginning since only He is burnt. After $t = 0.9$ s, the detonation wave begins to sweep across the fuel efficiently. Again, it shows a weakly converging sequence that a smaller Δx allows faster burning of material. A reduction by 5 % by mass of the whole star to be completely burnt is observed, when resolution drops by half. This shows that, even the local quantities can rely on Δx, the finer Δx is, the smaller contribution for an individual cell to the global system, especially the center cell gives. As a result, the resolution-dependent feature is averaged out in general.

E. TEST 3: RESOLUTION STUDY OF C-DETONATION TRIGGER

In this test we study how the choice of spatial resolution affects the convergence of shock in the trigger of second (C-) detonation. In the simulation, similar to the previous test, the geometric convergence plays an important role for creating the necessary hot spot, if the initial He-detonation possesses certain symmetry in space. For example, We choose to study Model 110-100-2-3R50 (N). It is because, by comparing Models 110-100-2-50 (X), 110-100-2-2R50

(Y) and 110-100-2-3R50 (N), they do not show a regular trend in the detonation pattern. Also, given the fact that Model 110-100-2-50 (X) can trigger the second detonation, with more initial He being burnt at the beginning, Model 110-100-2-3R50 should be more probable to be ignited. Therefore, it becomes interesting to question if the choice of resolution plays a role.

To test the validity of our result, we also perform convergence study for the Model 110-100-2-3R50 (N) at three resolutions of 7.5, 15 and 30 km. Again, 15 km is the default simulation size used in our calculation. We set up the same initial model with a total mass of 1.1 $M_\odot$ and He mass of 0.1 $M_\odot$ at solar metallity. The initial detonation is a three-bubble structure located along the rotation axis, symmetry axis and diagonal line. Due to the much longer computational time for the high resolution one, it is only computed until the reflected shock reaches the axis of rotation symmetry (i.e. z-axis).

In the left panel of Figure 38 we plot the global maximum temperature against time for the three models. Due to the multiple dimensional effects in this test, the time where the system reaches its maximum temperature and the exact value are not monotonic. However, it shows a clear sign that the difference between the two models decreases when Δx drops. The peak temperature varies from 4×10^9 to 5×10^9 K. The relative change drop from $\sim 20\%$ to $\sim 5\%$ between the two sets of models. However, we notice that the hot spot is inside the He-envelope. So even it exceeds the maximum threshold temperature 3×10^9 K, suitable for matter at density below 10^7 g cm^{-3}, it does not trigger any C-detonation.

In the middle panel of Figure 38 we plot the total energy against time. This also tests the convergence of energy production rate in the He-envelope due to the absence of second detonation. The maximum energy is limited to $E = -1.6 \times 10^{50}$ erg. It can be seen that the He-detonation has a stronger effect on the energy production rate. We observe a difference in the $\sim 1\%$ of final energy by reducing half of grid size but a difference of ~ 10 % time for the model to reach the same energy.

In the right panel of Figure 38 we plot the total burnt mass against time. The maximum burnt mass is limited to $M_{\rm He} = 0.05 M_\odot$. The He-detonation has larger but weakly converging differences in its propagation against different resolution. This conforms with the energy production rate in the middle panel. They all show to burn the same amount of matter, but the amount of time differs by 20% and is weakly converging.

The above test demonstrates that the trigger of C-detonation by shock convergence is in general robust at the current resolution. However, the necessary Δx to determine the C-detonation trigger can be different, which depends on the the chemical composition and also the numerical algorithm such as how nuclear reaction scheme is implemented. For further discussion in how resolution affects the discrimination of C-detonation trigger, we refer interested readers to some recent resolution studies for the colliding WD scenario in e.g. Katz & Zingale (2019); Kushnir & Katz (2019) and for the near-Chandrasekhar mass deflagration-detonation transition scenario in e.g. Fisher et al. (2019).

F. COMPARISON OF MODELS IN THE LITERATURE

We have studied the two-dimensional SNe Ia model using the sub-Chandrasekhar mass WD with the C detonation induced by surface He detonation. In this work, we compared effects of different detonation structure. Here, we consider the realizability of the detonation structure and compare with previous works in the literature.

F.1. *Shigeyama et al. (1992)*

The spherical detonation is the same as the classical DD Model (Shigeyama et al. 1992). The model is adopted for SN1990N, which contains clear Si and Ca signatures with high velocities. The Model 105-050-2-S50 is comparable with their Model CDT5 but with two qualitative differences. The two models share a similar CO core mass with the same metallicity at $Z_\odot$. Furthermore, the spherical He-detonation setting in Model 105-050-2-S50 ensures the evolution is spherical, which is compatible to their one-dimensional simulation with spherical symmetry. In their work, the detonation is triggered by hand, assuming the He detonation on the surface has finished and sent an inward-going shock wave. Thus, there is no direct He burning considered. Second, that model assumes a direct CO detonation at the center, which comes from the assumed symmetry in the detonation wave. In our model, the He detonation is the "X"-Type detonation. They find a yield of 0.56 $M_\odot$ and 1.3×10^{51} erg for the ^{56}Ni production and total energy. Our model has a stronger detonation that we find 0.60 $M_\odot$ and 1.07×10^{51} erg respectively. The spherical detonation model is one of the higher viable shapes of detonation when the convection in the He layer is weak. In that case, the layer closest to the CO boundary has always the highest and uniform temperature. The whole layer will be the first site to trigger explosive He burning.

F.2. *Fink et al. (2007)*

We compare our one-bubble model with the models in Fink et al. (2007) in the detonation structure. They consider an isothermal WD model of total mass $0.9-1.0\ M_\odot$. They also explored different detonation pattern, including spherical, one-, two-, and five-bubble detonation structure. Their model $z4.24A\_2dq\_256$ has a similar model configuration as our Model 105-050-2-2R50.

They observe the second detonation starts at 1.08 s after the He detonation. Our model shows a very close results of 1.07 s. However, they find a yield of 0.01 $M_\odot$ unburned fuel, 0.40 $M_\odot$ ^{56}Ni and 0.51 $M_\odot$ ^{28}Si. Our model shows more ^{56}Ni production of mass 0.49 $M_\odot$ but a lower IME at 0.18 $M_\odot$. There is more ^{16}O fuel of mass 0.11 $M_\odot$. The differences between the two models come from the burning scheme. An instantaneous input of energy is provided in the model of detonation wave, while our scheme applies the three-step burning scheme. The burning of ^{16}O is suppressed when the ash temperature is not sufficiently high, especially around 10^7 g cm^{-3}, so that the estimated NQSE and NSE timescales become very long for all the burning to take place. For WD models where convection and turbulence are important, the fluid motion always disturbs the heat-generating He layer. As a result, local hot spot is possible to form. When temperature is close to the explosive burning of ^{4}He, the formation of a hot spot is likely to be the first location of He detonation.

F.3. *Shen et al. (2018)*

In Shen et al. (2018) the sub-Chandrasekhar mass WD detonation model is also modeled in the framework of dynamically driven double degenerate double detonation (DDDDDD) model. In this framework, when the two WDs pass by each other, the tidal force of the secondary WD triggers the C detonation of the primary WD, while the secondary WD later leaves the system without disrupting itself. The major difference of this physical picture from the other one is that the companion WD remains intact after the SN Ia, unlike the standard white dwarf violent merger. This provides a smaller total mass in the system, where the ejecta may explode more easily with a higher velocity. In that work, SN Ia model with a mass range of 0.8 - 1.1 $M_\odot$ with a metallicity from 0 - 2 $Z_\odot$ and C/O mass fraction ratio from 0.3 - 1 are computed in the one-dimensional limit. Here we compare one of the most similar models, the Model 100-005-1-S50, with their 1 $M_\odot$, solar metallicity, C + O = 1 Model. We choose this model because the initial detonation and the C detonation are spherically symmetric, also the final ^{56}Ni mass is similar. We have 0.6 $M_\odot$ while their model has 0.53 $M_\odot$.

In Figure 39 we plot the scaled mass fraction of the stable isotopes of the two models. We can see that in general the two models agree well qualitatively. Both models share the similar relative mass fractions of the same elements. Some minor elements, including P, Cl, Na and Sc are surprisingly close to each other, despite their relatively small amounts (subject to larger systematic uncertainty) and the very different treatments in the explosion scenario, initial configuration, explosion treatment, and in particular, the hydrodynamics. Major elements, Si, S, Ar, Ca, Fe, Ni and Zn, are still close to each other. However, their model shows a systematic higher mass fraction for the high-Y_e end isotopes (i.e. close to 0.5), e.g. ^{28}Si, ^{32}S, ^{36}Ar, ^{40}Ca, ^{52}Cr and ^{54}Fe. This shows that they have more incomplete burning such that more IMEs and light Fe-peak elements are formed. However, there are also some differences in Ti and Fe. Their model obtains a higher abundance ratios of ^{49}Ti and ^{50,52,53}Cr than our model, but a lower ratio of $^{46-48}$Ti. We note that this feature is prominent in asymmetric detonation but not in symmetric detonation. Also, their ^{55}Mn production is a few times higher, despite the low density matter in the star. A more detailed study of how He detonation and C detonation are affected by the numerical treatment will be an interesting future work.

F.4. *Polin et al. (2019)*

In Polin et al. (2019) the one-dimensional sub-Chandrasekhar mass models are also calculated for a wide range of WD masses from 0.6 to 1.2 $M_\odot$ and He envelope masses from 0.01 to 0.08 $M_\odot$ using the CASTRO code. Their work studies the observational influences from the He envelope mass. It is found that two subclasses of light curves emerge. For a lighter He envelope, the light curve resembles with some features in SNe Ia, including the correlation between mass, brightness and velocity in the spectra. For a more massive He envelope, the light curve contains early UV flux and appears to be red due to iron-peak elements on the surface and later it turns blue.

Their methodology and initial models are different from ours. In their work, the nuclear reaction is directly solved by introducing the 13-isotope network containing ^{4}He, ^{12}C, ^{16}O, ^{20}Ne, ^{24}Mg, ^{28}Si, ^{32}S, ^{36}Ar, ^{40}Ca, ^{44}Ti, ^{48}Cr, ^{52}Fe and ^{56}Fe. The nuclear reaction zone is specifically refined using the AMR option in CASTRO. A mixed transition between the CO-core and He-envelope is introduced. Also, at the beginning a width of ~ 1 km spherical He-detonation is put

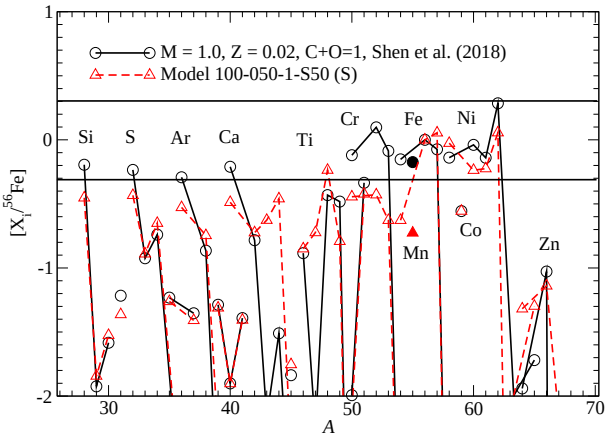

Figure 39. $[X_i/^{56}\mathrm{Fe}]$ for the model from Shen et al. (2018) (1 $M_\odot$, solar metallicity and C + O = 1) and our Model 100-005-1-S50.

in by hand. On the other hand, we use a simplified 7-isotope network patched with the three-step burning scheme. The nuclear reaction is not directly resolved but relied on the level-set, which assumes the front of the most rapid reaction is directly represented by lines, where slower nuclear reactions take place assuming a given timescale. No mixing between CO-core and He-envelope core is introduced in our initial model. Also, due to the two-dimensional nature, our models include initial He-detonations from spherical to different aspherical structure, but the typical size is larger ($\sim$ 30 km).

Since their work does not aim for nucleosynthesis, here we only compare with their global chemical yields, in particular their models with 0.05 $M_\odot$ He in the envelope. Their models show a different growth rate in the M_{Ni} as a function of M. They obtain a ^{56}Ni mass from $\sim$ 0.2, to 0.5 and then 0.8 $M_\odot$ ^{56}Ni in the 0.9, 1.0 and 1.1 $M_\odot$. On the other hand, we have 0.02, 0.6 and 0.8 $M_\odot$ ^{56}Ni respectively from our Models 090-050-2-S50 (S), 100-050-2-S50 (S) and 110-050-2-S50 (S). Large differences appear at low mass models. One major reason could be the nuclear reaction at the low density for the CO-detonation. In our model, we have used a three-step nuclear burning reaction, with the timescale dependent on the local density. On the other hand, they solve the nuclear reaction directly using the 13-isotope network in the hydrodynamics. And they also use the adaptive mesh refinement for resolving the nuclear burning at small scales. Both procedures can capture in greater details how the low-density matter achieves complete burning, which may enhance the IMEs and ^{56}Ni production. On the other hand, for a more massive WD model, our results agree with theirs well.

F.5. *Jacobs et al. (2016)*

An extension of the comparison includes the pre-supernova models evolved from multi-D hydrodynamics model. However, the exact site of nuclear runaway in our work is an model parameter. In fact, the detailed position and its runaway time can be modeled by following the exact hydrodynamics evolution over a few of convective turnover timescale. For example, in Jacobs et al. (2016) the three-dimensional sub-Chandrasekhar mass WDs of masses from 0.85 to 1.23 $M_\odot$ are studied using the low-Mach number code MAESTRO. The evolution path prior to its nuclear runaway is studied.

Three nuclear runaway types are observed: localized runaway, quasi-equilibrium and convective runaway. Localized runaway corresponds to the runaway taking place by a unique hot spot. This occurs when the convection fails to transport heat away generated from the nuclear reaction near the interface efficiently. Quasi-equilibrium stands for the opposite of the localized runaway. The convection can remove the heat efficiently so that no particular hot spot can grow. However, it is unclear finally the runaway is localized or collective. Convective runaway means the collective runaway in the form of helium nova.

In their study, there is not a clear trend in how they observed that localized runaway takes place in models with a mass 0.8, 1.1 and 1.2 $M_\odot$. Models with a mass of 1.0 $M_\odot$ tends to have quasi-equilibrium. Convective runaway takes place in the low mass model with a low M_{He}. From this it shows that for massive star model the single spot runaway, e.g. 120-050-2-50 (X) is a more realistic model than collective runaway. Models with a mass $M = 1.1$ $M_\odot$ tend to occur in a single spot runaway, and hence benchmark model including 110-100-2-50 (X) is the most likely

initial configuration. There is no clear conclusion for our benchmark models due to the quasi-equilibrium outcome for $M = 1.0\ M_\odot$. There is no models of mass $0.9\ M_\odot$ presented in their work to compare with ours.

REFERENCES

Abe, R. 1959, Progress of Theoretical Physics, 22, 213

Arnett, D. 1996, Supernovae and Nucleosynthesis: An Investigation of the History of Matter from the Big Bang to the Present

Ashall, C., Mazzali, P., Bersier, D., et al. 2014, Mon. Not. R. astr. Soc., 445, 4427

Benvenuto, O. G., Panei, J. A., Nomoto, K., Kitamura, H., & Hachisu, I. 2015, ApJL, 809, L6

Bergström, L., & Goobar, A. 2004, Cosmology and Particle Astrophysics (Springer), doi:10.1007/3-540-37719-0

Branch, D., & Wheeler, J. C. 2017, Supernova Explosions, doi:10.1007/978-3-662-55054-0

Brown, P. J., Smitka, M. T., Wang, L., et al. 2015, ApJ, 805, 74

Calder, A. C., Townsley, D. M., Seitenzahl, I. R., et al. 2007, ApJ, 656, 313

Cenko, S. B., Fllippenko, A. V., & Silverman, J. M. 2012, CBET, 3111, 2

Churazov, E., Sunyaev, R., Isern, J., et al. 2015, ApJ, 812, 62

Dan, M., Guillochon, J., Brüggen, M., Ramirez-Ruiz, E., & Rosswog, S. 2015, MNRAS, 454, 4411

Dan, M., Rosswog, S., Guillochon, J., & Ramirez-Ruiz, E. 2011, ApJ, 737, 89

Dave, P., Kashyap, R., Fisher, R., et al. 2017, ApJ, 841, 58

Diehl, R., Siegert, T., Hillebrandt, W., et al. 2015a, Science, 345, 1162

—. 2015b, Astron. Astrophys., 574, A72

Dimitriadis, G., Suillivan, M., Kerzendorf, W., et al. 2017, Mon. Not. R. astr. Soc., 468, 3798

Feltzing, A., Fohlman, M., & Bensby, T. 2007, Astron. Astrophys., 467, 665

Fink, M., Hillebrandt, W., & Röpke, F. K. 2007, A&A, 476, 1133

Fink, M., Röpke, F. K., Hillebrandt, W., et al. 2010, A&A, 514, A53

Fisher, R., Mozumdar, P., & Casabona, G. 2019, ApJ, 876, 64

Foley, R. J., Fox, O. D., McCully, C., et al. 2014, Mon. Not. R. astr. Soc., 443, 2887

Fryer, C. L., Ruiter, A. J., Belczynski, K., et al. 2010, ApJ, 725, 296

Goobar, A., Johansson, J., Amanullah, R., et al. 2014, ApJ, 784, 12

Graur, O., Zurek, D., Shara, M. M., et al. 2016, ApJ, 819, 36

Guerrero, J., García-Berro, E., & Isern, J. 2004, A&A, 413, 257

Hillebrandt, W., & Niemeyer, J. C. 2000, Annu. Rev. Astron. Astrophys., 38, 191

Isern, J., Jean, P., Bravo, E., et al. 2016, Astron. Astrophys., 588, 67

Iwamoto, K., Brachwitz, F., Nomoto, K., et al. 1999, ApJS, 125, 439

Jacobs, A. M., Zingale, M., Nonaka, A., Almgren, A. S., & Bell, J. B. 2016, ApJ, 827, 84

Jha, S. W. 2017, Handbook of Supernovae, ed. A. W. Alsabti & P. Murdin (Springer), 375

Jiang, J.-A., Doi, M., Maeda, K., et al. 2017, Nature, 550, 80

Kandrashoff, M., Cenko, S. B., & Li, W. 2012, CBET, 3111, 1

Kasen, D. 2010, ApJ, 708, 1025

Katz, M. P., & Zingale, M. 2019, ApJ, 874, 169

Kitamura, H. 2000, ApJ, 539, 888

Kushnir, D., & Katz, B. 2019, arXiv e-prints, arXiv:1904.10001

Leung, S.-C., Chu, M.-C., & Lin, L.-M. 2015a, Mon. Not. R. astr. Soc., 454, 1238

—. 2015b, ApJ, 812, 110

Leung, S.-C., & Nomoto, K. 2017, in 14th International Symposium on Nuclei in the Cosmos (NIC2016), ed. S. Kubono, T. Kajino, S. Nishimura, T. Isobe, S. Nagataki, T. Shima, & Y. Takeda (JPS Conf. Proc., Tokyo), 020506

Leung, S.-C., & Nomoto, K. 2018, ApJ, 861, 143

Li, W., Flippenko, A. V., & Treffers, R. R. 2001, ApJ, 546, 734

Livne, E. 1990, ApJL, 354, L53

Livne, E., & Arnett, D. 1995, ApJ, 452, 62

Livne, E., & Glasner, A. S. 1990, ApJ, 361, 244

—. 1991, ApJ, 370, 272

Maoz, D., Mannucci, F., Li, W., et al. 2011, MNRAS, 412, 1508

Maoz, D., Mannucci, F., & Nelemans, G. 2014, ARA&A, 52, 107

Marion, G. H., Kirschner, R. P., Foley, R. J., Challis, P., & Irwin, J. 2012, CBET, 3111, 3

Moll, R., Raskin, C., Kasen, D., & Woosley, S. E. 2014, ApJ, 785, 105

Moll, R., & Woosley, S. E. 2013, ApJ, 774, 137

Moore, K., Townsley, D. M., & Bildsten, L. 2013, ApJ, 776, 97

Nabi, J.-U., & Klapdor-Kleingrothaus, H. V. 1999, ADNDT, 71, 149

—. 2004, ADNDT, 88, 237

Niemeyer, J. C., Hillebrandt, W., & Woosley, S. E. 1995, ApJ, 452, 979
Nomoto, K. 1982a, ApJ, 253, 798
—. 1982b, ApJ, 257, 780
—. 1984, ApJ, 277, 791
Nomoto, K., Iwamoto, K., & Kishimoto, N. 1997, Science, 276, 1378
Nomoto, K., & Leung, S.-C. 2017, Handbook of Supernovae, ed. A. W. Alsabti & P. Murdin (Springer), 1275
—. 2018, SSRv, 214, 67
Nomoto, K., Sugimoto, D., & Neo, S. 1976, Ap&SS, 39, L37
Nomoto, K., Thielemann, F. K., & Yokoi, K. 1984, ApJ, 286, 644
Nugent, P., Sullivan, M., Cenko, S. B., et al. 2011, nature, 480, 344
Osher, S., & Sethian, J. A. 1988, JCP, 79, 12
Pakmor, R. 2017, Violent Mergers, ed. A. W. Alsabti & P. Murdin, 1257
Pakmor, R., Kromer, M., Taubenberger, S., & Springel, V. 2013, ApJL, 770, L8
Polin, A., Nugent, P., & Kasen, D. 2019, ApJ, 873, 84
Rasio, F. A., & Shapiro, S. L. 1995, ApJ, 438, 887
Raskin, C., Kasen, D., Moll, R., Schwab, J., & Woosley, S. 2014, ApJ, 788, 75
Raskin, C., Scannapieco, E., Fryer, C., Rockefeller, G., & Timmes, F. X. 2012, ApJ, 746, 62
Rauscher, T., & Thielemann, F. K. 2000, ADNDT, 75, 1
Reddy, B. E., Tomkin, J., Lambert, D. L., & Prieto, C. A. 2003, Mon. Not. R. astr. Soc., 340, 304
Reinecke, M., Hillebrandt, W., Niemeyer, J. C., & Klein, R. 1999, Astron. Astrophys., 347, 731
Roepke, F. K., & Hillebrandt, W. 2005, Astron. Astrophys., 431, 635
Sato, Y., Nakasato, N., Tanikawa, A., et al. 2015, ApJ, 807, 105
Segretain, L., Chabrier, G., & Mochkovitch, R. 1997, ApJ, 481, 355
Seitenzahl, I. R., Ropeke, F. K., Fink, M., & Pakmor, R. 2010, Mon. Not. R. astr. Soc., 407, 2297
Shappee, B. J., & Stanek, K. Z. 2011, ApJ, 733, 124
Shappee, B. J., Stanek, K. Z., Kochanek, C. S., & Garnavich, P. M. 2017, ApJ, 841, 48
Sharpe, G. J. 1999, Mon. Not. R. astr. Soc., 310, 1039
Shen, K. J., Kasen, D., Miles, B. J., & Townsley, D. M. 2018, ApJ, 854, 52
Shigeyama, T., Nomoto, K., Yamaoka, H., & Thielemann, F.-K. 1992, ApJ, 386, L13
Sim, S. A., Fink, M., Kromer, M., et al. 2012, MNRAS, 420, 3003
Sim, S. A., Roepke, F. K., Hillebrandt, W., et al. 2010, ApJ, 714, L52
Sobeck, J. S., Ivans, I. I., Simmerer, J. A., et al. 2006, Astron. J., 131, 2949
Taubenberger, S. 2017, Handbook of Supernovae, ed. A. W. Alsabti & P. Murdin (Springer), 317
Telesco, C. M., Hoeflich, P., Li, D., et al. 2015, ApJ, 798, 93
Timmes, F., Fryer, C., Timmes, F., et al. 2019, in BAAS, Vol. 51, 2
Timmes, F. X. 1999, ApJ, 124, 241
Timmes, F. X., & Arnett, D. 1999, ApJ, 125, 277
Timmes, F. X., & Swesty, D. 1999, ApJS, 126, 501
Townsley, D. M., Calder, A. C., Asida, S. M., et al. 2007, ApJ, 668, 1118
Travaglio, C., Hillebrandt, W., Reinecke, M., & Thielemann, F.-K. 2004, Astron. Astrophys., 425, 1029
Umeda, H., Nomoto, K., Yamaoka, H., & Wanajo, S. 1999, ApJ, 513, 861
Woosley, S. E., & Kasen, D. 2011, ApJ, 734, 38
Woosley, S. E., Taam, R. E., & Weaver, T. A. 1986, ApJ, 301, 601
Yamaguchi, H., Eriksen, K. A., Badenes, C., et al. 2014, ApJ, 780, L136
Yamaguchi, H., et al. 2015, ApJ, 801, L31
Yang, Y., Wang, L., Baade, D., et al. 2018, ApJ, 852, 89
Yoon, S.-C., Podsiadlowski, P., & Rosswog, S. 2007, MNRAS, 380, 933
Yungelson, L. R. 2005, in Astrophysics and Space Science Library, Vol. 332, White dwarfs: cosmological and galactic probes, ed. E. M. Sion, S. Vennes, & H. L. Shipman (Springer), 163–173

Table 7. The nucleosynthesis yields for the stable isotopes of the benchmark model at different metallicity. The model at solar metallicity is Model 110-100-2-50. Masses are in units of solar mass.

Isotope	$Z = 0$	$Z = 0.1\ Z_\odot$	$Z = 0.5\ Z_\odot$	$Z = Z_\odot$	$Z = 2\ Z_\odot$	$Z = 3\ Z_\odot$	$Z = 5\ Z_\odot$
^{12}C	3.39×10^{-3}	3.38×10^{-3}	3.38×10^{-3}	3.35×10^{-3}	3.29×10^{-3}	2.62×10^{-3}	2.20×10^{-3}
^{13}C	3.33×10^{-10}	1.22×10^{-10}	3.41×10^{-10}	1.25×10^{-9}	4.59×10^{-9}	2.9×10^{-8}	1.20×10^{-8}
^{14}N	1.16×10^{-8}	4.53×10^{-9}	1.37×10^{-8}	3.80×10^{-8}	9.63×10^{-8}	6.40×10^{-7}	9.43×10^{-8}
^{15}N	2.44×10^{-6}	3.97×10^{-8}	3.2×10^{-9}	1.8×10^{-9}	4.42×10^{-10}	1.86×10^{-9}	6.88×10^{-10}
^{16}O	1.14×10^{-1}	1.14×10^{-1}	1.16×10^{-1}	1.17×10^{-1}	1.19×10^{-1}	1.12×10^{-1}	1.4×10^{-1}
^{17}O	1.86×10^{-10}	5.92×10^{-10}	5.31×10^{-9}	2.8×10^{-8}	6.32×10^{-8}	1.44×10^{-7}	5.44×10^{-8}
^{18}O	7.64×10^{-12}	2.4×10^{-11}	1.37×10^{-10}	3.4×10^{-10}	4.87×10^{-10}	2.67×10^{-9}	1.5×10^{-9}
^{19}F	3.67×10^{-10}	5.26×10^{-11}	1.78×10^{-11}	3.28×10^{-11}	1.5×10^{-10}	3.31×10^{-10}	3.46×10^{-10}
^{20}Ne	3.98×10^{-3}	3.96×10^{-3}	4.4×10^{-3}	4.0×10^{-3}	3.86×10^{-3}	3.42×10^{-3}	3.16×10^{-3}
^{21}Ne	1.16×10^{-8}	1.5×10^{-8}	6.10×10^{-8}	2.17×10^{-7}	7.58×10^{-7}	2.20×10^{-6}	3.85×10^{-6}
^{22}Ne	1.16×10^{-8}	9.45×10^{-6}	4.72×10^{-5}	9.45×10^{-5}	1.89×10^{-4}	1.82×10^{-4}	3.1×10^{-4}
^{23}Na	7.18×10^{-6}	7.71×10^{-6}	1.1×10^{-5}	1.47×10^{-5}	2.46×10^{-5}	4.4×10^{-5}	6.5×10^{-5}
^{24}Mg	1.70×10^{-2}	1.60×10^{-2}	1.11×10^{-2}	8.26×10^{-3}	5.46×10^{-3}	3.77×10^{-3}	2.66×10^{-3}
^{25}Mg	2.15×10^{-7}	3.49×10^{-6}	1.53×10^{-5}	3.89×10^{-5}	9.28×10^{-5}	1.50×10^{-4}	2.61×10^{-4}
^{26}Mg	2.36×10^{-6}	7.52×10^{-6}	2.80×10^{-5}	5.60×10^{-5}	1.27×10^{-4}	2.47×10^{-4}	5.85×10^{-4}
^{26}Al	2.86×10^{-29}	2.86×10^{-29}	2.86×10^{-29}	2.86×10^{-29}	2.86×10^{-29}	2.86×10^{-29}	1.0×10^{-10}
^{27}Al	7.37×10^{-5}	2.6×10^{-4}	5.27×10^{-4}	6.50×10^{-4}	6.97×10^{-4}	6.39×10^{-4}	6.56×10^{-4}
^{28}Si	1.17×10^{-1}	1.22×10^{-1}	1.36×10^{-1}	1.35×10^{-1}	1.32×10^{-1}	1.30×10^{-1}	1.4×10^{-1}
^{29}Si	6.15×10^{-5}	3.20×10^{-4}	5.66×10^{-4}	8.76×10^{-4}	1.57×10^{-3}	2.13×10^{-3}	3.64×10^{-3}
^{30}Si	3.81×10^{-5}	6.74×10^{-5}	7.2×10^{-4}	1.62×10^{-3}	3.62×10^{-3}	5.59×10^{-3}	1.10×10^{-2}
^{31}P	9.57×10^{-5}	5.89×10^{-5}	2.33×10^{-4}	3.97×10^{-4}	6.62×10^{-4}	8.36×10^{-4}	1.8×10^{-3}
^{32}S	5.40×10^{-2}	5.28×10^{-2}	6.14×10^{-2}	6.8×10^{-2}	5.69×10^{-2}	5.33×10^{-2}	3.91×10^{-2}
^{33}S	5.1×10^{-5}	1.32×10^{-4}	2.73×10^{-4}	3.72×10^{-4}	4.95×10^{-4}	5.45×10^{-4}	5.41×10^{-4}
^{34}S	6.96×10^{-6}	1.26×10^{-4}	1.19×10^{-3}	2.62×10^{-3}	5.68×10^{-3}	8.65×10^{-3}	1.22×10^{-2}
^{36}S	1.19×10^{-9}	2.76×10^{-9}	3.86×10^{-8}	1.77×10^{-7}	1.53×10^{-6}	4.80×10^{-6}	1.51×10^{-5}
^{35}Cl	1.2×10^{-5}	2.17×10^{-5}	8.55×10^{-5}	1.51×10^{-4}	2.41×10^{-4}	2.45×10^{-4}	1.90×10^{-4}
^{37}Cl	5.1×10^{-6}	1.10×10^{-5}	2.39×10^{-5}	3.26×10^{-5}	4.31×10^{-5}	4.65×10^{-5}	4.30×10^{-5}
^{36}Ar	1.8×10^{-2}	9.79×10^{-3}	1.4×10^{-2}	9.73×10^{-3}	8.24×10^{-3}	7.39×10^{-3}	5.25×10^{-3}
^{38}Ar	2.93×10^{-6}	6.44×10^{-5}	6.1×10^{-4}	1.32×10^{-3}	2.76×10^{-3}	3.98×10^{-3}	4.53×10^{-3}
^{40}Ar	2.32×10^{-10}	2.41×10^{-10}	8.66×10^{-10}	3.35×10^{-9}	3.53×10^{-8}	1.14×10^{-7}	2.94×10^{-7}
^{39}K	9.47×10^{-6}	2.30×10^{-5}	7.10×10^{-5}	1.7×10^{-4}	1.45×10^{-4}	1.49×10^{-4}	1.5×10^{-4}
^{40}K	4.96×10^{-8}	5.13×10^{-8}	8.32×10^{-8}	1.23×10^{-7}	2.25×10^{-7}	2.24×10^{-7}	1.15×10^{-7}
^{41}K	2.12×10^{-6}	3.87×10^{-6}	6.60×10^{-6}	8.47×10^{-6}	9.95×10^{-6}	9.58×10^{-6}	7.29×10^{-6}
^{40}Ca	1.11×10^{-2}	9.73×10^{-3}	9.38×10^{-3}	8.49×10^{-3}	7.14×10^{-3}	6.79×10^{-3}	5.45×10^{-3}
^{42}Ca	2.55×10^{-6}	4.15×10^{-6}	2.13×10^{-5}	4.53×10^{-5}	8.90×10^{-5}	1.17×10^{-4}	1.12×10^{-4}
^{43}Ca	1.29×10^{-5}	1.30×10^{-5}	1.32×10^{-5}	1.30×10^{-5}	1.31×10^{-5}	1.30×10^{-5}	1.20×10^{-5}
^{44}Ca	5.52×10^{-4}	5.49×10^{-4}	5.15×10^{-4}	5.14×10^{-4}	5.13×10^{-4}	5.13×10^{-4}	4.74×10^{-4}
^{46}Ca	6.40×10^{-12}	6.41×10^{-12}	2.80×10^{-11}	1.78×10^{-10}	9.73×10^{-10}	7.95×10^{-9}	2.18×10^{-9}
^{48}Ca	1.93×10^{-15}	1.93×10^{-15}	1.53×10^{-14}	9.31×10^{-12}	7.31×10^{-14}	1.36×10^{-10}	2.20×10^{-12}
^{45}Sc	1.54×10^{-6}	1.61×10^{-6}	1.60×10^{-6}	1.67×10^{-6}	1.72×10^{-6}	1.61×10^{-6}	1.45×10^{-6}
^{46}Ti	8.89×10^{-6}	9.57×10^{-6}	1.96×10^{-5}	2.94×10^{-5}	4.46×10^{-5}	5.13×10^{-5}	4.25×10^{-5}
^{47}Ti	8.26×10^{-5}	8.28×10^{-5}	8.57×10^{-5}	8.61×10^{-5}	8.63×10^{-5}	7.71×10^{-5}	7.21×10^{-5}
^{48}Ti	5.10×10^{-3}	5.7×10^{-3}	4.89×10^{-3}	4.87×10^{-3}	4.85×10^{-3}	4.27×10^{-3}	4.54×10^{-3}
^{49}Ti	5.11×10^{-5}	5.50×10^{-5}	5.11×10^{-5}	5.24×10^{-5}	5.30×10^{-5}	4.97×10^{-5}	5.37×10^{-5}
^{50}Ti	2.74×10^{-9}	2.74×10^{-9}	8.21×10^{-9}	1.22×10^{-5}	1.8×10^{-8}	5.2×10^{-7}	9.39×10^{-9}
^{50}V	4.91×10^{-7}	4.91×10^{-7}	8.36×10^{-7}	8.42×10^{-7}	8.43×10^{-7}	1.73×10^{-6}	2.43×10^{-7}
^{51}V	6.10×10^{-4}	6.12×10^{-4}	5.77×10^{-4}	5.89×10^{-4}	5.93×10^{-4}	5.62×10^{-4}	5.70×10^{-4}

Table 8. *cont′d* of Table 7.

Isotope	$Z = 0$	$Z = 0.1$	$Z = 0.5$	$Z = 1$	$Z = 2$	$Z = 3$	$Z = 5$
^{50}Cr	1.0×10^{-4}	1.7×10^{-4}	1.50×10^{-4}	2.18×10^{-4}	3.50×10^{-4}	4.46×10^{-4}	5.18×10^{-4}
^{52}Cr	1.78×10^{-2}	1.76×10^{-2}	1.59×10^{-2}	1.60×10^{-2}	1.56×10^{-2}	1.57×10^{-2}	1.73×10^{-2}
^{53}Cr	4.25×10^{-4}	4.74×10^{-4}	4.39×10^{-4}	4.87×10^{-4}	5.20×10^{-4}	5.96×10^{-4}	7.64×10^{-4}
^{54}Cr	8.73×10^{-6}	8.73×10^{-6}	1.28×10^{-5}	1.37×10^{-4}	1.30×10^{-5}	1.72×10^{-5}	6.57×10^{-6}
^{55}Mn	1.79×10^{-3}	1.95×10^{-3}	1.89×10^{-3}	2.28×10^{-3}	2.60×10^{-3}	3.85×10^{-3}	7.26×10^{-3}
^{54}Fe	8.76×10^{-4}	1.36×10^{-3}	3.59×10^{-3}	7.80×10^{-3}	1.23×10^{-2}	1.94×10^{-2}	3.96×10^{-2}
^{56}Fe	6.73×10^{-1}	6.69×10^{-1}	6.34×10^{-1}	6.10×10^{-1}	5.83×10^{-1}	5.57×10^{-1}	5.15×10^{-1}
^{57}Fe	1.51×10^{-2}	1.60×10^{-2}	1.83×10^{-2}	2.12×10^{-2}	2.52×10^{-2}	2.84×10^{-2}	3.30×10^{-2}
^{58}Fe	6.90×10^{-6}	6.90×10^{-6}	9.56×10^{-6}	4.39×10^{-4}	9.61×10^{-6}	1.12×10^{-5}	3.94×10^{-6}
^{60}Fe	1.6×10^{-13}	1.1×10^{-13}	5.65×10^{-13}	1.34×10^{-9}	5.63×10^{-13}	4.99×10^{-10}	1.88×10^{-14}
^{59}Co	2.25×10^{-4}	2.87×10^{-4}	5.38×10^{-4}	7.19×10^{-4}	7.79×10^{-4}	7.42×10^{-4}	6.80×10^{-4}
^{58}Ni	4.35×10^{-3}	5.59×10^{-3}	1.56×10^{-2}	3.26×10^{-2}	5.80×10^{-2}	8.56×10^{-2}	1.40×10^{-1}
^{60}Ni	1.0×10^{-2}	1.2×10^{-2}	9.8×10^{-3}	8.28×10^{-3}	6.37×10^{-3}	5.34×10^{-3}	3.57×10^{-3}
^{61}Ni	5.14×10^{-4}	5.26×10^{-4}	5.85×10^{-4}	5.99×10^{-4}	5.98×10^{-4}	5.47×10^{-4}	4.63×10^{-4}
^{62}Ni	4.81×10^{-4}	6.51×10^{-4}	1.33×10^{-3}	2.20×10^{-3}	2.92×10^{-3}	3.30×10^{-3}	3.63×10^{-3}
^{64}Ni	1.43×10^{-9}	1.44×10^{-9}	3.64×10^{-9}	6.96×10^{-7}	3.55×10^{-9}	4.69×10^{-8}	3.77×10^{-10}
^{63}Cu	5.19×10^{-6}	6.28×10^{-6}	4.98×10^{-6}	5.59×10^{-6}	6.16×10^{-6}	6.44×10^{-6}	7.66×10^{-6}
^{65}Cu	1.73×10^{-5}	1.74×10^{-5}	1.73×10^{-5}	1.76×10^{-5}	1.74×10^{-5}	1.62×10^{-5}	1.39×10^{-5}
^{64}Zn	2.13×10^{-4}	1.88×10^{-4}	1.20×10^{-4}	1.16×10^{-4}	1.12×10^{-4}	1.0×10^{-4}	8.22×10^{-5}
^{66}Zn	3.87×10^{-5}	4.6×10^{-5}	4.33×10^{-5}	5.2×10^{-5}	5.65×10^{-5}	5.75×10^{-5}	6.31×10^{-5}
^{67}Zn	4.83×10^{-6}	4.83×10^{-6}	4.18×10^{-6}	4.36×10^{-6}	4.20×10^{-6}	3.70×10^{-6}	3.97×10^{-6}
^{68}Zn	6.64×10^{-6}	6.37×10^{-6}	7.52×10^{-6}	7.56×10^{-6}	7.51×10^{-6}	6.36×10^{-6}	4.42×10^{-6}
^{70}Zn	1.99×10^{-16}	2.38×10^{-16}	2.40×10^{-15}	1.10×10^{-13}	1.16×10^{-15}	6.22×10^{-12}	4.92×10^{-17}

Table 9. Similar to Table 7 but for the radioactive isotopes of the benchmark model. Masses are in units of solar mass.

Z (Z_{odot})	$Z = 0$	$Z = 0.1$	$Z = 0.5$	$Z = 1$	$Z = 2$	$Z = 3$	$Z = 5$
^{22}Na	7.32×10^{-9}	6.59×10^{-9}	1.12×10^{-8}	1.25×10^{-8}	1.1×10^{-8}	7.67×10^{-9}	5.26×10^{-9}
^{26}Al	1.91×10^{-6}	4.30×10^{-6}	7.4×10^{-6}	6.98×10^{-6}	4.45×10^{-6}	2.40×10^{-6}	1.15×10^{-6}
^{39}Ar	5.90×10^{-9}	6.5×10^{-9}	1.28×10^{-8}	1.99×10^{-8}	5.54×10^{-8}	1.5×10^{-7}	1.1×10^{-7}
^{40}K	4.99×10^{-8}	5.16×10^{-8}	8.37×10^{-8}	1.23×10^{-7}	2.26×10^{-7}	2.25×10^{-7}	1.15×10^{-7}
^{41}Ca	2.4×10^{-6}	3.63×10^{-6}	6.65×10^{-6}	8.49×10^{-6}	9.99×10^{-6}	9.51×10^{-6}	7.23×10^{-6}
^{44}Ti	5.52×10^{-4}	5.50×10^{-4}	5.15×10^{-4}	5.14×10^{-4}	5.12×10^{-4}	5.15×10^{-4}	4.72×10^{-4}
^{48}V	2.93×10^{-6}	2.94×10^{-6}	3.22×10^{-6}	3.26×10^{-6}	3.30×10^{-6}	2.81×10^{-6}	2.9×10^{-6}
^{49}V	3.86×10^{-6}	3.86×10^{-6}	5.9×10^{-6}	5.19×10^{-6}	5.40×10^{-6}	5.30×10^{-6}	3.44×10^{-6}
^{53}Mn	8.39×10^{-5}	8.40×10^{-5}	9.34×10^{-5}	1.6×10^{-4}	1.35×10^{-4}	1.84×10^{-4}	2.16×10^{-4}
^{60}Fe	1.58×10^{-12}	1.58×10^{-12}	8.29×10^{-12}	2.1×10^{-8}	8.29×10^{-12}	7.23×10^{-9}	2.64×10^{-13}
^{56}Co	1.14×10^{-4}	1.15×10^{-4}	8.58×10^{-5}	8.95×10^{-5}	9.2×10^{-5}	8.92×10^{-5}	1.51×10^{-4}
^{57}Co	8.77×10^{-5}	8.79×10^{-5}	8.84×10^{-5}	1.47×10^{-4}	1.3×10^{-4}	9.99×10^{-5}	1.7×10^{-4}
^{60}Co	1.21×10^{-8}	1.21×10^{-8}	3.6×10^{-8}	8.90×10^{-8}	3.6×10^{-8}	4.63×10^{-7}	3.44×10^{-9}
^{56}Ni	6.73×10^{-1}	6.69×10^{-1}	6.33×10^{-1}	6.8×10^{-1}	5.82×10^{-1}	5.55×10^{-1}	5.13×10^{-1}
^{57}Ni	1.50×10^{-2}	1.59×10^{-2}	1.82×10^{-2}	2.10×10^{-2}	2.51×10^{-2}	2.83×10^{-2}	3.29×10^{-2}
^{59}Ni	4.11×10^{-5}	4.11×10^{-5}	4.9×10^{-5}	7.33×10^{-5}	4.65×10^{-5}	4.82×10^{-5}	8.84×10^{-5}
^{63}Ni	4.74×10^{-10}	4.75×10^{-10}	1.55×10^{-9}	9.31×10^{-8}	1.54×10^{-9}	9.77×10^{-8}	1.11×10^{-10}

Table 10. The nucleosynthesis yields for the stable isotopes of the benchmark model with a spherical He detonation as a trigger based on Model 110-050-2-B50 at solar metallicity. Masses are in units of solar mass.

Z ($Z_\odot$)	0	0.1	0.5	1	2	3	5
^{12}C	4.10×10^{-3}	4.9×10^{-3}	4.5×10^{-3}	4.2×10^{-3}	3.95×10^{-3}	3.89×10^{-3}	3.77×10^{-3}
^{13}C	3.66×10^{-10}	2.36×10^{-10}	2.13×10^{-9}	8.97×10^{-9}	5.42×10^{-8}	8.85×10^{-8}	2.8×10^{-7}
^{14}N	1.24×10^{-8}	8.32×10^{-9}	3.57×10^{-8}	1.17×10^{-7}	5.17×10^{-7}	8.47×10^{-7}	1.95×10^{-6}
^{15}N	1.94×10^{-6}	4.25×10^{-8}	3.71×10^{-9}	1.38×10^{-9}	1.49×10^{-9}	2.65×10^{-9}	8.42×10^{-9}
^{16}O	9.80×10^{-2}	9.93×10^{-2}	1.1×10^{-1}	1.2×10^{-1}	1.4×10^{-1}	1.4×10^{-1}	1.2×10^{-1}
^{17}O	2.98×10^{-10}	1.50×10^{-9}	1.52×10^{-8}	4.32×10^{-8}	8.5×10^{-8}	1.6×10^{-7}	1.52×10^{-7}
^{18}O	1.13×10^{-11}	4.34×10^{-11}	1.94×10^{-10}	5.10×10^{-10}	1.96×10^{-9}	4.5×10^{-9}	1.31×10^{-8}
^{19}F	3.96×10^{-10}	6.70×10^{-11}	2.65×10^{-11}	6.80×10^{-11}	2.17×10^{-10}	3.97×10^{-10}	8.63×10^{-10}
^{20}Ne	4.90×10^{-3}	4.87×10^{-3}	4.80×10^{-3}	4.72×10^{-3}	4.53×10^{-3}	4.34×10^{-3}	4.3×10^{-3}
^{21}Ne	1.39×10^{-8}	1.62×10^{-8}	1.13×10^{-7}	4.33×10^{-7}	1.49×10^{-6}	3.5×10^{-6}	8.24×10^{-6}
^{22}Ne	1.43×10^{-8}	9.46×10^{-6}	4.72×10^{-5}	9.46×10^{-5}	1.92×10^{-4}	2.97×10^{-4}	5.24×10^{-4}
^{23}Na	9.57×10^{-6}	1.2×10^{-5}	1.38×10^{-5}	2.10×10^{-5}	3.61×10^{-5}	5.49×10^{-5}	1.9×10^{-4}
^{24}Mg	1.66×10^{-2}	1.55×10^{-2}	1.14×10^{-2}	8.62×10^{-3}	5.74×10^{-3}	4.33×10^{-3}	3.8×10^{-3}
^{25}Mg	2.89×10^{-7}	3.66×10^{-6}	1.94×10^{-5}	4.99×10^{-5}	1.18×10^{-4}	1.88×10^{-4}	3.64×10^{-4}
^{26}Mg	3.16×10^{-6}	9.62×10^{-6}	3.71×10^{-5}	7.47×10^{-5}	1.61×10^{-4}	2.94×10^{-4}	8.17×10^{-4}
^{26}Al	2.86×10^{-29}	2.86×10^{-29}	2.86×10^{-29}	2.86×10^{-29}	2.86×10^{-29}	3.61×10^{-28}	4.8×10^{-28}
^{27}Al	8.57×10^{-5}	2.30×10^{-4}	5.81×10^{-4}	7.17×10^{-4}	7.70×10^{-4}	7.78×10^{-4}	8.34×10^{-4}
^{28}Si	1.5×10^{-1}	1.10×10^{-1}	1.11×10^{-1}	1.10×10^{-1}	1.8×10^{-1}	1.6×10^{-1}	1.0×10^{-1}
^{29}Si	5.9×10^{-5}	2.26×10^{-4}	4.78×10^{-4}	8.24×10^{-4}	1.61×10^{-3}	2.46×10^{-3}	4.53×10^{-3}
^{30}Si	3.23×10^{-5}	7.15×10^{-5}	6.93×10^{-4}	1.58×10^{-3}	3.44×10^{-3}	5.58×10^{-3}	1.9×10^{-2}
^{31}P	8.39×10^{-5}	5.42×10^{-5}	2.6×10^{-4}	3.54×10^{-4}	5.97×10^{-4}	8.3×10^{-4}	1.11×10^{-3}
^{32}S	5.10×10^{-2}	4.92×10^{-2}	4.96×10^{-2}	4.90×10^{-2}	4.56×10^{-2}	4.16×10^{-2}	3.41×10^{-2}
^{33}S	4.7×10^{-5}	1.6×10^{-4}	2.24×10^{-4}	3.8×10^{-4}	4.10×10^{-4}	4.67×10^{-4}	4.98×10^{-4}
^{34}S	3.93×10^{-6}	1.4×10^{-4}	8.85×10^{-4}	1.97×10^{-3}	4.35×10^{-3}	6.78×10^{-3}	1.9×10^{-2}
^{36}S	2.78×10^{-11}	1.31×10^{-9}	3.34×10^{-8}	1.82×10^{-7}	1.73×10^{-6}	6.42×10^{-6}	2.23×10^{-5}
^{35}Cl	7.90×10^{-6}	1.78×10^{-5}	7.8×10^{-5}	1.30×10^{-4}	2.12×10^{-4}	2.35×10^{-4}	1.91×10^{-4}
^{37}Cl	3.6×10^{-6}	8.88×10^{-6}	1.73×10^{-5}	2.37×10^{-5}	3.21×10^{-5}	3.67×10^{-5}	3.95×10^{-5}
^{36}Ar	1.2×10^{-2}	8.94×10^{-3}	8.21×10^{-3}	7.52×10^{-3}	6.22×10^{-3}	5.18×10^{-3}	3.69×10^{-3}
^{38}Ar	1.6×10^{-6}	6.0×10^{-5}	4.77×10^{-4}	1.4×10^{-3}	2.19×10^{-3}	3.21×10^{-3}	4.63×10^{-3}
^{40}Ar	4.66×10^{-12}	1.12×10^{-11}	3.25×10^{-10}	3.4×10^{-9}	3.91×10^{-8}	1.46×10^{-7}	4.31×10^{-7}
^{39}K	7.10×10^{-6}	2.5×10^{-5}	5.70×10^{-5}	8.52×10^{-5}	1.15×10^{-4}	1.21×10^{-4}	1.3×10^{-4}
^{40}K	5.89×10^{-10}	1.90×10^{-9}	1.41×10^{-8}	5.41×10^{-8}	1.58×10^{-7}	1.83×10^{-7}	9.4×10^{-8}
^{41}K	1.20×10^{-6}	2.76×10^{-6}	4.41×10^{-6}	5.66×10^{-6}	6.76×10^{-6}	6.64×10^{-6}	5.36×10^{-6}
^{40}Ca	1.6×10^{-2}	8.91×10^{-3}	7.69×10^{-3}	6.87×10^{-3}	5.71×10^{-3}	4.96×10^{-3}	3.97×10^{-3}
^{42}Ca	2.10×10^{-6}	3.60×10^{-6}	1.63×10^{-5}	3.39×10^{-5}	6.60×10^{-5}	8.89×10^{-5}	1.5×10^{-4}
^{43}Ca	1.36×10^{-5}	1.37×10^{-5}	1.39×10^{-5}	1.39×10^{-5}	1.38×10^{-5}	1.38×10^{-5}	1.39×10^{-5}
^{44}Ca	6.2×10^{-4}	6.1×10^{-4}	6.0×10^{-4}	5.99×10^{-4}	6.0×10^{-4}	5.97×10^{-4}	5.97×10^{-4}
^{46}Ca	1.84×10^{-16}	4.41×10^{-15}	2.86×10^{-12}	6.92×10^{-11}	9.5×10^{-10}	2.14×10^{-9}	2.49×10^{-9}
^{48}Ca	4.80×10^{-23}	3.60×10^{-21}	5.54×10^{-18}	5.8×10^{-16}	6.53×10^{-14}	5.43×10^{-13}	3.19×10^{-12}
^{45}Sc	6.14×10^{-7}	6.72×10^{-7}	7.34×10^{-7}	7.81×10^{-7}	8.9×10^{-7}	7.97×10^{-7}	7.65×10^{-7}
^{46}Ti	9.74×10^{-7}	1.64×10^{-6}	7.69×10^{-6}	1.53×10^{-5}	2.72×10^{-5}	3.35×10^{-5}	3.33×10^{-5}
^{47}Ti	6.53×10^{-5}	6.54×10^{-5}	6.57×10^{-5}	6.58×10^{-5}	6.61×10^{-5}	6.64×10^{-5}	6.67×10^{-5}
^{48}Ti	2.68×10^{-3}	2.65×10^{-3}	2.63×10^{-3}	2.61×10^{-3}	2.59×10^{-3}	2.59×10^{-3}	2.58×10^{-3}
^{49}Ti	2.38×10^{-5}	2.64×10^{-5}	2.76×10^{-5}	2.83×10^{-5}	2.87×10^{-5}	2.93×10^{-5}	3.3×10^{-5}
^{50}Ti	1.3×10^{-13}	2.70×10^{-13}	9.62×10^{-11}	7.12×10^{-10}	1.93×10^{-9}	2.48×10^{-9}	6.33×10^{-9}
^{50}V	4.85×10^{-10}	4.94×10^{-10}	1.39×10^{-9}	3.86×10^{-9}	6.34×10^{-9}	1.9×10^{-8}	3.20×10^{-8}
^{51}V	2.67×10^{-4}	2.69×10^{-4}	2.76×10^{-4}	2.81×10^{-4}	2.86×10^{-4}	2.95×10^{-4}	3.12×10^{-4}

Table 11. *cont'd* of Table 10.

Z ($Z_\odot$)	0	0.1	0.5	1	2	3	5
^{50}Cr	1.69×10^{-5}	2.32×10^{-5}	5.98×10^{-5}	1.9×10^{-4}	2.10×10^{-4}	2.80×10^{-4}	3.48×10^{-4}
^{52}Cr	3.34×10^{-3}	3.19×10^{-3}	2.95×10^{-3}	2.80×10^{-3}	2.73×10^{-3}	2.93×10^{-3}	3.83×10^{-3}
^{53}Cr	7.22×10^{-5}	1.6×10^{-4}	1.34×10^{-4}	1.56×10^{-4}	2.3×10^{-4}	2.78×10^{-4}	4.48×10^{-4}
^{54}Cr	2.68×10^{-8}	2.70×10^{-8}	3.58×10^{-8}	6.70×10^{-8}	2.54×10^{-7}	7.23×10^{-7}	2.23×10^{-6}
^{55}Mn	3.56×10^{-4}	4.89×10^{-4}	7.29×10^{-4}	9.15×10^{-4}	1.39×10^{-3}	2.41×10^{-3}	6.72×10^{-3}
^{54}Fe	1.97×10^{-4}	6.46×10^{-4}	2.70×10^{-3}	5.20×10^{-3}	9.87×10^{-3}	1.49×10^{-2}	3.68×10^{-2}
^{56}Fe	7.25×10^{-1}	7.21×10^{-1}	7.4×10^{-1}	6.84×10^{-1}	6.45×10^{-1}	6.8×10^{-1}	5.32×10^{-1}
^{57}Fe	1.16×10^{-2}	1.26×10^{-2}	1.57×10^{-2}	1.90×10^{-2}	2.41×10^{-2}	2.77×10^{-2}	3.12×10^{-2}
^{58}Fe	3.70×10^{-8}	3.72×10^{-8}	3.99×10^{-8}	4.83×10^{-8}	8.49×10^{-8}	1.46×10^{-7}	2.97×10^{-7}
^{60}Fe	1.45×10^{-19}	1.52×10^{-19}	4.18×10^{-19}	1.11×10^{-18}	2.0×10^{-18}	1.94×10^{-18}	1.24×10^{-17}
^{59}Co	6.73×10^{-5}	1.25×10^{-4}	4.59×10^{-4}	6.17×10^{-4}	7.33×10^{-4}	6.72×10^{-4}	4.46×10^{-4}
^{58}Ni	9.17×10^{-4}	1.82×10^{-3}	1.41×10^{-2}	3.6×10^{-2}	6.46×10^{-2}	9.80×10^{-2}	1.51×10^{-1}
^{60}Ni	8.66×10^{-3}	8.96×10^{-3}	7.64×10^{-3}	6.41×10^{-3}	4.44×10^{-3}	2.89×10^{-3}	1.22×10^{-3}
^{61}Ni	1.90×10^{-4}	2.5×10^{-4}	2.32×10^{-4}	2.48×10^{-4}	2.37×10^{-4}	1.98×10^{-4}	1.22×10^{-4}
^{62}Ni	1.7×10^{-4}	2.96×10^{-4}	1.7×10^{-3}	1.83×10^{-3}	2.70×10^{-3}	2.83×10^{-3}	2.20×10^{-3}
^{64}Ni	7.90×10^{-13}	9.44×10^{-13}	9.52×10^{-13}	8.3×10^{-13}	7.94×10^{-13}	8.17×10^{-13}	8.46×10^{-13}
^{63}Cu	1.90×10^{-6}	3.14×10^{-6}	1.85×10^{-6}	2.24×10^{-6}	2.89×10^{-6}	3.20×10^{-6}	3.9×10^{-6}
^{65}Cu	3.34×10^{-6}	3.42×10^{-6}	3.47×10^{-6}	3.49×10^{-6}	3.35×10^{-6}	3.22×10^{-6}	2.89×10^{-6}
^{64}Zn	1.30×10^{-4}	8.61×10^{-5}	1.68×10^{-5}	1.30×10^{-5}	9.70×10^{-6}	7.81×10^{-6}	6.14×10^{-6}
^{66}Zn	7.96×10^{-6}	9.62×10^{-6}	1.58×10^{-5}	2.15×10^{-5}	2.67×10^{-5}	2.71×10^{-5}	2.33×10^{-5}
^{67}Zn	1.21×10^{-6}	1.20×10^{-6}	1.20×10^{-6}	1.21×10^{-6}	1.21×10^{-6}	1.24×10^{-6}	1.24×10^{-6}
^{68}Zn	8.43×10^{-7}	5.39×10^{-7}	4.9×10^{-7}	4.7×10^{-7}	4.7×10^{-7}	4.17×10^{-7}	4.22×10^{-7}
^{70}Zn	5.14×10^{-17}	5.52×10^{-17}	4.40×10^{-15}	5.22×10^{-17}	5.14×10^{-17}	5.7×10^{-17}	5.6×10^{-17}

Table 12. The nucleosynthesis yields for radioactive isotopes of the benchmark models. Masses are in units of solar mass.

Z ($Z_\odot$)	0	0.1	0.5	1	2	3	5
^{22}Na	9.63×10^{-9}	8.92×10^{-9}	1.40×10^{-8}	1.56×10^{-8}	1.24×10^{-8}	9.89×10^{-9}	7.6×10^{-9}
^{26}Al	2.54×10^{-6}	5.47×10^{-6}	8.71×10^{-6}	8.12×10^{-6}	5.7×10^{-6}	3.16×10^{-6}	1.44×10^{-6}
^{39}Ar	9.85×10^{-12}	1.14×10^{-10}	1.75×10^{-9}	8.69×10^{-9}	4.57×10^{-8}	9.15×10^{-8}	1.3×10^{-7}
^{40}K	5.92×10^{-10}	1.91×10^{-9}	1.42×10^{-8}	5.44×10^{-8}	1.59×10^{-7}	1.84×10^{-7}	9.9×10^{-8}
^{41}Ca	1.5×10^{-6}	2.59×10^{-6}	4.44×10^{-6}	5.71×10^{-6}	6.75×10^{-6}	6.65×10^{-6}	5.31×10^{-6}
^{44}Ti	6.3×10^{-4}	6.1×10^{-4}	6.0×10^{-4}	5.99×10^{-4}	5.97×10^{-4}	5.97×10^{-4}	5.95×10^{-4}
^{48}V	1.11×10^{-6}	1.12×10^{-6}	1.13×10^{-6}	1.15×10^{-6}	1.19×10^{-6}	1.21×10^{-6}	1.20×10^{-6}
^{49}V	8.16×10^{-8}	8.42×10^{-8}	1.21×10^{-7}	1.85×10^{-7}	3.38×10^{-7}	5.81×10^{-7}	1.12×10^{-6}
^{53}Mn	2.72×10^{-6}	2.84×10^{-6}	5.18×10^{-6}	1.15×10^{-5}	4.51×10^{-5}	9.98×10^{-5}	1.83×10^{-4}
^{60}Fe	2.14×10^{-18}	2.26×10^{-18}	5.98×10^{-18}	1.62×10^{-17}	3.0×10^{-17}	2.78×10^{-17}	1.78×10^{-16}
^{56}Co	1.56×10^{-5}	1.59×10^{-5}	1.67×10^{-5}	1.79×10^{-5}	2.4×10^{-5}	2.57×10^{-5}	5.77×10^{-5}
^{57}Co	5.43×10^{-6}	5.56×10^{-6}	6.93×10^{-6}	9.87×10^{-6}	2.4×10^{-5}	3.2×10^{-5}	4.37×10^{-5}
^{60}Co	5.85×10^{-13}	5.93×10^{-13}	6.10×10^{-13}	6.59×10^{-13}	1.7×10^{-12}	2.25×10^{-12}	8.29×10^{-12}
^{56}Ni	7.25×10^{-1}	7.21×10^{-1}	7.4×10^{-1}	6.84×10^{-1}	6.45×10^{-1}	6.6×10^{-1}	5.29×10^{-1}
^{57}Ni	1.16×10^{-2}	1.26×10^{-2}	1.57×10^{-2}	1.90×10^{-2}	2.41×10^{-2}	2.76×10^{-2}	3.11×10^{-2}
^{59}Ni	3.31×10^{-6}	3.36×10^{-6}	3.80×10^{-6}	4.77×10^{-6}	8.56×10^{-6}	1.96×10^{-5}	6.77×10^{-5}
^{63}Ni	2.55×10^{-14}	5.3×10^{-14}	2.88×10^{-14}	2.62×10^{-14}	2.95×10^{-14}	4.33×10^{-14}	1.26×10^{-13}

Table 13. The nucleosynthesis yields for the stable isotopes of the benchmark model with a spherical He detonation as a trigger based on Model 100-050-2-S50 at solar metallicity. Masses are in units of solar mass.

Z ($Z_\odot$)	0	0.1	0.5	1	2	3	5
^{12}C	1.18×10^{-3}	1.17×10^{-3}	1.16×10^{-3}	1.15×10^{-3}	1.13×10^{-3}	1.13×10^{-3}	1.11×10^{-3}
^{13}C	1.4×10^{-10}	8.4×10^{-11}	8.87×10^{-10}	3.2×10^{-9}	1.21×10^{-8}	3.70×10^{-8}	1.9×10^{-7}
^{14}N	3.94×10^{-9}	1.76×10^{-9}	9.2×10^{-9}	1.81×10^{-8}	7.5×10^{-8}	2.52×10^{-7}	6.87×10^{-7}
^{15}N	1.0×10^{-6}	4.93×10^{-9}	5.68×10^{-10}	2.13×10^{-10}	3.20×10^{-10}	1.42×10^{-9}	5.54×10^{-9}
^{16}O	5.90×10^{-2}	6.34×10^{-2}	6.55×10^{-2}	6.64×10^{-2}	6.68×10^{-2}	6.64×10^{-2}	6.48×10^{-2}
^{17}O	9.61×10^{-11}	2.70×10^{-10}	4.18×10^{-9}	1.8×10^{-8}	2.3×10^{-8}	2.43×10^{-8}	2.52×10^{-8}
^{18}O	3.29×10^{-12}	8.33×10^{-12}	6.40×10^{-11}	9.43×10^{-11}	4.35×10^{-10}	2.21×10^{-9}	8.97×10^{-9}
^{19}F	5.92×10^{-11}	7.31×10^{-12}	7.99×10^{-12}	2.39×10^{-11}	7.87×10^{-11}	1.70×10^{-10}	2.95×10^{-10}
^{20}Ne	1.30×10^{-3}	1.27×10^{-3}	1.21×10^{-3}	1.15×10^{-3}	1.8×10^{-3}	1.4×10^{-3}	9.83×10^{-4}
^{21}Ne	2.97×10^{-9}	5.41×10^{-9}	5.8×10^{-8}	1.57×10^{-7}	5.91×10^{-7}	1.56×10^{-6}	4.5×10^{-6}
^{22}Ne	5.70×10^{-9}	3.38×10^{-9}	5.77×10^{-9}	9.25×10^{-9}	6.35×10^{-7}	6.45×10^{-6}	4.12×10^{-5}
^{23}Na	3.59×10^{-6}	3.86×10^{-6}	5.77×10^{-6}	8.39×10^{-6}	1.58×10^{-5}	2.80×10^{-5}	5.31×10^{-5}
^{24}Mg	3.69×10^{-3}	3.10×10^{-3}	1.84×10^{-3}	1.28×10^{-3}	8.70×10^{-4}	7.14×10^{-4}	6.29×10^{-4}
^{25}Mg	1.9×10^{-7}	8.53×10^{-7}	6.20×10^{-6}	1.45×10^{-5}	3.43×10^{-5}	5.87×10^{-5}	1.11×10^{-4}
^{26}Mg	1.26×10^{-6}	3.45×10^{-6}	1.35×10^{-5}	2.89×10^{-5}	6.82×10^{-5}	1.13×10^{-4}	2.74×10^{-4}
^{26}Al	2.60×10^{-29}	2.60×10^{-29}	2.60×10^{-29}	2.60×10^{-29}	2.60×10^{-29}	2.60×10^{-29}	3.57×10^{-11}
^{27}Al	2.45×10^{-5}	4.76×10^{-5}	9.84×10^{-5}	1.14×10^{-4}	1.23×10^{-4}	1.33×10^{-4}	1.72×10^{-4}
^{28}Si	1.14×10^{-1}	1.18×10^{-1}	1.22×10^{-1}	1.25×10^{-1}	1.26×10^{-1}	1.26×10^{-1}	1.22×10^{-1}
^{29}Si	2.22×10^{-5}	9.34×10^{-5}	1.71×10^{-4}	2.67×10^{-4}	4.74×10^{-4}	7.4×10^{-4}	1.24×10^{-3}
^{30}Si	1.66×10^{-5}	2.23×10^{-5}	1.69×10^{-4}	3.79×10^{-4}	9.29×10^{-4}	1.73×10^{-3}	4.50×10^{-3}
^{31}P	4.4×10^{-5}	2.88×10^{-5}	9.33×10^{-5}	1.53×10^{-4}	2.64×10^{-4}	3.74×10^{-4}	5.61×10^{-4}
^{32}S	7.11×10^{-2}	6.89×10^{-2}	6.81×10^{-2}	6.56×10^{-2}	5.89×10^{-2}	5.28×10^{-2}	4.28×10^{-2}
^{33}S	1.64×10^{-5}	7.31×10^{-5}	1.39×10^{-4}	1.89×10^{-4}	2.65×10^{-4}	3.19×10^{-4}	3.71×10^{-4}
^{34}S	4.3×10^{-6}	1.15×10^{-4}	8.82×10^{-4}	1.91×10^{-3}	4.13×10^{-3}	6.58×10^{-3}	1.14×10^{-2}
^{36}S	4.11×10^{-12}	5.80×10^{-10}	9.34×10^{-9}	6.35×10^{-8}	6.23×10^{-7}	1.81×10^{-6}	4.76×10^{-6}
^{35}Cl	8.25×10^{-6}	1.80×10^{-5}	6.35×10^{-5}	1.4×10^{-4}	1.57×10^{-4}	1.75×10^{-4}	1.59×10^{-4}
^{37}Cl	2.23×10^{-6}	9.59×10^{-6}	1.85×10^{-5}	2.51×10^{-5}	3.32×10^{-5}	3.58×10^{-5}	3.39×10^{-5}
^{36}Ar	1.55×10^{-2}	1.41×10^{-2}	1.28×10^{-2}	1.15×10^{-2}	9.49×10^{-3}	8.2×10^{-3}	6.1×10^{-3}
^{38}Ar	6.21×10^{-7}	8.62×10^{-5}	6.28×10^{-4}	1.34×10^{-3}	2.70×10^{-3}	3.87×10^{-3}	5.30×10^{-3}
^{40}Ar	7.66×10^{-14}	4.26×10^{-12}	1.64×10^{-10}	1.71×10^{-9}	1.62×10^{-8}	4.42×10^{-8}	1.14×10^{-7}
^{39}K	5.8×10^{-6}	2.17×10^{-5}	6.27×10^{-5}	9.25×10^{-5}	1.22×10^{-4}	1.24×10^{-4}	1.2×10^{-4}
^{40}K	4.81×10^{-11}	1.58×10^{-9}	1.21×10^{-8}	3.84×10^{-8}	8.59×10^{-8}	9.1×10^{-8}	5.60×10^{-8}
^{41}K	7.4×10^{-7}	2.71×10^{-6}	4.54×10^{-6}	5.64×10^{-6}	6.64×10^{-6}	6.37×10^{-6}	4.80×10^{-6}
^{40}Ca	1.61×10^{-2}	1.40×10^{-2}	1.19×10^{-2}	1.4×10^{-2}	8.49×10^{-3}	7.33×10^{-3}	5.81×10^{-3}
^{42}Ca	3.55×10^{-7}	2.58×10^{-6}	1.97×10^{-5}	4.24×10^{-5}	7.93×10^{-5}	1.1×10^{-4}	1.10×10^{-4}
^{43}Ca	1.31×10^{-5}	1.36×10^{-5}	1.39×10^{-5}	1.38×10^{-5}	1.36×10^{-5}	1.36×10^{-5}	1.37×10^{-5}
^{44}Ca	2.78×10^{-4}	2.76×10^{-4}	2.65×10^{-4}	2.63×10^{-4}	2.61×10^{-4}	2.60×10^{-4}	2.59×10^{-4}
^{46}Ca	3.99×10^{-20}	8.14×10^{-16}	1.79×10^{-12}	4.90×10^{-11}	5.11×10^{-10}	1.13×10^{-9}	1.43×10^{-9}
^{48}Ca	2.1×10^{-25}	1.61×10^{-22}	9.58×10^{-18}	9.28×10^{-16}	6.1×10^{-14}	3.6×10^{-13}	1.10×10^{-12}
^{45}Sc	2.8×10^{-7}	2.72×10^{-7}	3.35×10^{-7}	3.77×10^{-7}	4.21×10^{-7}	4.18×10^{-7}	3.91×10^{-7}
^{46}Ti	8.53×10^{-7}	1.70×10^{-6}	9.45×10^{-6}	1.85×10^{-5}	3.9×10^{-5}	3.61×10^{-5}	3.42×10^{-5}
^{47}Ti	2.13×10^{-5}	2.18×10^{-5}	2.24×10^{-5}	2.27×10^{-5}	2.31×10^{-5}	2.33×10^{-5}	2.35×10^{-5}
^{48}Ti	8.12×10^{-4}	7.82×10^{-4}	7.37×10^{-4}	7.8×10^{-4}	6.76×10^{-4}	6.58×10^{-4}	6.33×10^{-4}
^{49}Ti	4.75×10^{-6}	1.2×10^{-5}	1.30×10^{-5}	1.47×10^{-5}	1.56×10^{-5}	1.66×10^{-5}	1.77×10^{-5}
^{50}Ti	5.52×10^{-16}	1.58×10^{-13}	5.96×10^{-11}	6.7×10^{-10}	2.35×10^{-9}	3.70×10^{-9}	1.7×10^{-8}
^{50}V	1.8×10^{-11}	2.22×10^{-11}	8.63×10^{-10}	3.68×10^{-9}	8.7×10^{-9}	1.46×10^{-8}	4.14×10^{-8}
^{51}V	5.15×10^{-5}	5.47×10^{-5}	6.79×10^{-5}	7.62×10^{-5}	8.55×10^{-5}	9.87×10^{-5}	1.21×10^{-4}

Table 14. *cont′d* of Table 13.

Z ($Z_\odot$)	0	0.1	0.5	1	2	3	5
^{50}Cr	5.56×10^{-6}	1.34×10^{-5}	6.64×10^{-5}	1.41×10^{-4}	3.5×10^{-4}	4.30×10^{-4}	5.91×10^{-4}
^{52}Cr	4.11×10^{-3}	3.86×10^{-3}	3.30×10^{-3}	2.94×10^{-3}	2.65×10^{-3}	2.77×10^{-3}	3.68×10^{-3}
^{53}Cr	4.72×10^{-5}	1.21×10^{-4}	1.78×10^{-4}	2.14×10^{-4}	2.77×10^{-4}	3.74×10^{-4}	5.67×10^{-4}
^{54}Cr	9.21×10^{-10}	1.18×10^{-9}	1.14×10^{-8}	4.40×10^{-8}	2.43×10^{-7}	8.6×10^{-7}	2.68×10^{-6}
^{55}Mn	3.9×10^{-4}	5.59×10^{-4}	1.3×10^{-3}	1.32×10^{-3}	1.87×10^{-3}	3.6×10^{-3}	6.30×10^{-3}
^{54}Fe	1.10×10^{-4}	8.14×10^{-4}	4.37×10^{-3}	8.69×10^{-3}	1.66×10^{-2}	2.48×10^{-2}	4.79×10^{-2}
^{56}Fe	6.43×10^{-1}	6.38×10^{-1}	6.20×10^{-1}	6.0×10^{-1}	5.65×10^{-1}	5.32×10^{-1}	4.67×10^{-1}
^{57}Fe	9.74×10^{-3}	1.6×10^{-2}	1.32×10^{-2}	1.60×10^{-2}	2.2×10^{-2}	2.32×10^{-2}	2.62×10^{-2}
^{58}Fe	1.70×10^{-9}	1.86×10^{-9}	5.14×10^{-9}	1.36×10^{-8}	5.25×10^{-8}	1.23×10^{-7}	3.1×10^{-7}
^{60}Fe	1.39×10^{-23}	1.81×10^{-21}	7.0×10^{-19}	3.4×10^{-18}	4.58×10^{-18}	2.90×10^{-18}	1.5×10^{-17}
^{59}Co	6.56×10^{-5}	9.1×10^{-5}	4.9×10^{-4}	5.27×10^{-4}	6.33×10^{-4}	6.12×10^{-4}	5.29×10^{-4}
^{58}Ni	9.62×10^{-4}	1.18×10^{-3}	1.11×10^{-2}	2.50×10^{-2}	5.35×10^{-2}	8.7×10^{-2}	1.27×10^{-1}
^{60}Ni	7.71×10^{-3}	8.14×10^{-3}	7.14×10^{-3}	6.13×10^{-3}	4.50×10^{-3}	3.27×10^{-3}	1.81×10^{-3}
^{61}Ni	2.18×10^{-4}	2.33×10^{-4}	2.62×10^{-4}	2.78×10^{-4}	2.79×10^{-4}	2.61×10^{-4}	2.11×10^{-4}
^{62}Ni	8.49×10^{-5}	2.15×10^{-4}	9.81×10^{-4}	1.72×10^{-3}	2.72×10^{-3}	3.17×10^{-3}	3.24×10^{-3}
^{64}Ni	4.14×10^{-14}	3.79×10^{-14}	4.71×10^{-14}	4.59×10^{-14}	1.80×10^{-11}	5.11×10^{-14}	7.60×10^{-14}
^{63}Cu	1.72×10^{-6}	3.69×10^{-6}	2.13×10^{-6}	2.50×10^{-6}	3.23×10^{-6}	3.76×10^{-6}	4.34×10^{-6}
^{65}Cu	7.54×10^{-6}	7.68×10^{-6}	7.54×10^{-6}	7.61×10^{-6}	7.60×10^{-6}	7.55×10^{-6}	7.25×10^{-6}
^{64}Zn	1.44×10^{-4}	1.31×10^{-4}	3.10×10^{-5}	2.70×10^{-5}	2.38×10^{-5}	2.20×10^{-5}	2.0×10^{-5}
^{66}Zn	8.34×10^{-6}	1.1×10^{-5}	1.70×10^{-5}	2.41×10^{-5}	3.35×10^{-5}	3.76×10^{-5}	3.80×10^{-5}
^{67}Zn	3.40×10^{-7}	3.33×10^{-7}	3.34×10^{-7}	3.41×10^{-7}	3.53×10^{-7}	3.62×10^{-7}	3.71×10^{-7}
^{68}Zn	1.4×10^{-6}	6.8×10^{-7}	3.75×10^{-7}	3.71×10^{-7}	3.71×10^{-7}	3.72×10^{-7}	3.87×10^{-7}
^{70}Zn	1.62×10^{-18}	1.48×10^{-18}	1.99×10^{-18}	1.97×10^{-18}	1.12×10^{-16}	1.64×10^{-18}	1.62×10^{-18}

Table 15. Similar to 13 but for the radioactive isotopes. Masses are in units of solar mass.

Z ($Z_\odot$)	0	0.1	0.5	1	2	3	5
^{22}Na	2.93×10^{-9}	3.22×10^{-9}	4.6×10^{-9}	3.74×10^{-9}	2.87×10^{-9}	2.42×10^{-9}	2.0×10^{-9}
^{26}Al	8.57×10^{-7}	1.74×10^{-6}	2.12×10^{-6}	1.70×10^{-6}	1.4×10^{-6}	7.15×10^{-7}	4.1×10^{-7}
^{39}Ar	4.11×10^{-13}	1.11×10^{-10}	1.66×10^{-9}	7.27×10^{-9}	3.3×10^{-8}	5.13×10^{-8}	5.39×10^{-8}
^{40}K	4.83×10^{-11}	1.59×10^{-9}	1.22×10^{-8}	3.86×10^{-8}	8.64×10^{-8}	9.6×10^{-8}	5.63×10^{-8}
^{41}Ca	6.17×10^{-7}	2.38×10^{-6}	4.36×10^{-6}	5.66×10^{-6}	6.62×10^{-6}	6.34×10^{-6}	4.76×10^{-6}
^{44}Ti	2.70×10^{-4}	2.68×10^{-4}	2.66×10^{-4}	2.64×10^{-4}	2.62×10^{-4}	2.61×10^{-4}	2.59×10^{-4}
^{48}V	1.45×10^{-7}	1.47×10^{-7}	1.70×10^{-7}	1.96×10^{-7}	2.34×10^{-7}	2.49×10^{-7}	2.36×10^{-7}
^{49}V	8.72×10^{-9}	1.18×10^{-8}	6.3×10^{-8}	1.54×10^{-7}	3.54×10^{-7}	6.54×10^{-7}	1.31×10^{-6}
^{53}Mn	3.8×10^{-7}	4.27×10^{-7}	2.73×10^{-6}	9.5×10^{-6}	4.91×10^{-5}	1.22×10^{-4}	2.50×10^{-4}
^{60}Fe	2.23×10^{-22}	2.90×10^{-20}	1.14×10^{-17}	4.59×10^{-17}	6.65×10^{-17}	4.22×10^{-17}	1.48×10^{-16}
^{56}Co	5.62×10^{-6}	5.89×10^{-6}	7.25×10^{-6}	8.93×10^{-6}	1.21×10^{-5}	1.85×10^{-5}	4.20×10^{-5}
^{57}Co	1.10×10^{-6}	1.23×10^{-6}	2.61×10^{-6}	5.62×10^{-6}	1.86×10^{-5}	3.17×10^{-5}	5.16×10^{-5}
^{60}Co	2.31×10^{-15}	7.99×10^{-15}	6.58×10^{-14}	1.17×10^{-13}	5.39×10^{-13}	1.67×10^{-12}	7.29×10^{-12}
^{56}Ni	6.42×10^{-1}	6.38×10^{-1}	6.20×10^{-1}	6.0×10^{-1}	5.64×10^{-1}	5.31×10^{-1}	4.64×10^{-1}
^{57}Ni	9.74×10^{-3}	1.6×10^{-2}	1.32×10^{-2}	1.60×10^{-2}	2.2×10^{-2}	2.31×10^{-2}	2.62×10^{-2}
^{59}Ni	1.59×10^{-6}	1.61×10^{-6}	2.5×10^{-6}	2.89×10^{-6}	6.89×10^{-6}	1.61×10^{-5}	4.48×10^{-5}
^{63}Ni	5.94×10^{-16}	9.34×10^{-16}	3.30×10^{-15}	2.12×10^{-15}	4.10×10^{-13}	1.92×10^{-14}	9.76×10^{-14}

Table 16. The nucleosynthesis yields for stable isotopes from the models using one He detonation bubble as the initial configuration. The minimum He envelope mass is used for each choice of progenitor mass. All models are of solar metallicity and masses are in units of solar mass.

M	0.90	0.95	1.00	1.05	1.10	1.15	1.20
$M_{\rm He}$	0.15	0.15	0.10	0.10	0.10	0.10	0.05
^{12}C	1.78×10^{-2}	7.5×10^{-3}	8.85×10^{-3}	1.26×10^{-2}	3.35×10^{-3}	1.6×10^{-4}	2.10×10^{-3}
^{13}C	6.99×10^{-8}	2.73×10^{-9}	3.87×10^{-9}	1.84×10^{-8}	1.25×10^{-9}	4.83×10^{-11}	5.8×10^{-10}
^{14}N	1.50×10^{-6}	7.88×10^{-8}	9.0×10^{-8}	4.92×10^{-7}	3.80×10^{-8}	8.42×10^{-10}	1.41×10^{-8}
^{15}N	8.65×10^{-9}	1.83×10^{-9}	2.69×10^{-9}	3.45×10^{-9}	1.8×10^{-9}	1.13×10^{-10}	7.37×10^{-10}
^{16}O	2.63×10^{-1}	2.19×10^{-1}	2.35×10^{-1}	1.85×10^{-1}	1.17×10^{-1}	5.23×10^{-2}	6.54×10^{-2}
^{17}O	3.23×10^{-7}	4.35×10^{-8}	4.80×10^{-8}	1.68×10^{-7}	2.8×10^{-8}	2.95×10^{-10}	7.14×10^{-9}
^{18}O	4.35×10^{-9}	5.86×10^{-10}	6.10×10^{-10}	1.89×10^{-9}	3.4×10^{-10}	6.56×10^{-12}	1.29×10^{-10}
^{19}F	4.10×10^{-10}	6.42×10^{-11}	8.49×10^{-11}	1.79×10^{-10}	3.28×10^{-11}	1.94×10^{-12}	1.80×10^{-11}
^{20}Ne	2.65×10^{-2}	8.46×10^{-3}	1.4×10^{-2}	9.19×10^{-3}	4.0×10^{-3}	6.90×10^{-4}	2.91×10^{-3}
^{21}Ne	2.48×10^{-6}	4.54×10^{-7}	5.79×10^{-7}	1.3×10^{-6}	2.17×10^{-7}	2.1×10^{-8}	1.32×10^{-7}
^{22}Ne	3.40×10^{-4}	2.0×10^{-4}	2.42×10^{-4}	3.53×10^{-4}	9.45×10^{-5}	2.66×10^{-9}	5.62×10^{-5}
^{23}Na	1.18×10^{-4}	3.13×10^{-5}	4.7×10^{-5}	4.36×10^{-5}	1.47×10^{-5}	2.20×10^{-6}	1.8×10^{-5}
^{24}Mg	3.7×10^{-2}	2.15×10^{-2}	2.38×10^{-2}	1.62×10^{-2}	8.26×10^{-3}	3.32×10^{-3}	4.97×10^{-3}
^{25}Mg	2.63×10^{-4}	7.96×10^{-5}	1.2×10^{-4}	1.1×10^{-4}	3.89×10^{-5}	7.71×10^{-6}	2.51×10^{-5}
^{26}Mg	3.97×10^{-4}	1.20×10^{-4}	1.47×10^{-4}	1.59×10^{-4}	5.60×10^{-5}	9.35×10^{-6}	3.69×10^{-5}
^{26}Al	7.61×10^{-9}	2.47×10^{-29}	3.75×10^{-28}	2.73×10^{-29}	2.86×10^{-29}	2.99×10^{-29}	4.48×10^{-28}
^{27}Al	2.67×10^{-3}	1.68×10^{-3}	1.95×10^{-3}	1.30×10^{-3}	6.50×10^{-4}	2.53×10^{-4}	3.93×10^{-4}
^{28}Si	1.90×10^{-1}	1.43×10^{-1}	1.53×10^{-1}	1.27×10^{-1}	1.35×10^{-1}	9.51×10^{-2}	9.20×10^{-2}
^{29}Si	2.83×10^{-3}	1.87×10^{-3}	2.9×10^{-3}	1.61×10^{-3}	8.76×10^{-4}	3.44×10^{-4}	5.18×10^{-4}
^{30}Si	4.62×10^{-3}	4.1×10^{-3}	4.36×10^{-3}	3.0×10^{-3}	1.62×10^{-3}	6.99×10^{-4}	9.30×10^{-4}
^{31}P	9.82×10^{-4}	7.65×10^{-4}	8.70×10^{-4}	6.18×10^{-4}	3.97×10^{-4}	1.78×10^{-4}	2.23×10^{-4}
^{32}S	7.66×10^{-2}	5.15×10^{-2}	5.63×10^{-2}	4.93×10^{-2}	6.8×10^{-2}	4.57×10^{-2}	4.25×10^{-2}
^{33}S	7.26×10^{-4}	6.22×10^{-4}	6.84×10^{-4}	5.4×10^{-4}	3.72×10^{-4}	1.82×10^{-4}	2.15×10^{-4}
^{34}S	3.49×10^{-3}	3.43×10^{-3}	3.42×10^{-3}	3.7×10^{-3}	2.62×10^{-3}	1.34×10^{-3}	1.43×10^{-3}
^{36}S	5.53×10^{-7}	4.52×10^{-7}	5.1×10^{-7}	3.46×10^{-7}	1.77×10^{-7}	6.99×10^{-8}	1.5×10^{-7}
^{35}Cl	3.69×10^{-4}	1.64×10^{-4}	1.92×10^{-4}	1.42×10^{-4}	1.51×10^{-4}	7.4×10^{-5}	8.76×10^{-5}
^{37}Cl	4.17×10^{-5}	2.85×10^{-5}	3.16×10^{-5}	2.41×10^{-5}	3.26×10^{-5}	1.95×10^{-5}	1.98×10^{-5}
^{36}Ar	1.7×10^{-2}	6.82×10^{-3}	7.39×10^{-3}	7.10×10^{-3}	9.73×10^{-3}	7.81×10^{-3}	6.95×10^{-3}
^{38}Ar	1.70×10^{-3}	1.6×10^{-3}	1.13×10^{-3}	9.58×10^{-4}	1.32×10^{-3}	7.79×10^{-4}	7.89×10^{-4}
^{40}Ar	9.42×10^{-9}	6.9×10^{-9}	7.36×10^{-9}	4.63×10^{-9}	3.35×10^{-9}	1.3×10^{-9}	1.60×10^{-9}
^{39}K	1.46×10^{-4}	8.23×10^{-5}	9.61×10^{-5}	6.56×10^{-5}	1.7×10^{-4}	7.4×10^{-5}	6.75×10^{-5}
^{40}K	1.72×10^{-7}	6.69×10^{-8}	9.10×10^{-8}	5.43×10^{-8}	1.23×10^{-7}	2.30×10^{-8}	2.92×10^{-8}
^{41}K	1.0×10^{-5}	6.10×10^{-6}	6.97×10^{-6}	5.23×10^{-6}	8.47×10^{-6}	5.44×10^{-6}	5.4×10^{-6}
^{40}Ca	9.56×10^{-3}	6.91×10^{-3}	7.39×10^{-3}	6.71×10^{-3}	8.49×10^{-3}	7.38×10^{-3}	6.36×10^{-3}
^{42}Ca	5.98×10^{-5}	3.53×10^{-5}	3.97×10^{-5}	3.7×10^{-5}	4.53×10^{-5}	2.70×10^{-5}	2.76×10^{-5}
^{43}Ca	2.32×10^{-5}	2.29×10^{-5}	2.66×10^{-5}	1.55×10^{-5}	1.30×10^{-5}	1.18×10^{-5}	1.22×10^{-5}
^{44}Ca	1.0×10^{-3}	1.4×10^{-3}	1.15×10^{-3}	6.58×10^{-4}	5.14×10^{-4}	3.69×10^{-4}	5.11×10^{-4}
^{46}Ca	1.75×10^{-10}	1.59×10^{-10}	1.75×10^{-10}	1.15×10^{-10}	1.78×10^{-10}	2.52×10^{-11}	3.70×10^{-11}
^{48}Ca	1.46×10^{-15}	7.77×10^{-16}	9.33×10^{-16}	5.85×10^{-16}	9.31×10^{-12}	1.11×10^{-16}	2.31×10^{-16}
^{45}Sc	1.57×10^{-6}	1.33×10^{-6}	1.45×10^{-6}	1.2×10^{-6}	1.67×10^{-6}	1.59×10^{-6}	5.84×10^{-7}
^{46}Ti	3.44×10^{-5}	1.68×10^{-5}	1.95×10^{-5}	1.62×10^{-5}	2.94×10^{-5}	1.87×10^{-5}	1.43×10^{-5}
^{47}Ti	1.71×10^{-4}	1.77×10^{-4}	1.79×10^{-4}	1.19×10^{-4}	8.61×10^{-5}	5.44×10^{-5}	7.61×10^{-5}
^{48}Ti	9.25×10^{-3}	9.96×10^{-3}	8.99×10^{-3}	7.46×10^{-3}	4.87×10^{-3}	5.11×10^{-3}	3.34×10^{-3}
^{49}Ti	6.71×10^{-5}	6.60×10^{-5}	6.67×10^{-5}	5.42×10^{-5}	5.24×10^{-5}	6.48×10^{-5}	2.46×10^{-5}
^{50}Ti	1.16×10^{-9}	1.53×10^{-9}	1.55×10^{-9}	1.46×10^{-9}	1.22×10^{-5}	4.28×10^{-10}	4.71×10^{-10}
^{50}V	6.12×10^{-9}	7.11×10^{-9}	6.77×10^{-9}	6.7×10^{-9}	8.42×10^{-7}	1.62×10^{-8}	2.39×10^{-9}
^{51}V	1.5×10^{-3}	1.1×10^{-3}	9.89×10^{-4}	7.96×10^{-4}	5.89×10^{-4}	3.84×10^{-4}	3.74×10^{-4}

Table 17. *cont′d* of Table 16.

M	0.90	0.95	1.00	1.05	1.10	1.15	1.20
$M_{\rm He}$	0.15	0.15	0.10	0.10	0.10	0.10	0.05
^{50}Cr	2.8×10^{-4}	1.29×10^{-4}	1.35×10^{-4}	1.25×10^{-4}	2.18×10^{-4}	1.83×10^{-4}	1.20×10^{-4}
^{52}Cr	1.36×10^{-2}	1.74×10^{-2}	1.6×10^{-2}	1.67×10^{-2}	1.60×10^{-2}	1.24×10^{-2}	8.18×10^{-3}
^{53}Cr	4.36×10^{-4}	3.84×10^{-4}	3.40×10^{-4}	3.76×10^{-4}	4.87×10^{-4}	4.52×10^{-4}	2.42×10^{-4}
^{54}Cr	5.24×10^{-8}	9.91×10^{-8}	4.6×10^{-8}	2.79×10^{-8}	1.37×10^{-4}	5.88×10^{-7}	3.12×10^{-8}
^{55}Mn	1.96×10^{-3}	1.78×10^{-3}	1.59×10^{-3}	2.11×10^{-3}	2.28×10^{-3}	2.16×10^{-3}	2.85×10^{-3}
^{54}Fe	6.59×10^{-3}	4.18×10^{-3}	4.55×10^{-3}	4.65×10^{-3}	7.80×10^{-3}	6.52×10^{-3}	1.17×10^{-2}
^{56}Fe	1.39×10^{-1}	3.17×10^{-1}	3.52×10^{-1}	4.93×10^{-1}	6.10×10^{-1}	7.97×10^{-1}	8.26×10^{-1}
^{57}Fe	6.32×10^{-3}	1.11×10^{-2}	1.13×10^{-2}	1.64×10^{-2}	2.12×10^{-2}	2.65×10^{-2}	2.72×10^{-2}
^{58}Fe	1.71×10^{-8}	6.75×10^{-8}	1.9×10^{-8}	7.29×10^{-9}	4.39×10^{-4}	5.86×10^{-7}	9.43×10^{-9}
^{60}Fe	1.45×10^{-18}	9.5×10^{-19}	6.46×10^{-19}	4.59×10^{-19}	1.34×10^{-9}	2.17×10^{-17}	3.13×10^{-19}
^{59}Co	2.47×10^{-4}	3.44×10^{-4}	3.94×10^{-4}	5.34×10^{-4}	7.19×10^{-4}	8.1×10^{-4}	6.90×10^{-4}
^{58}Ni	5.8×10^{-3}	1.27×10^{-2}	1.49×10^{-2}	2.21×10^{-2}	3.26×10^{-2}	3.87×10^{-2}	5.43×10^{-2}
^{60}Ni	3.63×10^{-3}	6.2×10^{-3}	5.57×10^{-3}	8.12×10^{-3}	8.28×10^{-3}	9.20×10^{-3}	6.92×10^{-3}
^{61}Ni	4.35×10^{-4}	4.71×10^{-4}	3.71×10^{-4}	6.39×10^{-4}	5.99×10^{-4}	5.77×10^{-4}	4.46×10^{-4}
^{62}Ni	6.55×10^{-4}	1.46×10^{-3}	1.42×10^{-3}	2.6×10^{-3}	2.20×10^{-3}	2.40×10^{-3}	1.96×10^{-3}
^{64}Ni	9.49×10^{-11}	2.80×10^{-12}	4.49×10^{-11}	1.50×10^{-12}	6.96×10^{-7}	1.22×10^{-10}	3.1×10^{-11}
^{63}Cu	7.58×10^{-6}	6.93×10^{-6}	6.10×10^{-6}	6.60×10^{-6}	5.59×10^{-6}	3.84×10^{-6}	3.75×10^{-6}
^{65}Cu	2.21×10^{-5}	2.6×10^{-5}	1.68×10^{-5}	2.59×10^{-5}	1.76×10^{-5}	1.27×10^{-5}	1.39×10^{-5}
^{64}Zn	1.6×10^{-4}	1.3×10^{-4}	7.2×10^{-5}	1.46×10^{-4}	1.16×10^{-4}	8.74×10^{-5}	7.18×10^{-5}
^{66}Zn	4.63×10^{-5}	6.76×10^{-5}	5.21×10^{-5}	7.15×10^{-5}	5.2×10^{-5}	4.32×10^{-5}	4.23×10^{-5}
^{67}Zn	7.95×10^{-6}	7.76×10^{-6}	6.11×10^{-6}	6.29×10^{-6}	4.36×10^{-6}	2.63×10^{-6}	3.7×10^{-6}
^{68}Zn	4.15×10^{-6}	4.56×10^{-6}	3.34×10^{-6}	1.5×10^{-5}	7.56×10^{-6}	3.93×10^{-6}	3.27×10^{-6}
^{70}Zn	4.40×10^{-15}	6.16×10^{-17}	3.36×10^{-11}	5.53×10^{-17}	1.10×10^{-13}	2.26×10^{-14}	2.28×10^{-16}

Table 18. Similar to Table 16 but for the radioactive isotopes of the selected models after explosion. Masses are in units of solar mass.

M	0.90	0.95	1.00	1.05	1.10	1.15	1.20
$M_{\rm He}$	0.15	0.15	0.10	0.10	0.10	0.10	0.05
^{22}Na	8.72×10^{-8}	2.71×10^{-8}	3.50×10^{-8}	3.2×10^{-8}	1.25×10^{-8}	2.0×10^{-9}	9.56×10^{-9}
^{26}Al	4.50×10^{-5}	1.46×10^{-5}	1.72×10^{-5}	1.49×10^{-5}	6.98×10^{-6}	1.50×10^{-6}	4.78×10^{-6}
^{39}Ar	2.90×10^{-8}	1.20×10^{-8}	1.35×10^{-8}	9.97×10^{-9}	1.99×10^{-8}	2.96×10^{-9}	4.99×10^{-9}
^{40}K	1.73×10^{-7}	6.72×10^{-8}	9.15×10^{-8}	5.46×10^{-8}	1.23×10^{-7}	2.31×10^{-8}	2.94×10^{-8}
^{41}Ca	9.96×10^{-6}	6.19×10^{-6}	7.5×10^{-6}	5.27×10^{-6}	8.49×10^{-6}	5.46×10^{-6}	5.8×10^{-6}
^{44}Ti	1.0×10^{-3}	1.4×10^{-3}	1.14×10^{-3}	6.58×10^{-4}	5.14×10^{-4}	3.69×10^{-4}	5.11×10^{-4}
^{48}V	2.50×10^{-6}	2.21×10^{-6}	2.59×10^{-6}	1.16×10^{-6}	3.26×10^{-6}	1.7×10^{-6}	7.73×10^{-7}
^{49}V	2.43×10^{-7}	2.7×10^{-7}	2.6×10^{-7}	1.58×10^{-7}	5.19×10^{-6}	5.53×10^{-7}	1.7×10^{-7}
^{53}Mn	1.28×10^{-5}	1.30×10^{-5}	9.54×10^{-6}	5.48×10^{-6}	1.6×10^{-4}	3.34×10^{-5}	7.11×10^{-6}
^{60}Fe	2.4×10^{-17}	1.32×10^{-17}	9.26×10^{-18}	6.74×10^{-18}	2.1×10^{-8}	3.25×10^{-16}	4.49×10^{-18}
^{56}Co	1.10×10^{-5}	1.4×10^{-5}	5.8×10^{-6}	4.41×10^{-6}	8.95×10^{-5}	9.86×10^{-5}	1.45×10^{-5}
^{57}Co	8.35×10^{-6}	1.4×10^{-5}	4.83×10^{-6}	2.85×10^{-6}	1.47×10^{-4}	4.7×10^{-5}	6.10×10^{-6}
^{60}Co	1.19×10^{-13}	1.71×10^{-12}	9.14×10^{-14}	8.67×10^{-14}	8.90×10^{-8}	4.87×10^{-11}	7.92×10^{-14}
^{56}Ni	1.38×10^{-1}	3.17×10^{-1}	3.52×10^{-1}	4.93×10^{-1}	6.8×10^{-1}	7.96×10^{-1}	8.26×10^{-1}
^{57}Ni	6.31×10^{-3}	1.11×10^{-2}	1.13×10^{-2}	1.64×10^{-2}	2.10×10^{-2}	2.64×10^{-2}	2.72×10^{-2}
^{59}Ni	6.5×10^{-6}	3.50×10^{-6}	1.70×10^{-6}	1.37×10^{-6}	7.33×10^{-5}	1.88×10^{-5}	1.21×10^{-5}
^{63}Ni	1.51×10^{-12}	1.19×10^{-13}	1.29×10^{-13}	4.23×10^{-14}	9.31×10^{-8}	1.25×10^{-12}	4.94×10^{-13}

Table 19. The nucleosynthesis yields for stable isotopes from the selected models using a He detonation ring as the initial configuration. based on the benchmark model 110-050-2-B50. $M_{\rm He} = 0.05\ M_\odot$ for all models in this table. Masses are in units of solar mass.

$M(M_\odot)$	0.90	0.95	1.00	1.05	1.10	1.20
^{12}C	6.40×10^{-2}	6.0×10^{-2}	1.15×10^{-3}	6.86×10^{-3}	4.2×10^{-3}	7.84×10^{-6}
^{13}C	2.2×10^{-8}	1.60×10^{-8}	3.2×10^{-9}	7.8×10^{-9}	8.97×10^{-9}	1.6×10^{-11}
^{14}N	5.8×10^{-7}	4.40×10^{-7}	1.63×10^{-8}	1.14×10^{-7}	7.62×10^{-8}	6.96×10^{-12}
^{15}N	1.2×10^{-8}	1.14×10^{-8}	2.13×10^{-10}	1.71×10^{-9}	1.38×10^{-9}	9.11×10^{-12}
^{16}O	4.28×10^{-1}	3.86×10^{-1}	6.64×10^{-2}	1.35×10^{-1}	1.2×10^{-1}	6.89×10^{-3}
^{17}O	2.96×10^{-7}	2.56×10^{-7}	1.8×10^{-8}	6.97×10^{-8}	4.32×10^{-8}	1.23×10^{-13}
^{18}O	3.82×10^{-9}	3.52×10^{-9}	9.43×10^{-11}	6.91×10^{-10}	5.10×10^{-10}	4.95×10^{-16}
^{19}F	3.79×10^{-10}	3.64×10^{-10}	2.39×10^{-11}	8.36×10^{-11}	6.80×10^{-11}	5.48×10^{-16}
^{20}Ne	3.77×10^{-2}	2.98×10^{-2}	1.15×10^{-3}	7.69×10^{-3}	4.72×10^{-3}	1.50×10^{-6}
^{21}Ne	2.36×10^{-6}	2.15×10^{-6}	1.57×10^{-7}	5.52×10^{-7}	4.33×10^{-7}	8.30×10^{-11}
^{22}Ne	2.14×10^{-3}	1.98×10^{-3}	8.99×10^{-9}	1.88×10^{-4}	9.46×10^{-5}	6.27×10^{-11}
^{23}Na	1.51×10^{-4}	1.31×10^{-4}	8.39×10^{-6}	2.97×10^{-5}	2.10×10^{-5}	8.5×10^{-8}
^{24}Mg	5.56×10^{-2}	4.28×10^{-2}	1.28×10^{-3}	1.15×10^{-2}	8.62×10^{-3}	3.2×10^{-5}
^{25}Mg	4.1×10^{-4}	3.13×10^{-4}	1.45×10^{-5}	7.25×10^{-5}	4.99×10^{-5}	2.42×10^{-8}
^{26}Mg	4.88×10^{-4}	4.22×10^{-4}	2.72×10^{-5}	9.78×10^{-5}	6.65×10^{-5}	9.82×10^{-8}
^{26}Al	7.39×10^{-5}	5.12×10^{-5}	1.70×10^{-6}	1.29×10^{-5}	8.12×10^{-6}	4.23×10^{-9}
^{27}Al	5.4×10^{-3}	3.75×10^{-3}	1.14×10^{-4}	9.34×10^{-4}	7.17×10^{-4}	2.68×10^{-6}
^{28}Si	1.47×10^{-1}	1.70×10^{-1}	1.25×10^{-1}	1.95×10^{-1}	1.10×10^{-1}	2.58×10^{-2}
^{29}Si	4.31×10^{-3}	3.75×10^{-3}	2.67×10^{-4}	1.11×10^{-3}	8.24×10^{-4}	1.33×10^{-5}
^{30}Si	7.86×10^{-3}	6.77×10^{-3}	3.79×10^{-4}	1.99×10^{-3}	1.58×10^{-3}	1.70×10^{-5}
^{31}P	1.65×10^{-3}	1.36×10^{-3}	1.53×10^{-4}	4.58×10^{-4}	3.54×10^{-4}	1.38×10^{-5}
^{32}S	4.27×10^{-2}	5.68×10^{-2}	6.56×10^{-2}	8.62×10^{-2}	4.90×10^{-2}	1.54×10^{-2}
^{33}S	9.91×10^{-4}	9.46×10^{-4}	1.89×10^{-4}	3.97×10^{-4}	3.8×10^{-4}	2.10×10^{-5}
^{34}S	2.98×10^{-3}	3.66×10^{-3}	1.91×10^{-3}	2.73×10^{-3}	1.97×10^{-3}	1.83×10^{-4}
^{36}S	7.68×10^{-7}	7.22×10^{-7}	5.59×10^{-8}	1.97×10^{-7}	1.63×10^{-7}	1.24×10^{-9}
^{35}Cl	4.81×10^{-4}	3.20×10^{-4}	1.4×10^{-4}	1.65×10^{-4}	1.30×10^{-4}	1.33×10^{-5}
^{37}Cl	2.54×10^{-5}	3.13×10^{-5}	2.51×10^{-5}	3.14×10^{-5}	2.37×10^{-5}	3.72×10^{-6}
^{36}Ar	4.1×10^{-3}	6.94×10^{-3}	1.15×10^{-2}	1.32×10^{-2}	7.52×10^{-3}	3.19×10^{-3}
^{38}Ar	6.34×10^{-4}	9.8×10^{-4}	1.34×10^{-3}	1.39×10^{-3}	1.4×10^{-3}	1.43×10^{-4}
^{40}Ar	1.51×10^{-8}	1.21×10^{-8}	1.69×10^{-9}	3.35×10^{-9}	3.1×10^{-9}	6.50×10^{-11}
^{39}K	6.37×10^{-5}	6.25×10^{-5}	9.25×10^{-5}	1.3×10^{-4}	8.52×10^{-5}	1.65×10^{-5}
^{40}K	2.77×10^{-7}	1.69×10^{-7}	3.86×10^{-8}	5.74×10^{-8}	5.44×10^{-8}	3.13×10^{-9}
^{41}K	1.43×10^{-8}	1.31×10^{-8}	3.14×10^{-9}	5.6×10^{-9}	4.25×10^{-9}	3.56×10^{-10}
^{40}Ca	2.55×10^{-3}	4.83×10^{-3}	1.4×10^{-2}	1.2×10^{-2}	6.87×10^{-3}	4.7×10^{-3}
^{42}Ca	1.78×10^{-5}	2.49×10^{-5}	4.24×10^{-5}	4.9×10^{-5}	3.39×10^{-5}	6.97×10^{-6}
^{43}Ca	6.12×10^{-6}	1.55×10^{-6}	1.38×10^{-5}	3.98×10^{-6}	1.39×10^{-5}	1.22×10^{-5}
^{44}Ca	2.56×10^{-5}	5.0×10^{-6}	2.89×10^{-5}	1.13×10^{-5}	6.55×10^{-5}	6.17×10^{-5}
^{46}Ca	2.58×10^{-10}	2.53×10^{-10}	4.90×10^{-11}	7.11×10^{-11}	6.92×10^{-11}	2.26×10^{-12}
^{48}Ca	1.72×10^{-15}	1.43×10^{-15}	9.28×10^{-16}	5.10×10^{-16}	5.8×10^{-16}	4.93×10^{-18}
^{45}Sc	3.45×10^{-7}	3.35×10^{-7}	3.77×10^{-7}	3.70×10^{-7}	7.81×10^{-7}	5.19×10^{-7}
^{46}Ti	6.57×10^{-6}	1.1×10^{-5}	1.85×10^{-5}	1.91×10^{-5}	1.53×10^{-5}	5.39×10^{-6}
^{47}Ti	2.24×10^{-5}	5.19×10^{-6}	2.27×10^{-5}	7.83×10^{-6}	6.58×10^{-5}	6.59×10^{-5}
^{48}Ti	9.64×10^{-4}	2.84×10^{-4}	7.8×10^{-4}	3.60×10^{-4}	2.61×10^{-3}	3.70×10^{-3}
^{49}Ti	8.56×10^{-6}	8.99×10^{-6}	1.47×10^{-5}	1.26×10^{-5}	2.83×10^{-5}	2.94×10^{-5}
^{50}Ti	1.8×10^{-9}	1.66×10^{-9}	6.7×10^{-10}	7.99×10^{-10}	7.12×10^{-10}	7.54×10^{-11}
^{50}V	5.37×10^{-9}	8.68×10^{-9}	3.68×10^{-9}	4.9×10^{-9}	3.86×10^{-9}	5.91×10^{-10}
^{51}V	8.33×10^{-5}	5.3×10^{-5}	7.62×10^{-5}	5.93×10^{-5}	2.81×10^{-4}	3.20×10^{-4}

Table 20. *cont′d* of Table 19.

$M(M_\odot)$	0.90	0.95	1.00	1.05	1.10	1.20
^{50}Cr	4.32×10^{-5}	8.96×10^{-5}	2.29×10^{-4}	2.1×10^{-4}	1.9×10^{-4}	7.79×10^{-5}
^{52}Cr	1.27×10^{-3}	1.72×10^{-3}	2.87×10^{-3}	2.96×10^{-3}	2.80×10^{-3}	9.80×10^{-3}
^{53}Cr	4.95×10^{-5}	1.28×10^{-4}	2.2×10^{-4}	2.1×10^{-4}	1.56×10^{-4}	2.71×10^{-4}
^{54}Cr	1.79×10^{-8}	8.10×10^{-8}	8.83×10^{-8}	5.64×10^{-8}	6.70×10^{-8}	1.59×10^{-8}
^{55}Mn	3.18×10^{-4}	7.12×10^{-4}	1.8×10^{-3}	1.16×10^{-3}	9.15×10^{-4}	1.99×10^{-3}
^{54}Fe	1.71×10^{-3}	4.12×10^{-3}	1.11×10^{-2}	1.7×10^{-2}	5.20×10^{-3}	5.59×10^{-3}
^{56}Fe	3.58×10^{-2}	1.7×10^{-1}	3.12×10^{-1}	4.68×10^{-1}	6.84×10^{-1}	9.21×10^{-1}
^{57}Fe	1.5×10^{-3}	3.5×10^{-3}	8.17×10^{-3}	1.24×10^{-2}	1.90×10^{-2}	2.71×10^{-2}
^{58}Fe	4.54×10^{-9}	5.66×10^{-8}	2.43×10^{-8}	1.56×10^{-8}	4.83×10^{-8}	4.68×10^{-9}
^{60}Fe	7.82×10^{-19}	1.26×10^{-18}	2.67×10^{-18}	9.49×10^{-19}	1.11×10^{-18}	4.29×10^{-19}
^{59}Co	3.75×10^{-5}	9.83×10^{-5}	3.17×10^{-4}	4.28×10^{-4}	6.17×10^{-4}	6.63×10^{-4}
^{58}Ni	1.17×10^{-3}	3.62×10^{-3}	1.26×10^{-2}	1.95×10^{-2}	3.6×10^{-2}	4.53×10^{-2}
^{60}Ni	6.86×10^{-4}	1.60×10^{-3}	3.87×10^{-3}	5.7×10^{-3}	6.41×10^{-3}	6.13×10^{-3}
^{61}Ni	6.4×10^{-5}	9.30×10^{-5}	1.55×10^{-4}	1.97×10^{-4}	2.48×10^{-4}	3.21×10^{-4}
^{62}Ni	1.61×10^{-4}	3.91×10^{-4}	1.8×10^{-3}	1.43×10^{-3}	1.83×10^{-3}	1.69×10^{-3}
^{64}Ni	3.0×10^{-14}	7.77×10^{-10}	1.49×10^{-12}	3.69×10^{-13}	8.3×10^{-13}	1.13×10^{-13}
^{63}Cu	4.77×10^{-7}	5.25×10^{-7}	1.19×10^{-6}	1.35×10^{-6}	2.24×10^{-6}	2.83×10^{-6}
^{65}Cu	3.10×10^{-6}	1.82×10^{-6}	2.11×10^{-6}	2.17×10^{-6}	3.49×10^{-6}	6.87×10^{-6}
^{64}Zn	1.16×10^{-5}	1.19×10^{-5}	1.71×10^{-5}	1.32×10^{-5}	1.30×10^{-5}	4.32×10^{-5}
^{66}Zn	7.85×10^{-6}	9.57×10^{-6}	1.49×10^{-5}	1.73×10^{-5}	2.15×10^{-5}	2.83×10^{-5}
^{67}Zn	3.36×10^{-7}	3.35×10^{-7}	3.16×10^{-7}	3.61×10^{-7}	1.21×10^{-6}	2.25×10^{-6}
^{68}Zn	4.42×10^{-7}	4.83×10^{-7}	4.55×10^{-7}	2.69×10^{-7}	4.7×10^{-7}	2.25×10^{-6}
^{70}Zn	4.23×10^{-15}	4.3×10^{-14}	1.96×10^{-17}	1.29×10^{-15}	5.22×10^{-17}	9.12×10^{-19}

Table 21. Similar to Table 19, but for the radioactive isotopes. Masses are in units of solar mass.

$M(M_\odot)$	0.90	0.95	1.00	1.05	1.10	1.20
^{22}Na	1.12×10^{-7}	9.86×10^{-8}	3.74×10^{-9}	2.49×10^{-8}	1.56×10^{-8}	4.95×10^{-11}
^{26}Al	7.39×10^{-5}	5.12×10^{-5}	1.70×10^{-6}	1.29×10^{-5}	8.12×10^{-6}	4.10×10^{-9}
^{39}Ar	3.52×10^{-8}	2.39×10^{-8}	7.27×10^{-9}	9.79×10^{-9}	8.69×10^{-9}	5.15×10^{-10}
^{40}K	2.77×10^{-7}	1.69×10^{-7}	3.86×10^{-8}	5.74×10^{-8}	5.44×10^{-8}	3.13×10^{-9}
^{41}Ca	2.77×10^{-6}	4.13×10^{-6}	5.66×10^{-6}	6.52×10^{-6}	5.71×10^{-6}	1.22×10^{-6}
^{44}Ti	2.33×10^{-4}	4.37×10^{-5}	2.64×10^{-4}	1.2×10^{-4}	5.99×10^{-4}	5.65×10^{-4}
^{48}V	2.67×10^{-7}	1.43×10^{-7}	1.96×10^{-7}	1.59×10^{-7}	1.15×10^{-6}	6.95×10^{-7}
^{49}V	9.7×10^{-8}	1.73×10^{-7}	1.54×10^{-7}	1.52×10^{-7}	1.85×10^{-7}	4.78×10^{-8}
^{53}Mn	3.45×10^{-6}	9.83×10^{-6}	9.5×10^{-6}	1.40×10^{-5}	1.15×10^{-5}	1.85×10^{-6}
^{60}Fe	1.16×10^{-17}	1.81×10^{-17}	4.59×10^{-17}	1.36×10^{-17}	1.62×10^{-17}	5.72×10^{-18}
^{56}Co	9.18×10^{-7}	1.37×10^{-5}	8.93×10^{-6}	4.75×10^{-6}	1.79×10^{-5}	9.50×10^{-6}
^{57}Co	1.57×10^{-6}	7.14×10^{-6}	5.62×10^{-6}	7.38×10^{-6}	9.87×10^{-6}	1.41×10^{-6}
^{60}Co	3.98×10^{-14}	1.83×10^{-12}	1.17×10^{-13}	1.4×10^{-13}	6.59×10^{-13}	3.60×10^{-14}
^{56}Ni	3.58×10^{-2}	1.7×10^{-1}	6.0×10^{-1}	4.68×10^{-1}	6.84×10^{-1}	9.95×10^{-1}
^{57}Ni	1.5×10^{-3}	3.4×10^{-3}	1.60×10^{-2}	1.24×10^{-2}	1.90×10^{-2}	2.82×10^{-2}
^{59}Ni	3.98×10^{-7}	2.88×10^{-6}	2.89×10^{-6}	1.92×10^{-6}	4.77×10^{-6}	4.30×10^{-6}
^{63}Ni	5.77×10^{-16}	7.35×10^{-12}	2.12×10^{-15}	9.42×10^{-15}	2.62×10^{-14}	2.97×10^{-15}

Table 22. The nucleosynthesis yields for stable isotopes from the selected models using a spherical He detonation as the initial configuration. based on the benchmark model 110-050-2-S50. $M_{\rm He} = 0.05\ M_\odot$ for all models in this table. Masses are in units of solar mass.

$M(M_\odot)$	0.90	0.95	1.00	1.05	1.10	1.20
^{12}C	5.27×10^{-3}	4.1×10^{-3}	1.15×10^{-3}	2.97×10^{-4}	7.65×10^{-4}	7.84×10^{-6}
^{13}C	1.15×10^{-7}	3.32×10^{-7}	3.2×10^{-9}	4.6×10^{-11}	3.70×10^{-10}	1.6×10^{-11}
^{14}N	4.51×10^{-7}	4.93×10^{-7}	1.63×10^{-8}	2.22×10^{-10}	1.54×10^{-9}	6.96×10^{-12}
^{15}N	3.24×10^{-9}	2.61×10^{-9}	2.13×10^{-10}	6.54×10^{-11}	1.27×10^{-10}	9.11×10^{-12}
^{16}O	2.67×10^{-1}	1.14×10^{-1}	6.64×10^{-2}	3.90×10^{-2}	2.30×10^{-2}	6.89×10^{-3}
^{17}O	1.88×10^{-7}	1.62×10^{-7}	1.8×10^{-8}	8.12×10^{-11}	8.10×10^{-10}	1.23×10^{-13}
^{18}O	3.51×10^{-9}	3.29×10^{-9}	9.43×10^{-11}	1.99×10^{-12}	1.46×10^{-11}	4.95×10^{-16}
^{19}F	2.71×10^{-10}	2.20×10^{-10}	2.39×10^{-11}	9.14×10^{-13}	6.1×10^{-12}	5.48×10^{-16}
^{20}Ne	6.53×10^{-3}	1.46×10^{-3}	1.15×10^{-3}	4.63×10^{-4}	7.54×10^{-4}	1.50×10^{-6}
^{21}Ne	1.62×10^{-6}	1.34×10^{-6}	1.57×10^{-7}	1.40×10^{-8}	5.1×10^{-8}	8.30×10^{-11}
^{22}Ne	7.66×10^{-5}	8.61×10^{-5}	8.99×10^{-9}	1.53×10^{-9}	3.64×10^{-9}	6.27×10^{-11}
^{23}Na	4.32×10^{-5}	2.30×10^{-5}	8.39×10^{-6}	3.35×10^{-6}	4.66×10^{-6}	8.5×10^{-8}
^{24}Mg	2.29×10^{-2}	2.53×10^{-3}	1.28×10^{-3}	5.46×10^{-4}	4.43×10^{-4}	3.2×10^{-5}
^{25}Mg	1.0×10^{-4}	3.6×10^{-5}	1.45×10^{-5}	3.84×10^{-6}	7.30×10^{-6}	2.42×10^{-8}
^{26}Mg	1.26×10^{-4}	4.20×10^{-5}	2.72×10^{-5}	7.3×10^{-6}	1.21×10^{-5}	9.82×10^{-8}
^{26}Al	1.39×10^{-5}	2.16×10^{-6}	1.70×10^{-6}	8.41×10^{-7}	1.3×10^{-6}	4.23×10^{-9}
^{27}Al	1.98×10^{-3}	2.16×10^{-4}	1.14×10^{-4}	5.41×10^{-5}	4.32×10^{-5}	2.68×10^{-6}
^{28}Si	3.32×10^{-1}	1.60×10^{-1}	1.25×10^{-1}	1.3×10^{-1}	7.51×10^{-2}	2.58×10^{-2}
^{29}Si	2.3×10^{-3}	4.80×10^{-4}	2.67×10^{-4}	1.31×10^{-4}	1.10×10^{-4}	1.33×10^{-5}
^{30}Si	4.47×10^{-3}	8.4×10^{-4}	3.79×10^{-4}	1.76×10^{-4}	1.13×10^{-4}	1.70×10^{-5}
^{31}P	9.78×10^{-4}	2.75×10^{-4}	1.53×10^{-4}	9.56×10^{-5}	5.26×10^{-5}	1.38×10^{-5}
^{32}S	1.41×10^{-1}	8.0×10^{-2}	6.56×10^{-2}	5.45×10^{-2}	4.7×10^{-2}	1.54×10^{-2}
^{33}S	8.94×10^{-4}	3.18×10^{-4}	1.89×10^{-4}	1.27×10^{-4}	6.98×10^{-5}	2.10×10^{-5}
^{34}S	5.22×10^{-3}	3.17×10^{-3}	1.91×10^{-3}	1.12×10^{-3}	5.83×10^{-4}	1.83×10^{-4}
^{36}S	4.80×10^{-7}	1.2×10^{-7}	5.59×10^{-8}	2.86×10^{-8}	3.59×10^{-8}	1.24×10^{-9}
^{35}Cl	3.58×10^{-4}	1.43×10^{-4}	1.4×10^{-4}	8.11×10^{-5}	4.65×10^{-5}	1.33×10^{-5}
^{37}Cl	7.9×10^{-5}	3.32×10^{-5}	2.51×10^{-5}	2.1×10^{-5}	1.17×10^{-5}	3.72×10^{-6}
^{36}Ar	1.88×10^{-2}	1.34×10^{-2}	1.15×10^{-2}	9.40×10^{-3}	7.42×10^{-3}	3.19×10^{-3}
^{38}Ar	3.40×10^{-3}	1.88×10^{-3}	1.34×10^{-3}	9.84×10^{-4}	5.11×10^{-4}	1.43×10^{-4}
^{40}Ar	9.41×10^{-9}	2.57×10^{-9}	1.69×10^{-9}	1.25×10^{-9}	8.67×10^{-10}	6.50×10^{-11}
^{39}K	2.56×10^{-4}	1.13×10^{-4}	9.25×10^{-5}	7.56×10^{-5}	4.69×10^{-5}	1.65×10^{-5}
^{40}K	1.59×10^{-7}	5.28×10^{-8}	3.86×10^{-8}	3.31×10^{-8}	1.73×10^{-8}	3.13×10^{-9}
^{41}K	1.23×10^{-8}	4.90×10^{-9}	3.14×10^{-9}	2.38×10^{-9}	1.45×10^{-9}	3.56×10^{-10}
^{40}Ca	1.17×10^{-2}	1.12×10^{-2}	1.4×10^{-2}	7.54×10^{-3}	6.70×10^{-3}	4.7×10^{-3}
^{42}Ca	1.3×10^{-4}	5.63×10^{-5}	4.24×10^{-5}	3.24×10^{-5}	1.85×10^{-5}	6.97×10^{-6}
^{43}Ca	1.22×10^{-6}	4.26×10^{-6}	1.38×10^{-5}	5.89×10^{-6}	7.6×10^{-6}	1.22×10^{-5}
^{44}Ca	3.81×10^{-6}	6.72×10^{-6}	2.89×10^{-5}	6.32×10^{-6}	2.11×10^{-5}	6.17×10^{-5}
^{46}Ca	2.42×10^{-10}	7.92×10^{-11}	4.90×10^{-11}	4.55×10^{-11}	1.93×10^{-11}	2.26×10^{-12}
^{48}Ca	1.85×10^{-15}	9.88×10^{-16}	9.28×10^{-16}	7.92×10^{-16}	7.98×10^{-16}	4.93×10^{-18}
^{45}Sc	6.22×10^{-7}	3.73×10^{-7}	3.77×10^{-7}	2.18×10^{-7}	7.16×10^{-7}	5.19×10^{-7}
^{46}Ti	5.46×10^{-5}	2.20×10^{-5}	1.85×10^{-5}	1.50×10^{-5}	1.41×10^{-5}	5.39×10^{-6}
^{47}Ti	5.34×10^{-6}	4.63×10^{-6}	2.27×10^{-5}	8.32×10^{-6}	2.61×10^{-5}	6.59×10^{-5}
^{48}Ti	1.51×10^{-4}	2.92×10^{-4}	7.8×10^{-4}	2.58×10^{-4}	9.96×10^{-4}	3.70×10^{-3}
^{49}Ti	8.47×10^{-6}	1.58×10^{-5}	1.47×10^{-5}	8.40×10^{-6}	1.33×10^{-5}	2.94×10^{-5}
^{50}Ti	2.16×10^{-9}	1.42×10^{-9}	6.7×10^{-10}	4.45×10^{-10}	1.13×10^{-10}	7.54×10^{-11}
^{50}V	9.96×10^{-9}	7.6×10^{-9}	3.68×10^{-9}	2.87×10^{-9}	1.23×10^{-9}	5.91×10^{-10}
^{51}V	3.31×10^{-5}	5.99×10^{-5}	7.62×10^{-5}	3.46×10^{-5}	7.64×10^{-5}	3.20×10^{-4}

Table 23. *cont'd* of Table 22.

$M(M_\odot)$	0.90	0.95	1.00	1.05	1.10	1.20
^{50}Cr	3.1×10^{-4}	1.63×10^{-4}	1.41×10^{-4}	1.22×10^{-4}	1.13×10^{-4}	2.93×10^{-5}
^{52}Cr	5.29×10^{-4}	2.99×10^{-3}	2.94×10^{-3}	1.73×10^{-3}	2.14×10^{-3}	7.38×10^{-3}
^{53}Cr	8.54×10^{-5}	2.63×10^{-4}	2.14×10^{-4}	1.38×10^{-4}	1.44×10^{-4}	2.6×10^{-4}
^{54}Cr	1.3×10^{-7}	5.22×10^{-8}	4.40×10^{-8}	4.64×10^{-8}	3.17×10^{-8}	1.45×10^{-10}
^{55}Mn	4.60×10^{-4}	1.58×10^{-3}	1.32×10^{-3}	7.88×10^{-4}	8.56×10^{-4}	6.32×10^{-4}
^{54}Fe	1.17×10^{-2}	1.2×10^{-2}	8.69×10^{-3}	7.1×10^{-3}	5.94×10^{-3}	6.38×10^{-4}
^{56}Fe	1.55×10^{-2}	4.52×10^{-1}	6.0×10^{-1}	7.4×10^{-1}	8.17×10^{-1}	10.48×10^{-1}
^{57}Fe	5.52×10^{-4}	1.14×10^{-2}	1.60×10^{-2}	1.91×10^{-2}	2.29×10^{-2}	1.95×10^{-2}
^{58}Fe	2.94×10^{-8}	2.31×10^{-8}	1.36×10^{-8}	1.30×10^{-8}	1.5×10^{-8}	7.23×10^{-11}
^{60}Fe	2.99×10^{-18}	4.95×10^{-18}	3.4×10^{-18}	5.0×10^{-18}	1.5×10^{-16}	2.21×10^{-22}
^{59}Co	1.42×10^{-5}	3.86×10^{-4}	5.27×10^{-4}	6.13×10^{-4}	7.14×10^{-4}	1.74×10^{-4}
^{58}Ni	7.72×10^{-4}	1.79×10^{-2}	2.50×10^{-2}	3.5×10^{-2}	3.60×10^{-2}	7.7×10^{-3}
^{60}Ni	5.19×10^{-4}	4.99×10^{-3}	6.13×10^{-3}	6.87×10^{-3}	8.16×10^{-3}	1.0×10^{-2}
^{61}Ni	4.72×10^{-5}	1.81×10^{-4}	2.78×10^{-4}	2.77×10^{-4}	3.84×10^{-4}	3.61×10^{-4}
^{62}Ni	3.33×10^{-5}	1.41×10^{-3}	1.72×10^{-3}	1.88×10^{-3}	2.5×10^{-3}	2.97×10^{-4}
^{64}Ni	8.46×10^{-12}	5.56×10^{-12}	4.59×10^{-14}	4.90×10^{-13}	1.25×10^{-11}	1.80×10^{-13}
^{63}Cu	4.69×10^{-7}	1.21×10^{-6}	2.50×10^{-6}	2.29×10^{-6}	2.49×10^{-6}	5.65×10^{-6}
^{65}Cu	1.89×10^{-6}	1.76×10^{-6}	7.61×10^{-6}	4.82×10^{-6}	9.8×10^{-6}	1.28×10^{-5}
^{64}Zn	1.57×10^{-5}	9.39×10^{-6}	2.70×10^{-5}	2.48×10^{-5}	7.18×10^{-5}	2.3×10^{-4}
^{66}Zn	2.15×10^{-6}	1.81×10^{-5}	2.41×10^{-5}	2.33×10^{-5}	2.52×10^{-5}	1.65×10^{-5}
^{67}Zn	1.91×10^{-7}	1.89×10^{-7}	3.41×10^{-7}	2.13×10^{-7}	6.33×10^{-7}	2.31×10^{-6}
^{68}Zn	1.0×10^{-6}	2.82×10^{-7}	3.71×10^{-7}	2.25×10^{-7}	2.9×10^{-6}	3.74×10^{-6}
^{70}Zn	2.71×10^{-15}	1.77×10^{-16}	1.97×10^{-18}	2.46×10^{-16}	9.85×10^{-15}	4.73×10^{-18}

Table 24. Similar to Table 22, but for the radioactive isotopes. Masses are in units of solar mass.

$M(M_\odot)$	0.90	0.95	1.00	1.05	1.10	1.20
^{22}Na	1.94×10^{-8}	5.10×10^{-9}	3.74×10^{-9}	1.31×10^{-9}	2.46×10^{-9}	4.95×10^{-11}
^{26}Al	1.39×10^{-5}	2.16×10^{-6}	1.70×10^{-6}	8.41×10^{-7}	1.3×10^{-6}	4.10×10^{-9}
^{39}Ar	2.33×10^{-8}	1.1×10^{-8}	7.27×10^{-9}	5.89×10^{-9}	3.48×10^{-9}	5.15×10^{-10}
^{40}K	1.59×10^{-7}	5.28×10^{-8}	3.86×10^{-8}	3.31×10^{-8}	1.73×10^{-8}	3.13×10^{-9}
^{41}Ca	1.56×10^{-5}	6.89×10^{-6}	5.66×10^{-6}	4.75×10^{-6}	3.43×10^{-6}	1.22×10^{-6}
^{44}Ti	3.27×10^{-5}	6.5×10^{-5}	2.64×10^{-4}	5.75×10^{-5}	1.93×10^{-4}	5.65×10^{-4}
^{48}V	2.8×10^{-7}	1.81×10^{-7}	1.96×10^{-7}	5.81×10^{-8}	3.20×10^{-7}	6.95×10^{-7}
^{49}V	2.76×10^{-7}	2.21×10^{-7}	1.54×10^{-7}	1.24×10^{-7}	1.72×10^{-7}	4.78×10^{-8}
^{53}Mn	2.76×10^{-5}	1.14×10^{-5}	9.5×10^{-6}	9.36×10^{-6}	6.47×10^{-6}	1.85×10^{-6}
^{60}Fe	4.31×10^{-17}	7.35×10^{-17}	4.59×10^{-17}	7.34×10^{-17}	1.54×10^{-15}	5.72×10^{-18}
^{56}Co	3.65×10^{-6}	2.15×10^{-5}	8.93×10^{-6}	3.8×10^{-6}	3.80×10^{-6}	9.50×10^{-6}
^{57}Co	1.43×10^{-5}	8.54×10^{-6}	5.62×10^{-6}	4.83×10^{-6}	3.63×10^{-6}	1.41×10^{-6}
^{60}Co	6.7×10^{-13}	2.45×10^{-13}	1.17×10^{-13}	1.43×10^{-13}	2.6×10^{-13}	3.60×10^{-14}
^{56}Ni	1.51×10^{-2}	4.52×10^{-1}	6.0×10^{-1}	7.4×10^{-1}	8.17×10^{-1}	9.95×10^{-1}
^{57}Ni	5.39×10^{-4}	1.14×10^{-2}	1.60×10^{-2}	1.91×10^{-2}	2.29×10^{-2}	2.82×10^{-2}
^{59}Ni	2.84×10^{-6}	3.3×10^{-6}	2.89×10^{-6}	1.46×10^{-6}	1.84×10^{-6}	4.30×10^{-6}
^{63}Ni	5.43×10^{-13}	3.93×10^{-13}	2.12×10^{-15}	1.34×10^{-14}	4.1×10^{-13}	2.97×10^{-15}